TN-AP-72-565
OCTOBER 31, 1972
NTIS HC $7.50

Volume I

RESULTS OF A STUDY OF MACH NUMBER AND REYNOLDS NUMBER EFFECTS ON THE LEE SIDE VORTEX FLOW FIELD CHARACTERISTICS OF AN OGIVE-CYLINDER-FRUSTUM-CYLINDER AT ANGLES OF ATTACK TO 25 DEGREES

by J. E. Foley

NASA Contract NAS8-24391

(NASA-CR-123997-Vol-1) RESULTS OF A STUDY OF MACH NUMBER AND REYNOLDS NUMBER EFFECTS ON THE LEE SIDE VORTEX FLOW FIELD CHARACTERISTICS OF AN (Chrysler Corp.) 110 p HC $7.50 CSCL 20D
N73-15307
Unclas
G3/12 52321

11088

SPACE DIVISION CHRYSLER CORPORATION

TECHNICAL NOTE

TN-AP-72-565

VOLUME I

RESULTS OF A STUDY OF MACH NUMBER AND REYNOLDS NUMBER EFFECTS ON THE LEE SIDE VORTEX FLOW FIELD CHARACTERISTICS OF AN OGIVE-CYLINDER-FRUSTUM-CYLINDER AT ANGLES OF ATTACK TO 25 DEGREES

by

J. E. Foley
Research Specialist
Aerodynamics Group

October 31, 1972

APPROVED:
E. A. Rawls, Program Manager
Aerodynamics Group Supervisor

J. P. Tucker, Manager
Aerothermodynamics Section

R. H. Ross, Chief Engineer
Aerospace Physics Branch

CHRYSLER CORPORATION SPACE DIVISION
New Orleans, La.

ABSTRACT

An experimental program was conducted to survey the lee side vortex flow field about an ogive-cylinder-frustum-cylinder at angles of attack to 25 degrees for two Reynolds numbers at Mach number 0.8, and one Reynolds number at Mach number 1.96. The data were obtained using miniature 5-port conical pressure probes calibrated for angle of attack and roll angle over a Mach number range of 0.6 to 3.0. The results are presented here as local flow field properties and circulation strengths for various body stations. This work was accomplished for the Marshall Space Flight Center under contract number NAS8-24391.

TABLE OF CONTENTS

VOLUME I

LIST OF ILLUSTRATIONS

NOMENCLATURE

a	Speed of sound
C_p	Pressure coefficient
D	Reference diameter, maximum model diameter D = 1 in.
D'	Forebody cylinder diameter, D' = .5 in.
M	Mach number
P	Static pressure
P_t	Total pressure
P_i	Probe orifice pressures, i = 1, 5
$\overline{P}$	Average probe cone static pressure, $(P_2+P_3+P_4+P_5)/4$
Re	Freestream unit Reynolds number
$Re_{D'}$	Freestream Reynolds number based on D'
T_t	Total temperature
V	Velocity
$V_{x,\ r,\ \theta}$	Velocity components in cylindrical coordinate system
V_c	Crossflow velocity
x, r, θ	Model cylindrical coordinates, see figure 5
x, y, z	Model rectangular coordinates, see figure 5
α	Angle of attack
β	Probe pressure variable, P_1/P_t

NOMENCLATURE (continued)

$\Gamma/\pi D V_\infty$	Non-dimensional circulation strength
δ	Probe roll angle in calibration test
ϵ	Probe pressure variable, $\tan^{-1}\ [(P_4-P_2)/(P_3-P_5)]$
ρ	Probe pressure variable, $\sqrt{(P_4-P_2)^2+(P_3-P_5)^2}/P_1$
ϕ	Model roll angle, flow survey test
$\omega D/4V_\infty$	Non-dimensional vorticity

Subscripts

b	Denotes conditions at body surface
∞	Denotes free stream conditions

SUMMARY

An experimental program was conducted in the Marshall Space Flight Center 14-in. Trisonic Wind Tunnel to survey the lee side vortex flow field about an ogive-cylinder-frustum-cylinder at angles of attack to 25° for two Reynolds numbers at Mach number 0.8 and one Reynolds number at Mach number 1.96. The data were obtained using miniature 5-port conical pressure probes calibrated for angle of attack and roll angle at Mach numbers from 0.6 to 3.0. The results are presented as contour plots of local flow properties including local vorticity, crossflow velocity vector plots and the total circulation strength and vortex center location.

INTRODUCTION

The evaluation of the non-linear lift induced by crossflow separation about a body of revolution at moderate angles of attack has been a subject of theoretical and experimental studies for many years and has resulted in a number of approaches to the problem. These approaches may generally be classified as either empiric using estimates of the "non-linear" lift or normal force based on an empirically derived crossflow drag coefficient, or as theoretical using a potential model of the flow field which accounts for the presence of a pair of lee-side vortices generated by the crossflow separation. None of the existing approaches, however, yield adequate predictions of the non-linear lift for the range of potential body shapes and free stream conditions largely due to the lack of sufficient experimental data to systematically evaluate the effects of Mach number, Reynolds number and body geometry from which the deficiencies of the empiric and theoretical approaches could be evaluated.

The Marshall Space Flight Center (MSFC) has undertaken an experimental program to expand the data base for the evaluation of the effects of crossflow separation and the adequacy of the empiric and theoretical approaches to the problem. The program consists of an integrated study in which total forces, local surface pressures and flow field measurements, as well as surface and flow field visualization data, are obtained for a wide range of Mach numbers, Reynolds numbers and several body geometries.

Chrysler Corporation, Space Division has participated in this program in obtaining the surface pressure data, correlating surface pressure data and force data, and in obtaining flow field measurements. The results of the surface pressure test program is reported in Reference 1 and the correlation of surface pressures and force data is reported in Reference 2. This report presents the results of the flow field measurements on the lee-side of an ogive-cylinder-frustum-cylinder at $M_\infty = 0.8$ and 1.96 as obtained in the MSFC 14 in. Trisonic Wind Tunnel. These data show the distribution of local flow field properties, including vorticity, on the lee-side of the body at angle of attack and the total circulation strength of the vortex system at several axial stations along the body. The primary purpose of the test was to determine the effect of abrupt changes in body cross-section on the location and strength of the lee-side vortex systems for two Reynolds numbers at $M_\infty = 0.8$ and for one Reynolds number at $M_\infty = 1.96$. Only one Reynolds number condition was tested at $M_\infty = 1.96$ as the surface pressure and force data showed small effects of Reynolds number at this Mach number.

MODELS, INSTRUMENTATION, FACILITY

The body configuration utilized in this test program consisted of an ogive-cylinder-frustum-cylinder (O/C/F/C) as shown in Figure 1. The configuration was selected in order to evaluate the effect of an abrupt change in cross-section, as represented by the 25° frustum, on the forebody wake-vortex system. The forebody is an ogive-cylinder with a 3 caliber (based on forebody cylinder diameter) ogive nose. This forebody is the same as that tested by previous investigators (e.g. References 3, 4) and provides for a source of comparative data on the vortex position and strength generated by the forebody.

The model is constructed in three sections; the nose section, the frustum plus a portion of the aft cylinder, and the remaining aft cylinder (in which the rake is mounted) and sting. The nose section screws onto any of five frustum sections with differing aft cylinder lengths and this assembly is then slipped into the aft section and secured with set screws. During testing the rake remains at a fixed tunnel axial station and the model survey station is varied by using the different frustum sections as illustrated in Figure 1.

The rake consists of two probes mounted in individual struts attached to the aft body. The probes are miniature 5-port conical type with a 25° cone angle and a blunted nose. This configuration was selected based on probe development tests reported in Reference 5 . The probes were constructed by assembling five lengths of hypodermic tubing within a sleeve, with the inner tube spacing maintained by wire inserts between the tubes. The assembly was then soldered at the head, and machined down to the desired cone angle and the tip radiused. Due to the very small size of the probes, it was difficult to maintain tolerances and a number of probes were manufactured and the best ones selected.

The inner tubes thus formed the five orifices on the probe head, one pitot and four cone static orifices. The orifice tubes, .007" I.D. X 2" length, were connected to 6 ft. lengths of .032" O.D. X .020" I.D. extensions. The probe was then mounted in a .125 in. dia. holder with the bottom of the probe flush with the bottom of the probe holder such that the probe centerline is .030 in. below the probe holder centerline. Details of the probes are illustrated in Figures 1 and 2.

The struts which support the probes fit into slots in the model aft body. One strut is always located on the model top centerline and the other strut at a roll position of 270°(Figure 1) except for the most inboard locations. For the most inboard radial locations, one probe is mounted in a strut on the top centerline while the other probe is mounted in a cavity in the frustum section at a roll position of 180°(Figure 2). The struts can be translated in the radial direction at .125 in. increments. Intermediate probe radial locations can be obtained by inverting the probe in the strut which results in a .06 in. outboard translation due to the eccentric centerline of the probe w.r.t. the probe holder centerline. For calibration, the probes are mounted in a dual probe strut with the probes 3 in. apart.

The model is supported in the flow survey tests by a 16° offset sting which also houses an automatic roll mechanism developed for this test. The roll mechanism can be stepped at 7.5° increments on automatic signals from the tunnel control console. For probe calibration, the 16" offset was used along with fixed-roll offsets of 6° and 31°. With the fixed-roll offsets, roll angle was varied manually by rolling the model sting in the offset chuck.

The probe pressure tubes were connected to 0 to 50 psia. absolute pressure transducers mounted outside the tunnel. The pressures were recorded by a 10 channel digital acquisition system and the output punched on IBM cards. Data is then reduced to absolute pressures using an off-line digital computer.

These tests were conducted in the MSFC 14 in. Trisonic Wind Tunnel. Details of the tunnel operating characteristics may be obtained from Reference 6. Typical model installations for the calibration and flow survey tests are shown in the photographs of figures 3 and 4 respectively.

PROBE CALIBRATION TESTS

The probes were mounted in the calibration strut and aligned in roll using a telescope and sighting on the probe orifices in a front view. Probe pitch and yaw alignment was also checked and adjusted. The resulting alignments are estimated to be within $\pm 1^\circ$ in roll and $\pm .5^\circ$ in pitch and yaw.

The calibration strut was mounted alternately in the 6, 16 and 31° offsets allowing calibration from zero to 39° with a tunnel sector pitch range of $\pm 10^\circ$. With the 16° offset incorporating the automatic roll mechanism, a run consisted of a roll sweep of 180° in 7.5° increments at constant angle of attack. A second roll sweep was made for roll angles from 180° to 360° and the 360° roll sweep repeated for angles of attack from 6° to 26° at $7\frac{1}{2}^\circ$ increments. With the 6° and 31° offset, a run consisted of an angle of attack sweep at constant roll angle. A limited number of runs were made with the 6° offset to check the linearity of the probe characteristics at low angles of attack. With the 31° offset, angle of attack sweeps from 21° to 39° were made at roll angles from zero to 90° at 15° increments, and from 90° to 360° at 30° increments.

Calibration data was obtained for the above α/δ schedule at Mach numbers 0.6, 0.8, 1.0, 1.2, 1.46, 1.96 and 2.99. Limited data was also obtained at Mach numbers 0.7, 0.9 and 1.1. The transonic calibration data for Mach numbers 0.6 through 1.1 was obtained during one tunnel entry (MSFC TWT 515) and the supersonic calibration data was obtained in another tunnel entry (MSFC TWT 536). The results of the probe calibration tests will be published as a supplement to this report.

FLOW SURVEY TESTS

The probes were mounted in the flow survey model and aligned in a manner similar to the probe calibration model. Although the nominal probe roll alignment and probe radial locations could not always be obtained in the various model/strut configurations, the actual probe roll angles and radial locations were measured and recorded for use in the data reduction and analysis computer program.

The model sting was instrumented with strain gages from which sting deflection data were obtained. These sting deflections were used to determine tunnel sector pitch settings which would yield model angles of attack consistent with surface pressure tests of this configuration (Reference 1).

For model configurations with probe 1 mounted at a roll position of 0° and probe 2 at 270°, a run consisted of a roll sweep from zero to 90° in 7.5° increments. For configurations with probe 1 mounted at zero and probe 2 mounted at 180° roll position, a run consisted of a 180° roll sweep. This results in data being acquired in different lee side quadrants for probes 1 and 2 as illustrated in the sketches below.

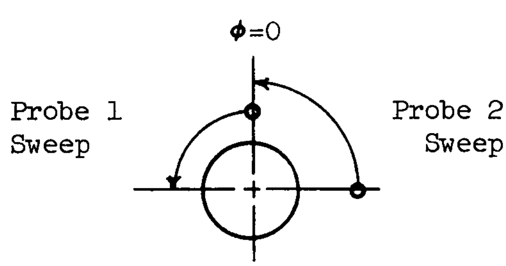

Probe 1 at =0°
Probe 2 at =270°

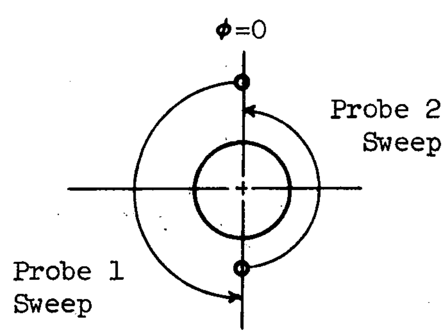

Probe 1 at =0°
Probe 2 at =180°

For the purpose of this test, the lee side flow field must therefore be assumed symmetrical. This assumption is consistent with obtaining flow field data about a body of revolution by the technique of attaching a rake to the body and rolling the body about its centerline. Any lee side flow field asymmetries which might be present are generally attributed to minute model irregularities which will cause the asymmetries to change with model roll angle. Thus the only way to actually survey an asymmetrical flow field would be to use a rake traversing system mounted independent of the body which is feasible only in a limited number of the large wind tunnels. Any flow field asymmetries were expected to be small for the conditions of this test, however, based on results of surface flow visualization tests of this configuration and other flow surveys at similar conditions (References 3 and 4).

Flow survey data were obtained in two tunnel entries, MSFC TWT 516 and 535. In the first entry (TWT 516) flow surveys were obtained at X/D = 3.5, 4.1, 4.4, 4.8 and 6.5 at Mach number 0.8 for the high Reynolds number condition (Re = 7.9×10^6 ft.$^{-1}$) and at angles of attack of 9.9, 14.3, 20.1 and 24.6°. Analysis of this data indicated that the increments in radial survey locations were inadequate at several stations and that the vortex system was too close to the body to define the vortex strength and location at angles of attack of 9.9 and 14.3° for most stations and for all angles of attack at station 4.4.

In the second entry (TWT 535), data was obtained with a greater density of r/D locations for Mach 0.8 at two Reynolds numbers (Re = 4.4 and 7.9×10^6 ft.$^{-1}$) but the survey was restricted to four X/D locations (X/D = 4.4 was dropped) and the two higher angles of attack. In addition, a full survey (five X/D locations and four angles of attack) was obtained at Mach number 1.96 and a Reynolds number of 9.8×10^6 ft.$^{-1}$.

A model roll angle misalignment of 2.5° was inadvertently present in the TWT 535 test set up. This misalignment was accounted for in the data reduction as described in the following section.

DATA REDUCTION

The flow survey data was reduced to local flow field properties using a computer program developed for this purpose. A preliminary version of this program is described in Reference 7. The program has been modified considerably, however, to improve the method of loading probe calibration data, to improve interpolation routines, and other modifications required to handle particular data. A brief description of the program operation is given below. Reference 7 will be revised in the near future to reflect the actual program used in processing the data.

The probe calibration data is read as absolute pressures P_i for each probe orifice from wind tunnel data cards, which also contain the calibration run conditions M, α, δ, Pt, Tt. The five orifice pressures are then reduced to probe calibration variables as given by

$$\rho = \sqrt{(P_4 - P_2)^2 + (P_3 - P_5)^2}/P_1$$

$$\epsilon = \tan^{-1}\left[(P_4 - P_2)/(P_3 - P_5)\right]$$

$$\overline{P}/P_1 = (P_2 + P_3 + P_4 + P_5)/(4\, P_1)$$

$$\beta = P_1/P_t$$

where P_1 is the pitot pressure and $P_{2,\ 3,\ 4,\ 5}$ are cone static pressures as illustrated in Figure 2. The polar form of the local angle of attack variables, ρ and ϵ, were chosen because of their nearly linear dependence with the independent calibration variables α and δ respectively.

Each of the four dependent calibration variables ρ, ϵ, $\overline{P}/P_1$, and β are stored for each probe in tables for selected values of the independent variables α, δ, and M, i.e.

$$\begin{Bmatrix} \rho \\ \epsilon \\ \overline{P}/P_1 \\ \beta \end{Bmatrix} = \begin{Bmatrix} \rho \\ \epsilon \\ \overline{P}/P_1 \\ \beta \end{Bmatrix} \quad (\alpha_i,\ \delta_j, M_k)$$

The independent values of angle of attack (α_i) selected were 0, 6, 11, 16, 21, 24, 28, 32, 36 and 39°. Nominal roll angles (δ_j) varied from 0 to 360° in 15° increments. For angles of attack above 24°, calibration data in the roll angle quadrants from 90 to 360° was obtained in the calibration tests at

30° roll angle increments and the values of the calibration variables for the intermediate roll angles were generated by linear interpolation. All of the primary calibration test Mach numbers were used, i.e. $M_k = 0.6$, .8, 1.0, 1.2, 1.46, 1.96, 2.99. Analysis ofthe data for the intermediate calibration Mach numbers ($M_k = .7$, .9, 1.1) for which only limited calibration data was obtained, indicated the desirability of a complete set of data at $M \cong 0.9$ for improved interpolation accuracy. This data was generated analytically (with emperic modifications) by linear extrapolation of the M = 0.6 and 0.8 data to an intermediate Mach number. The intermediate Mach number was chosen as .87 for probe 1 and as .88 for probe 2, as best fitting the data trends. The complete set of probe calibration tables will be published as a supplement to this report.

The flow survey data is also loaded as orifice pressures for each probe from wind tunnel data cards, and reduced to the probe variables ρ, ϵ, and $\overline{P}/P_1$. For each flow survey data point, the calibration table $\epsilon(M_i, \alpha_j, \delta_k)$ is entered with the measured value of ϵ and used to reduce the ρ and $\overline{P}/P_1$ calibration tables to

$$\begin{Bmatrix} \rho \\ \overline{P}/P_1 \end{Bmatrix} = \begin{Bmatrix} \rho \\ \overline{P}/P_1 \end{Bmatrix} (M_i, \alpha_j)$$

i.e. δ is determined by ϵ for each M_i, α_j and the $\rho(M_i, \alpha_j, \delta_k)$ and $\overline{P}/P_1$ $(M_i, \alpha_j, \delta_k)$ are entered at $\delta = \delta(M_i, \alpha_j)_\epsilon$ to eliminate δ from these tables. Next, the $\overline{P}/P_1$ (M_i, α_j) table is entered at the measured value of $\overline{P}/P_1$ which yields the local Mach number $M = M(\alpha_j)$. Then the $\rho(M_i, \alpha_j)$ table is entered with $M = M(\alpha_j)$ yielding $\rho = \rho(\alpha_j)$, which with the measured ρ defines the local angle of attack α. The local Mach number is then determined from the $M = M(\alpha_j)$ table (α is known) and δ is determined from the $\delta = \delta(M_i, \alpha_j)_\epsilon$ table. With the local flow conditions M, α & δ known P_1/P_t is determined from the P_1/P_t $(M_i, \alpha_j, \delta_k)$ table and the local total pressure is simply

$$P_t = P_1/(P_1/P_t)_{M, \alpha, \delta}$$

All of the table look-ups referred to above use linear interpolations. For the supersonic flow survey ($M_\infty = 1.96$), the calibration Mach number, M_i, was transformed to $1/M_i$ in the $\overline{P}/P_1$ table, i.e.

$$\overline{P}/P_1 = \overline{P}/P_1 \, [1/M_i, \alpha_i, \delta_i]$$

This significantly improves the linearity of $\overline{P}/P_1$ (M_i) at supersonic speeds and improves the accuracy of the interpolations.

The local crossflow flow direction δ, determined above, is the flow angle measured with respect to a probe reference established in the calibration test. As mentioned earlier, it was very difficult to obtain a consistent probe roll alignment in the flow survey struts for the various strut configurations and the probe was therefore set in the approximate roll position and measured by sighting on the orifices with a telescope. Also, some runs were made with the probes inverted in order to obtain intermediate radial positions. These alignment corrections were made to the flow direction angle δ to obtain the actual local crossflow direction θ_{VC},

$$\theta_{VC} = \delta - \Delta\delta$$

where $\Delta\delta$ is the difference in the probe roll alignments between the calibration and flow survey tests.

Knowing the local Mach number M and tunnel total temperature T_{t_∞}, the local and free stream speeds of sound are computed as

$$a = 49.0 \sqrt{T_{t_\infty}/(1 + .2\ M^2)} \quad \text{fps}$$

$$a_\infty = 49.0 \sqrt{T_{t_\infty}/(1 + .2\ M_\infty^2)} \quad \text{fps}$$

The local and free stream velocities are then

$$V = M\ a$$

$$V_\infty = M_\infty\ a_\infty$$

and the local velocity components are

$$V_x = V \cos\alpha$$

$$V_c = V \sin\alpha$$

$$V_r = V_c \cos\theta_{VC}$$

$$V_\theta = V_c \sin\theta_{VC}$$

The probe 2 data was then transposed to the same quadrant as probe 1 assuming symmetry about the leeward centerline. The model roll misalignment of 2.5° present in the TWT 535 data results in probe 1 and probe 2 data being located at off-nominal meridional positions as indicated in the table below.

Model Roll Angle, ϕ	Probe 1 Meridian, θ	Probe 2 Meridian, θ	Nominal Meridian, θ
2.5	177.5	182.5	180
10.0	170.0	175.0	172.5
17.5	162.5	167.5	165.0
--	--	--	--
--	--	--	--
92.5	87.5	92.5	90.0

The data for each probe was interpolated to the nominal meridional positions using a third order Lagrangian interpolation routine. The two meridional positions near the leeward centerline were reflected about the centerline to yield two additional locations for interpolation. The local flow properties which were interpolated were the individual velocity components, V_x, r, θ, the local speed of sound and the local total pressure. The interpolated values were then used to compute additional local flow properties

$$\alpha = \tan^{-1}\left(\sqrt{V_r^2 + V_\theta^2}/V_x\right)$$

$$\theta_{vc} = \tan^{-1}(V_\theta/V_r)$$

$$V = \sqrt{V_x^2 + V_r^2 + V_\theta^2}$$

$$M = V/a$$

$$P/P_\infty = (1 + .2M^2)^{-3.5}(1 + .2M_\infty^2)^{3.5}\ (Pt/Pt_\infty)$$

$$C_p = (P/P_\infty - 1)/.7M_\infty^2$$

The circulation strength $\Gamma/\pi DV_\infty = \oint \vec{V} \bullet d\vec{s}$ was calculated for each cell defined by 4 adjacent flow survey points (interpolated to the nominal meridional locations) assuming linear velocity distribution between points, and the average vorticity for each cell computed as $\omega D/4\ V_\infty = (\Gamma/\pi DV_\infty)/(4\Delta A/\pi D^2)$ where ΔA is the area of the cell. The total circulation strength is then computed as the sum of the circulation strengths for all cells in the flow survey plane.

Output of the computer program consists of listings of the local flow properties and circulation strengths, vector plots of the local crossflow velocities and local angle of attack, and contour plots of the various local flow properties.

The contour plots generate points $(r/D, \theta)$ at which a local flow property exists at some specified level. This is accomplished by fitting curves (third order Lagrangian) as a function of θ for each r/D and as a function of r/D for each θ, and then using these curve fits to generate a set of the local flow properties at an expanded set of r/D, θ. This expanded set is then searched using linear interpolation for the set of r/D, θ at which the specified values of the local flow property exist. The sets of r/D, θ are then plotted as points using a different symbol for each contour level.

RESULTS

The results of the flow survey tests are presented as flow field contour plots of the local Mach number (M), pressure coefficient (Cp), total pressure ratio (P_t/P_{t_∞}), and vorticity ($\omega D/4V_\infty$), and vector plots of the local crossflow velocity ($V_c/V_\infty \sin\alpha_\infty$). Total circulation strength and vortex centers are also presented and compared with appropriate available data. A complete listing of the computed data is given in the appendix to this report.

The flow field contour plots are shown in figures 6 through 17. These contour plots were generated by tracing curves through the computer generated contour point plots. All points generated were used except where contour levels are too close together to be easily distinguishable or where the flow property is varying so slightly that the basic data scatter does not produce meaningful contour levels. An example of the latter is that zero levels of local vorticity are generally not shown as much of the flow field is at or near zero vorticity and an erratic set of points is generated by the normal data scatter.

Vorticity Contours

The vorticity contour plots are shown in figures 6 through 8. At Mach number 0.8, Re = $4.4 \times 10^6 ft^{-1}$, the vorticity contours clearly show the location and strength of the forebody vortex at X/D = 3.5, 4.1, and 4.8 for both 20.1 and 24.6° angle of attack. The maximum vorticity levels are approximately the same at α = 20.1° and 24.6° but the vorticity is distributed over a larger area at α = 24.6° and represents a greater total circular strength. At X/D = 6.5, the forebody vortex is poorly defined, having "burst" somewhere aft of X/D = 4.8. The beginning of an aftbody vortex system appears to be present at X/D = 4.8 at $\theta \cong 120°$. This second vortex has begun to "roll-up" and is somewhat better defined at X/D = 6.5, but is still too close to the body to be well defined by the survey r/D, θ array. The minimum r/D survey location is approximately one probe diameter off the surface (.06 in) for all survey stations at Mach number 0.8 conditions and this data may be affected to some extent by probe/body interference and axial flow separations.

The negative vorticity levels near the body at x/D=4.8, $\theta \cong 150°$ are attributed to the probe being immersed in a separated axial flow at the most inboard radial probe position and these azimuth angles. The existence of this separated flow region is indicated by the local flow properties in this region and is discussed in later sections. The negative vorticity levels near the body and just above the side meridian at some stations is attributed to probe/body interference and/or basic data accuracy.

The vorticity distributions for Mach number 0.8, Re = 7.9 X 10^6ft.$^{-1}$, are generally similar to the Re = 4.4 X 10^6FT^{-1} results with maximum vorticity levels somewhat lower and distributed over a smaller area.

The vorticity distributions for Mach number 1.96, α = 10°, show a distinct vortex center present only at the most aft station, X/D = 6.5. At α = 14.5°, the vortex at X/D = 6.5 has increased in strength and the regions of vorticity at the forward stations have expanded and increased in strength. At α = 20.3°, the forebody vortex is well defined at all stations except X/D = 4.4 where the most inboard survey is two probe diameters (.12 in.) from the body surface and it appears that a significant quantity of circulation lies inboard of this radius. The forebody vortex at X/D = 6.5 is not as well defined at α = 20.3° as it was at α = 14.5° and appears to have two centers, although this could be a result of data accuracy at the low vorticity levels in this region. A second region of concentrated vorticity is apparent near the body and appears to be the beginning of an aft body vortex system. At α = 24.8°, there is a general increase in the size of the regions of vorticity with maximum levels remaining about the same as at α =20.3°.

Total Pressure Contours

Total pressure contours are presented in figures 9 through 11. Total pressure contours are also a good indication of regions of vorticity as the vortex feeding sheet, originating at the point of crossflow separation on the body, carries with it low energy boundary layer air which rolls up with the feeding sheet into the vortex core.

At Mach number 0.8 , the similarity of the total pressure contours to the vorticity contours is very apparent. Minimum total pressures within the vortex cores are on the order of 80 to 90% of freestream total pressure at most survey stations and are as low as 60% at the most aft station for α = 20.1°, Re = 4.4 X 10^6ft^{-1}. The total pressure contours at X/D = 4.8 are distorted by the presence of a region of a very low total pressure near the body at $\theta \cong 150°$. These low total pressures, in combination with the very low static pressures and Mach numbers noted below, are indicative of a region of separated flow.

The local total pressure contours at M = 1.96, α = 10.0° again are similar to the corresponding vorticity contours with the exception of the low total pressure cells at X/D - 4.1, 4.4, 4.8 near r/D = .5, .8, 1.3 respectively. These low total pressures, approximately 80% of freestream total pressure at X/D = 4.4 and 4.8, are near normal-shock-loss values for M_∞= 1.96 (P_{t2}/P_{t1} = .74) and cannot be true flow field values. These low total pressures have been correlated with other flow field properties and are found to be associated with the frustum shock wave. At flow field locations where the probe head is in close proximity to the frustum shock, the flow is very non-uniform with respect to the probe size and use of the uniform flow field calibration data leads to spurious trends for local flow properties. Local flow properties in the vicinity of the frustum shock wave should therefore be used with caution.

The total pressure contours at the higher angles of attack are again similar to the corresponding vorticity contours with the exception of the regions of probe/shock interaction noted above. The local total pressures in the vortex cores are very low at $M_\infty = 1.96$, with minimum values on the order of 30 to 40% of freestream total pressures. Although local total pressures near the body are also quite low at some locations, the corresponding local velocities are not low and no axial flow separation is indicated for the survey data at $M_\infty = 1.96$.

Local Mach Number and Pressure Coefficient Contours

The local Mach number contours are shown in figures 12 through 14 and the local pressure coefficient contours in figures 15 through 17. Although the local Mach number and pressure coefficients do not directly relate to the vortex motion, they do illustrate the large perturbations from freestream conditions associated with the flow about this configuration and serve to complete the description of the flow field.

The low pressure coefficients ($C_p \cong -.6$) and the low Mach numbers ($M \cong .4$) at $x/D = 4.8$, $\theta \cong 150^\circ$ are evident at both Reynolds numbers for $M_\infty = 0.8$. These flow properties, in conjunction with the low total pressures are indicative of axial flow separation noted earlier. It should be noted also that probe calibration characteristics were linearly extrapolated for local Mach numbers less than 0.6 and actual local Mach numbers may be lower than the calculated values for these conditions.

At $M_\infty = 1.96$, the presence of the frustum shock is again evident but is not clearly defined because of the probe/shock interactions noted earlier. No indications of axial flow separation are present for any conditions at $M_\infty = 1.96$.

Local Crossflow Velocity Vectors

The local crossflow velocity vectors, $V_c/V_\infty \sin \alpha_\infty$, are shown in figures 18 through 20. These vector plots illustrate many of the features of the leeside crossflow velocity field in the presence of vortices, including the crossflow separation at the body, the vortical motion about the vortex center, the leeward meridian stagnation point, and the reverse circumferential flow (i.e. away from the leeward meridian) on the lee side near the body.

The above features are typical for all of the $M_\infty = 0.8$ conditions, figures 18 and 19. The region of axial flow separation at $x/D = 4.8$, noted earlier results in large local velocities directed toward the body centerline and cannot be considered realistic.

The local crossflow velocity vectors for $M_\infty = 1.96$ are shown in figure 20. These velocity fields are similar to $M_\infty = 0.8$ conditions except that discontinuities in the velocity field due to the frustum shock and expansions are evident.

Circulation Strength

The total circulation strength was determined by summing the circulation strengths associated with each cell defined by four adjacent flow survey locations $(r/D, \theta)$ over the lee side quadrant at a given survey station. This summation, as a function of the inboard integration limit, is shown in figures 21 through 23. These plots illustrate the radial distribution of circulation strength and were also used as a basis for extrapolation to the body surface. Data for $\alpha_\infty = 10^\circ$, $M_\infty = 1.96$ is not shown as the circulation strengths at this condition were negligible.

The total circulation strength as a function of body station is illustrated in figures 24 and 25 for the summation over the measured r/D limits and the extrapolation to the body surface. The data of Jorgensen (ref. 3) and Tinling (ref. 4) derived from measured normal force distributions and vortex centers is compared with the present data at comparable conditions. The agreement with Tinlings and Jorgensens data is not unreasonable considering the difference in the methods of obtaining the data.

The effect of the frustum on the axial distribution of total circulation strength is generally to prevent or delay the normal increase in circulation strength with body station. The overall trends of total circulation strength with body station, Mach number and Reynolds number are qualitatively in agreement with the crossflow drag analysis of reference 2. A quantitative correlation of the results of the present data would require a much more detailed analysis than is possible in this report and should include an evaluation of the effects of probe/body and probe/frustum-shock interactions, separation of the circulation strengths associated with the vortex cores and feeding sheets, and an extrapolation of circulation strength to the body based on analysis of local velocities.

Vortex Centers

The vortex centers determined from evaluation of the vorticity contour plots is shown in figures 26 and 27. These data are also compared with Tinling's and Jorgensen's data and show good areeement at the appropriate conditions. For some conditions at $M_\infty = 1.96$, the vortex center was not well defined by the vorticity distributions and local total pressure distributions were used to locate the vortex centers.

CONCLUSIONS

The results presented in this report serve to define the local flow field properties, vorticity distributions, total and local circulation strengths and vortex centers at various stations on an ogive-cylinder-frustum-cylinder at angles of attack to 25 degrees for Mach numbers 0.8 and 1.96. The data shows a vortex system which developes on the forebody and proceeds downstream over the frustum and aft cylinder, growing in size but with decreasing maximum vorticity levels. The initial development of an aftbody vortex system can be observed at the most aft survey condition.

The total circulation strength and the vortex center at the forebody measuring station showed reasonable agreement with previously published data for the same forebody shape and at comparable conditions. The axial distribution of total circulation strength indicates that the effect of the frustum is to prevent or delay the normal increase in circulation strength which would be expected for smooth bodies.

Some regions of negative vorticity, i.e. rotation in the opposite sense of the primary vortex motion, was observed near the body at some body stations. One region, on the lee side at a body station just downstream of the frustum, is attributed to the presence of an axial flow separation bubble at the Mach number 0.8 conditions. Other regions of negative vorticity are generally attributed to probe/body interference and/or basic data accuracy.

RECOMMENDATIONS

It is recommended that the data presented in this report be further analyzed to evaluate the relative strengths and locations of the vortex systems and their feeding sheets so as to allow for evaluation of theoretical flow field models. Additional analysis of results at the most inboard locations should be undertaken in order to evaluate the possible effects of probe/body interference on this data, although tests on larger models may be required to adequately define the flow in this region. The effects of the axial flow separation bubble just downstream of the frustum at Mach number 0.8 should also be investigated further as it undoubtedly has a dominent influence on the flow in this region.

REFERENCES

1. Chianese, F. "Results of an Experimental Investigation to Obtain Surface Pressure Distributions on Four Models - Two Variable Cross Sections of Two Different Scales." CCSD TN-AP-68-368, November 1968.

2. Foley, J.E., "Results of a Study of Mach Number and Reynolds Number Effects on the Crossflow Drag Characteristics of Ogive-Cylinders and Ogive-Cylinder-Frustum-Cylinders at Angles of Attack to 30 Degrees." CCSD TN-AP-71-527, October 1971.

3. Jorgensen, L. H. and Perkins, E. W. "Investigation of Some Wake Vortex Characteristics of an Inclined Ogive-Cylinder Body at Mach Number 2." NASA Report 1371, 1958.

4. Tinling, B. E. and Allen, C. Q. "An Investigation of the Normal-Force and Vortex Wake Characteristics of an Ogive-Cylinder Body at Subsonic Speeds." NASA TN D-1297, April, 1962.

5. Foley, J. E. "Results of a Test to Determine the Feasibility of Use of Two Miniature Flow Direction and Velocity Measuring Probes at Subsonic and Supersonic Speeds." CCSD TN-AP-70-462, June 1970.

6. Simon, E. "The George C. Marshall Space Flight Center's 14x14 Inch Trisonic Wind Tunnel Technical Handbook." NASA TM X-53185, December 1964.

7. Foley, J. E. and Hull, J. J. "Computer Program CN0073, Flow Field Data Reduction and Analysis Program." CCSD TN-AP-70-465, April 1970.

MODEL NOSE LENGTH	
X/D	L
3.5	5.00
4.1	5.60
4.4	5.90
4.8	6.30
6.5	8.00

NOTE: All dimensions are in inches

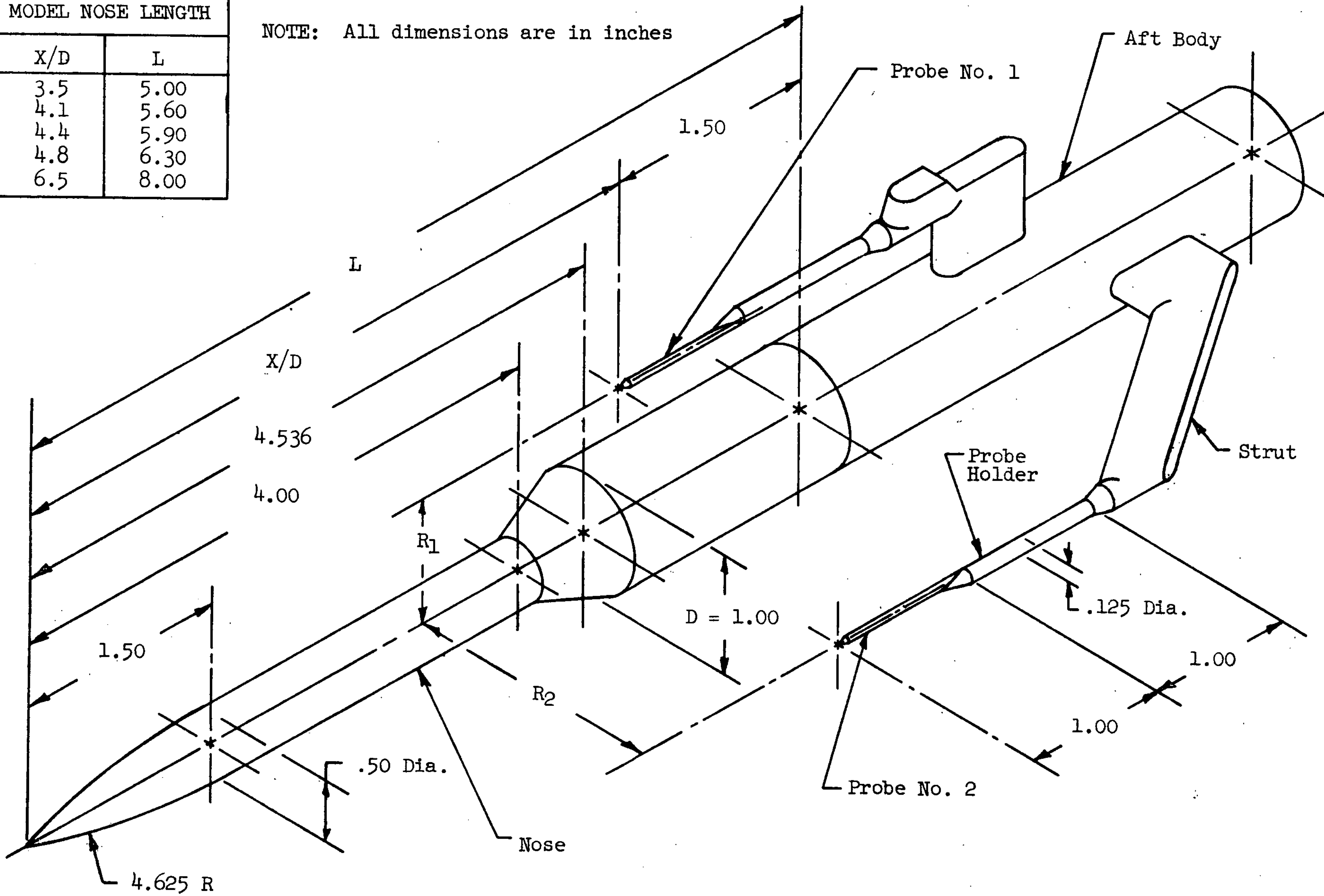

Figure 1. Model Configuration with Typical Probe/Strut Installation

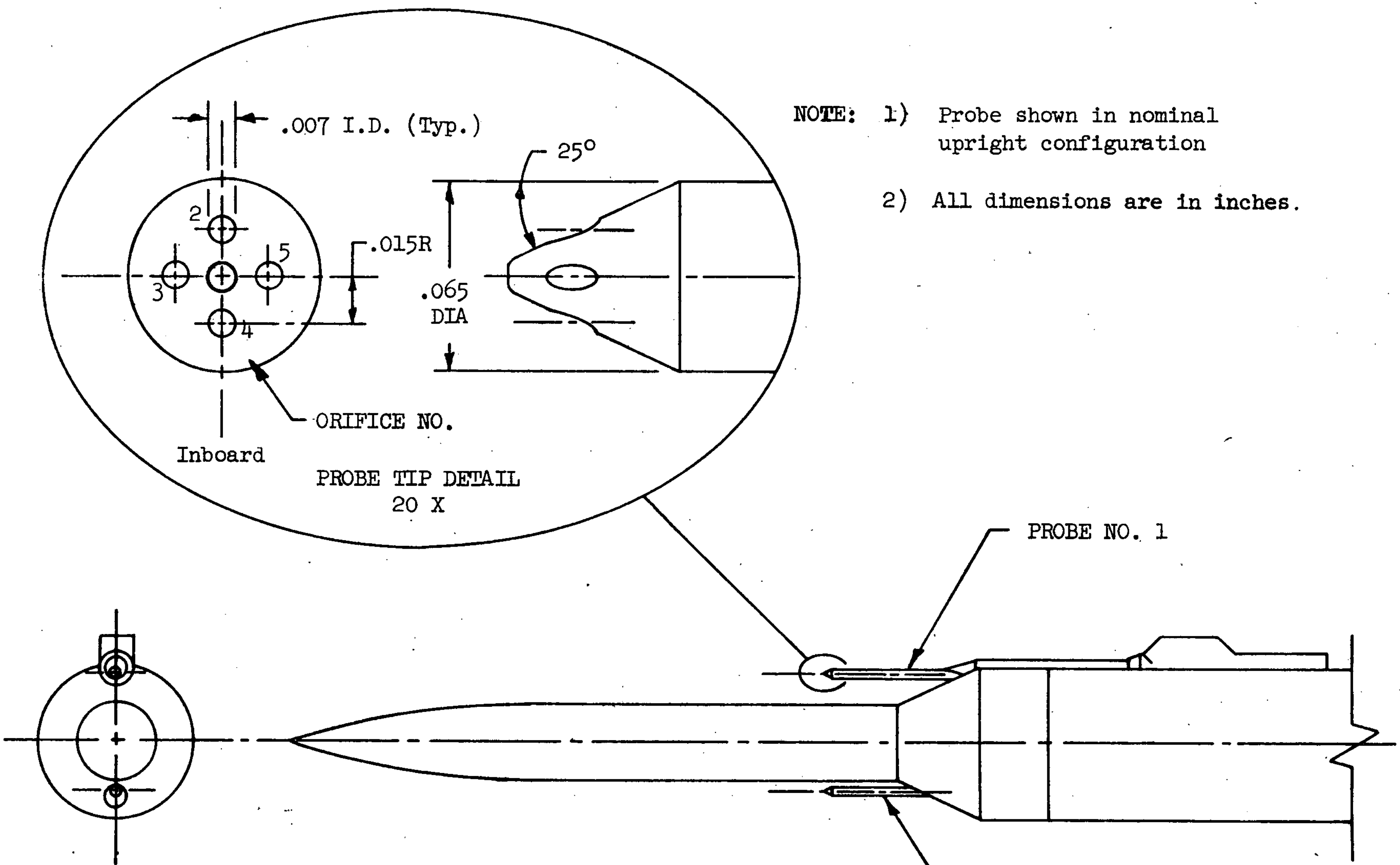

NOTE: 1) Probe shown in nominal upright configuration

2) All dimensions are in inches.

Figure 2. Probe/Strut Installation for Inboard Survey Locations and Probe Details

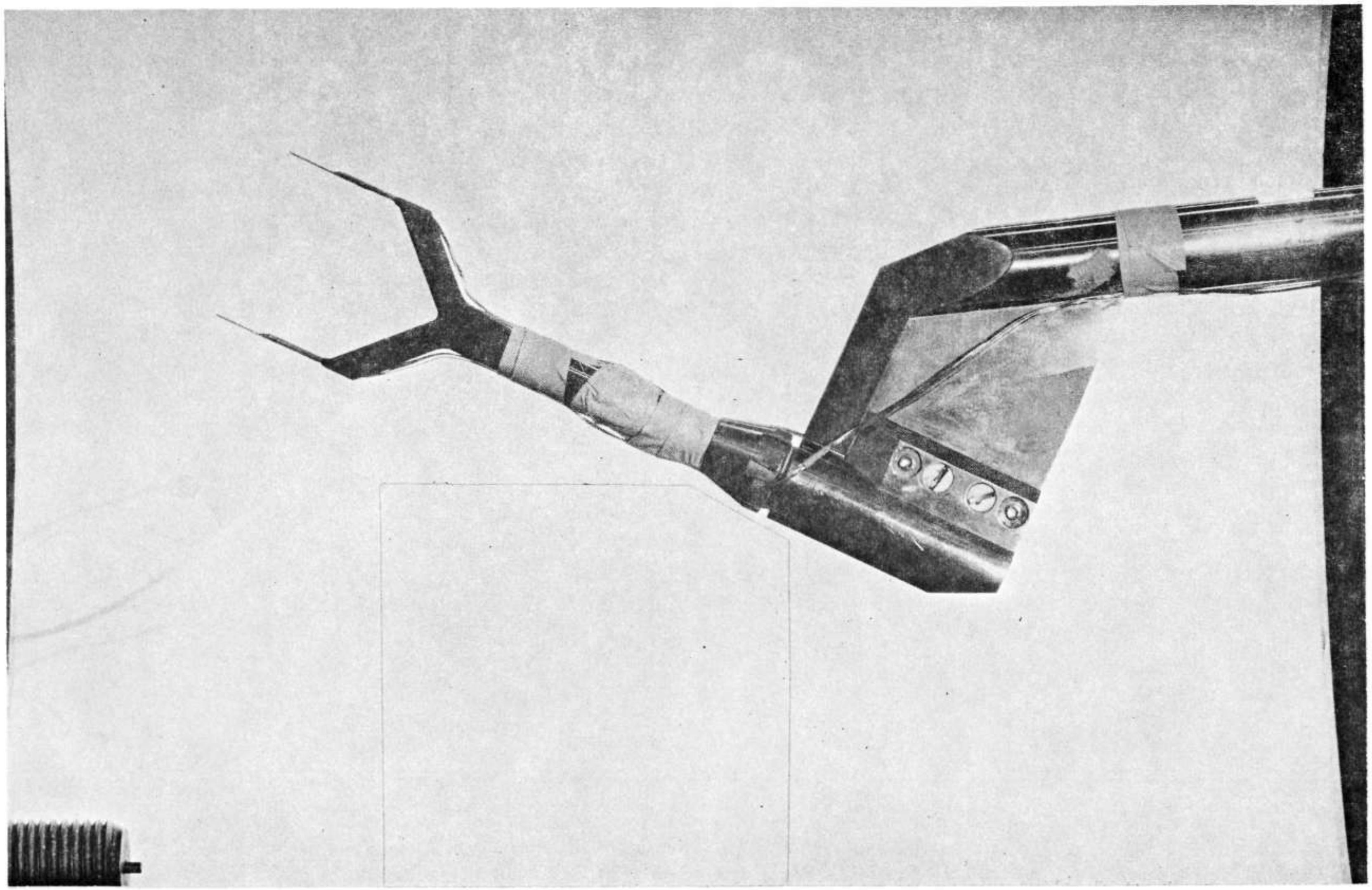

Figure 3. Typical Tunnel Installation Photograph, Probe Calibration Model

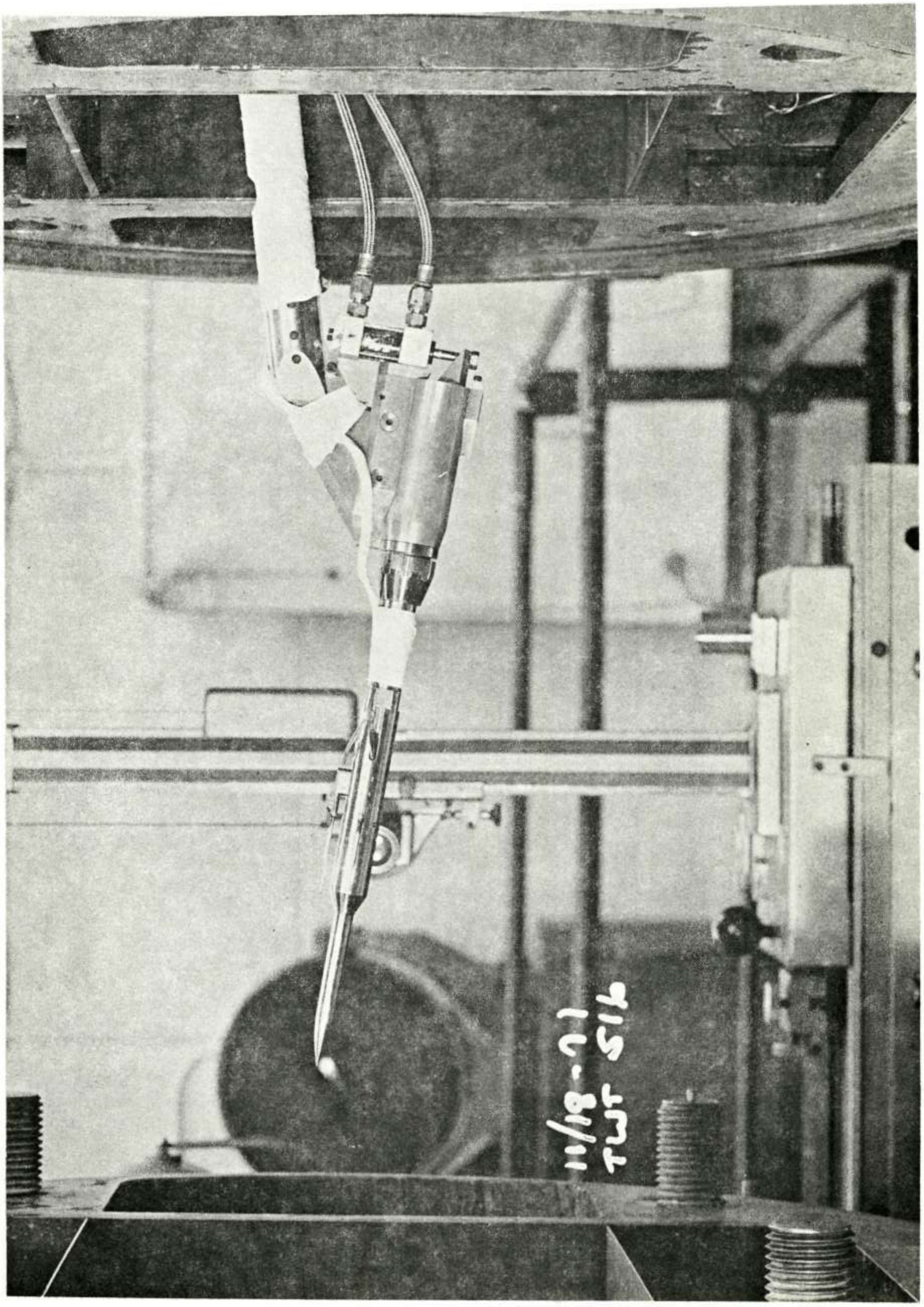

Figure 4. Typical Tunnel Installation Photograph, Flow Survey Model

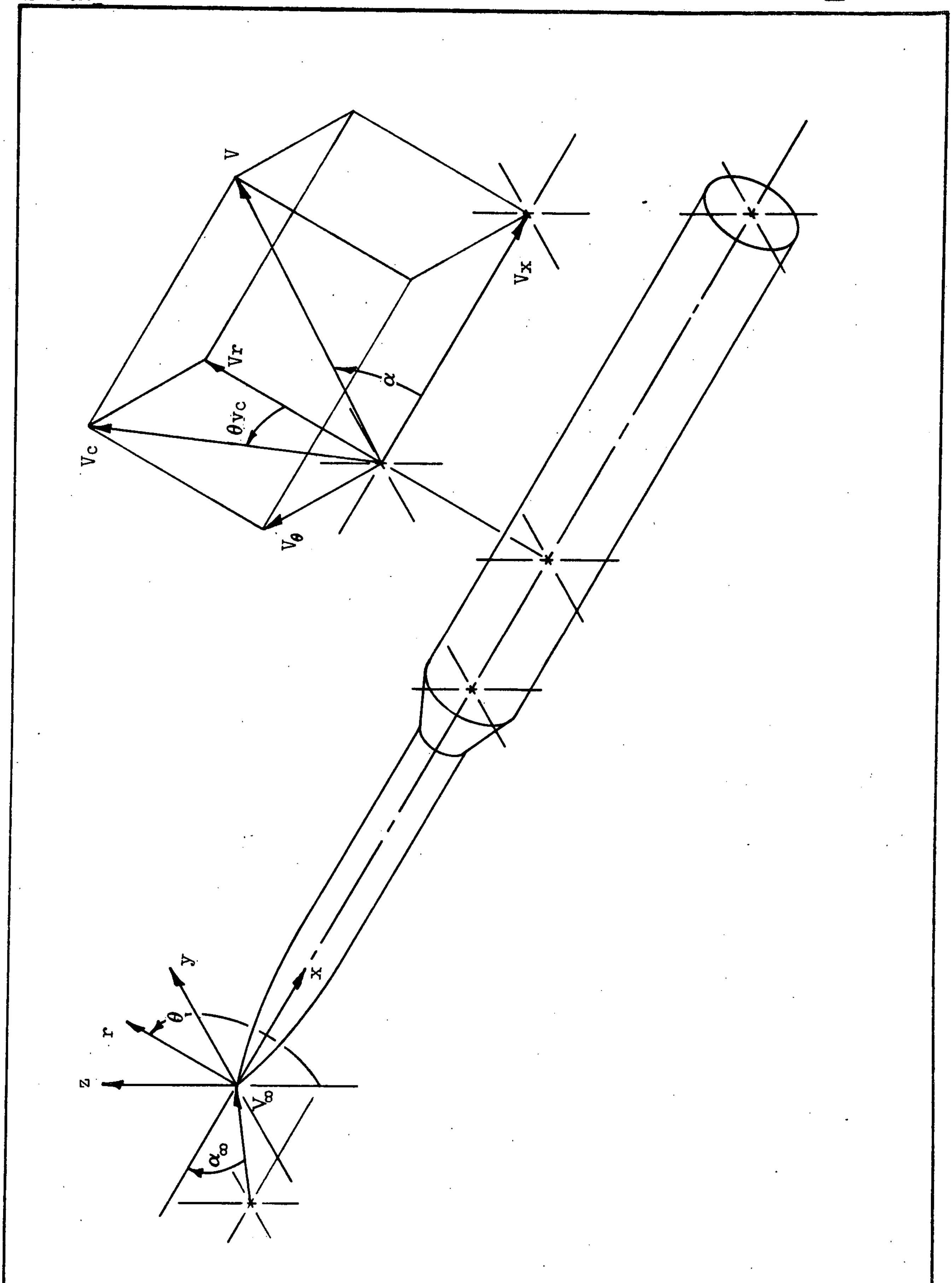

Figure 5. Model Axis Systems

LOCAL VORTICITY $(\omega D/4V_\infty)$

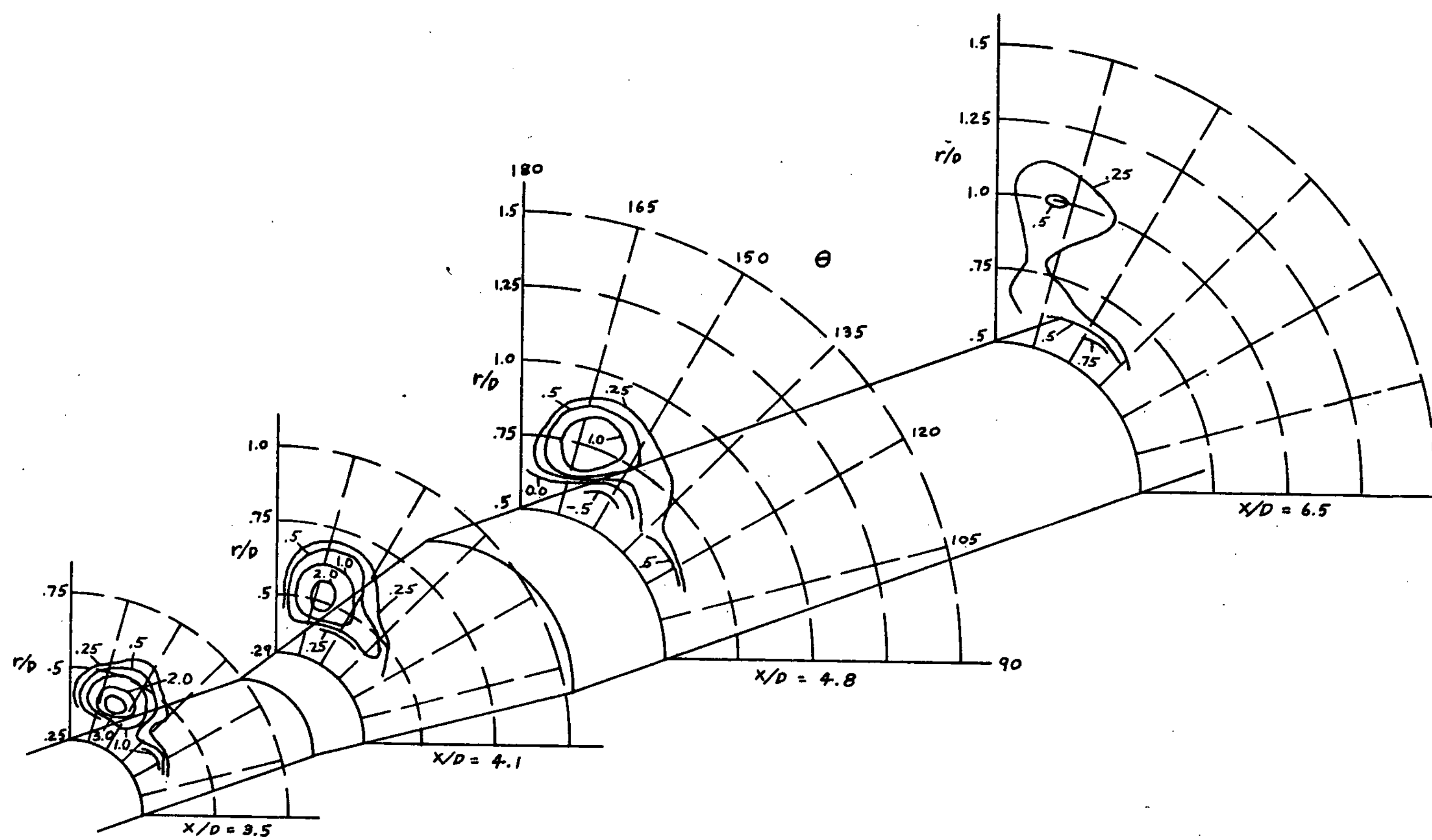

FIGURE 6 - CONSTANT LOCAL VORTICITY CONTOURS (M_∞=0.8, R_e=4.4X10^{6}ft^{-1})

(a) α_∞= 20.1°

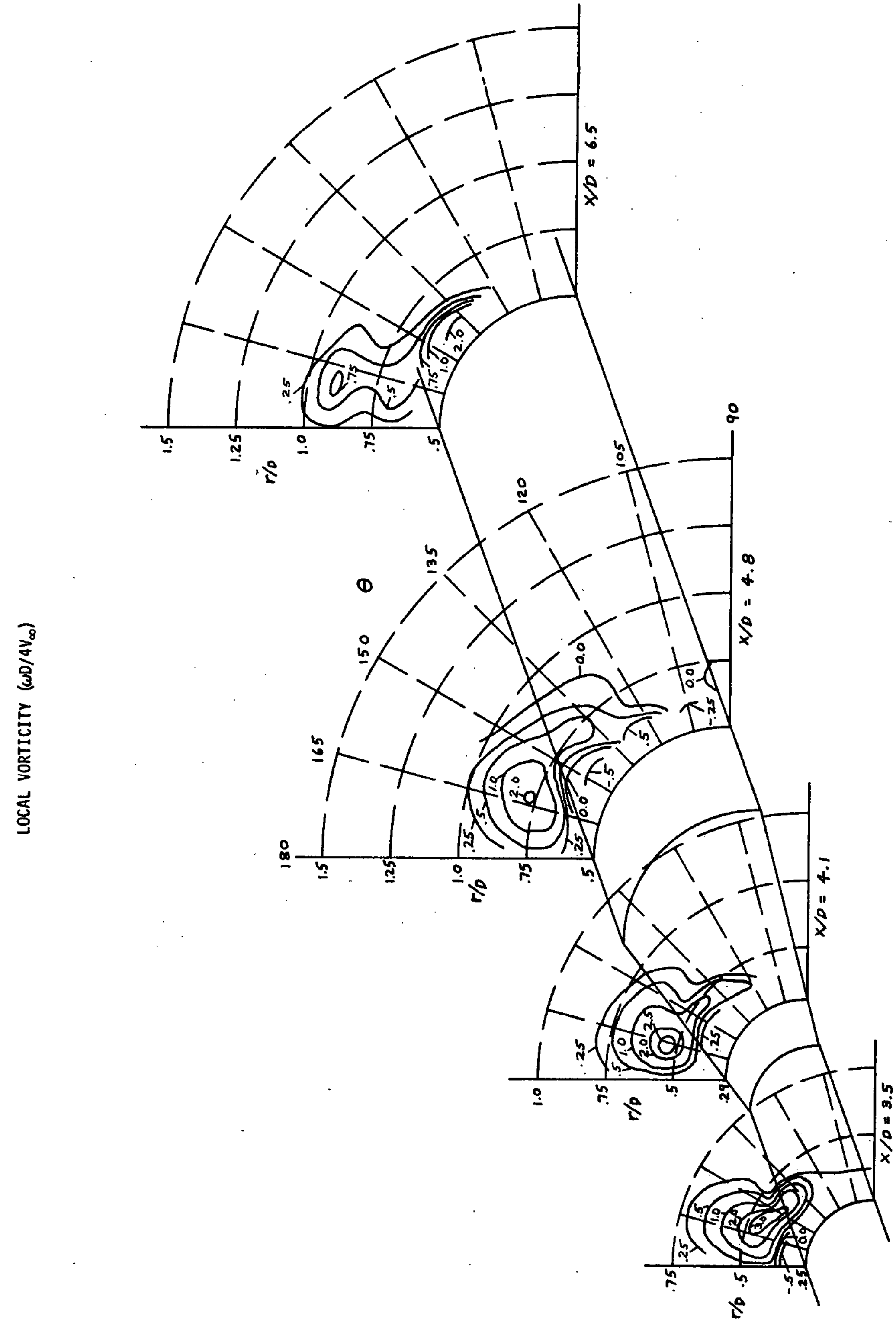

FIGURE 6 - CONSTANT LOCAL VORTICITY CONTOURS (M_∞=0.8, R_e=4.4X$10^6$$ft^{-1}$)

(b) α_∞= 24.6°

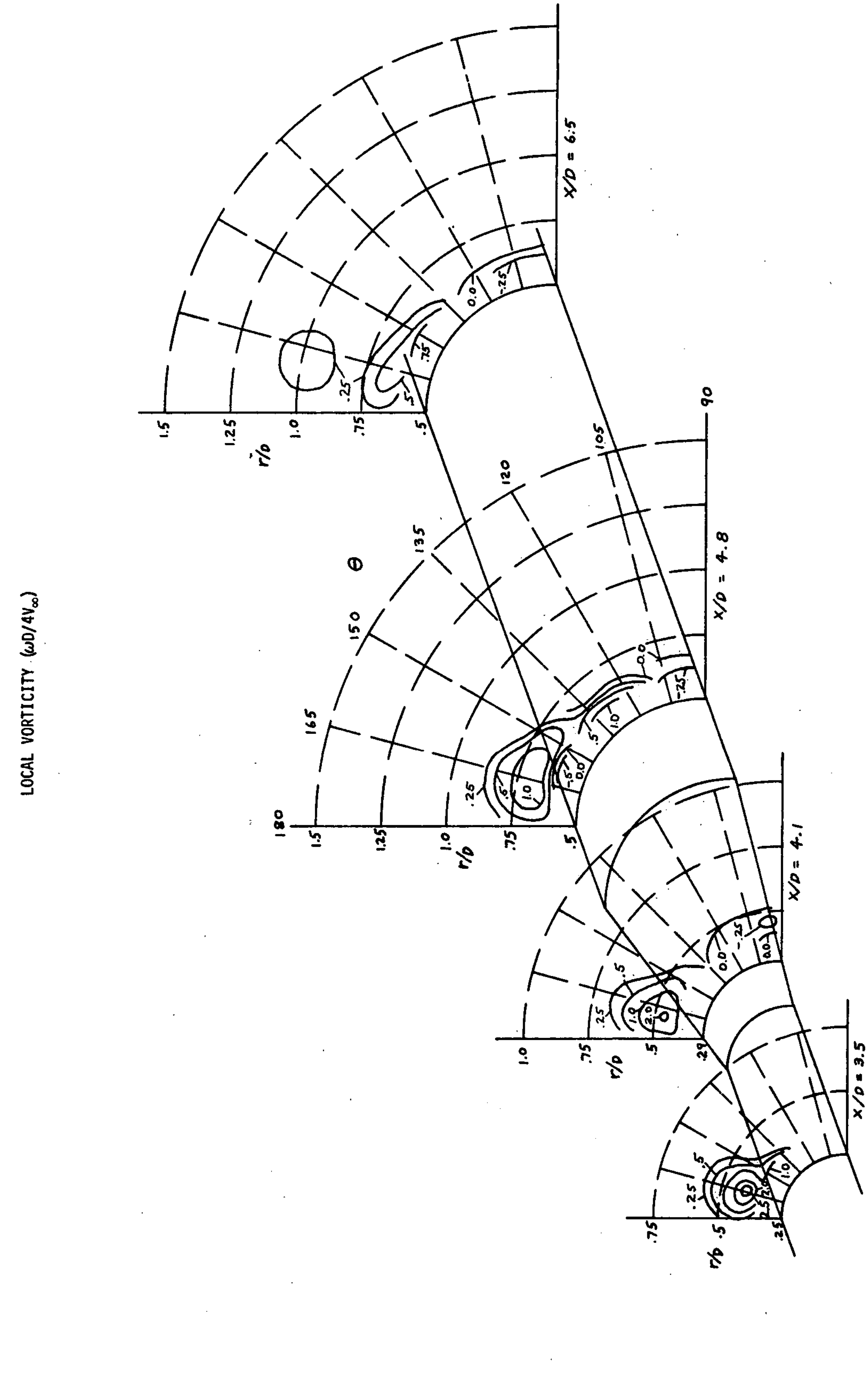

FIGURE 7 - CONSTANT LOCAL VORTICITY CONTOURS (M_∞=0.8, R_e=7.9X10^{6}ft^{-1})

(a) α_∞= 20.1°

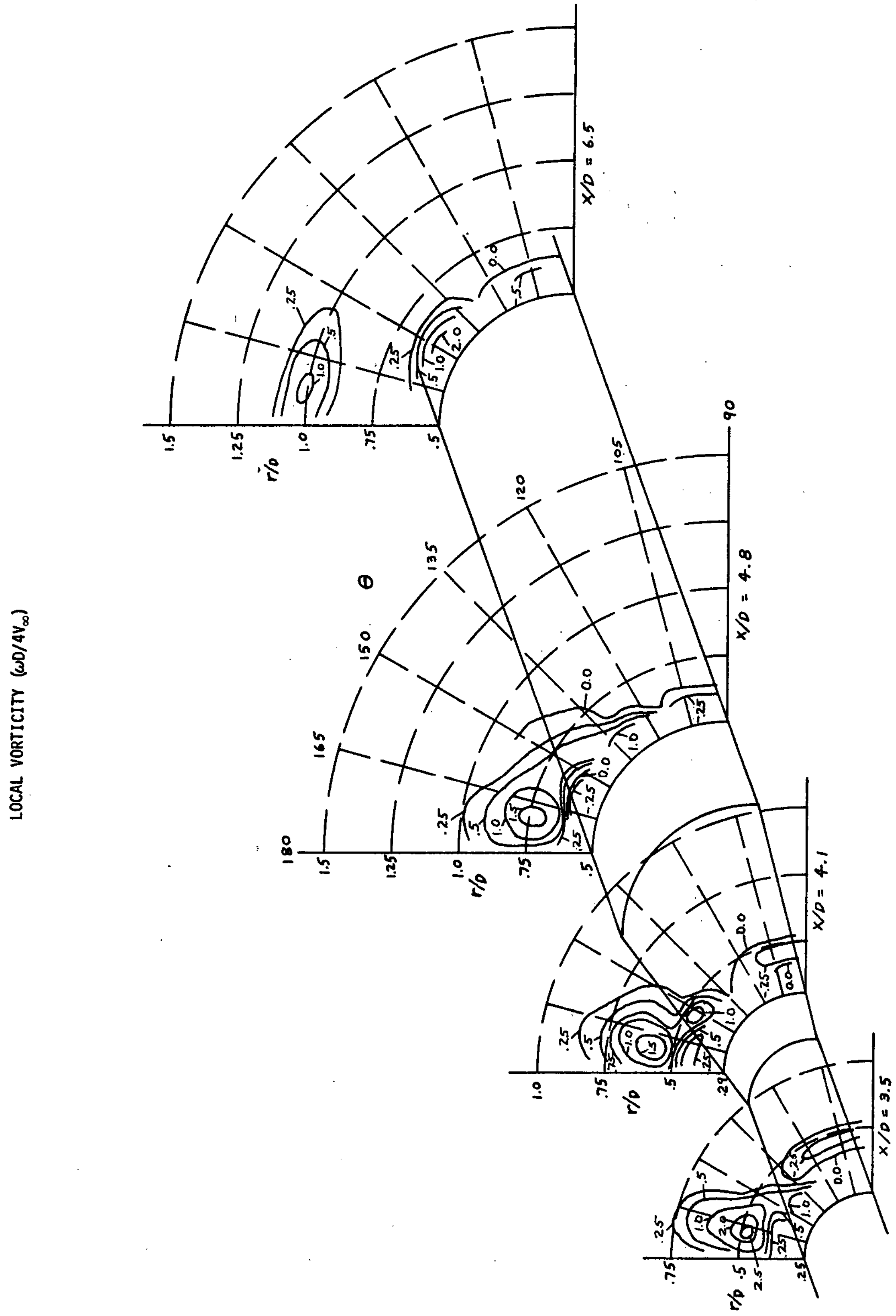

FIGURE 7 - CONSTANT LOCAL VORTICITY CONTOURS (M_∞=0.8, R_e=7.9X10^{-6}ft^{-1})

(b) α_∞= 24.6°

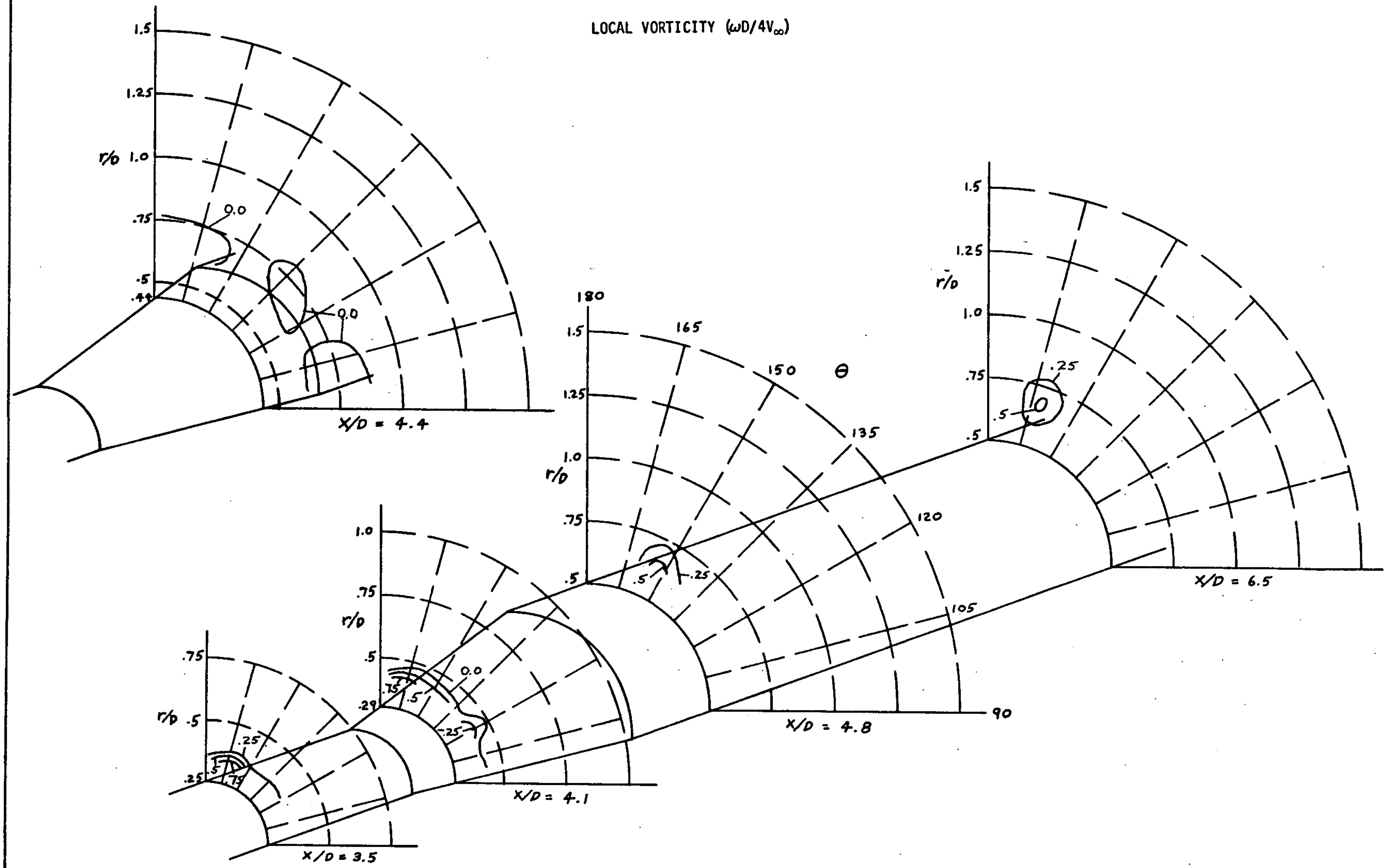

FIGURE 8 - CONSTANT LOCAL VORTICITY CONTOURS (M_∞ =1.96, R_e=9.8X10^{6}ft^{-1})

(a) α_∞= 10.0°

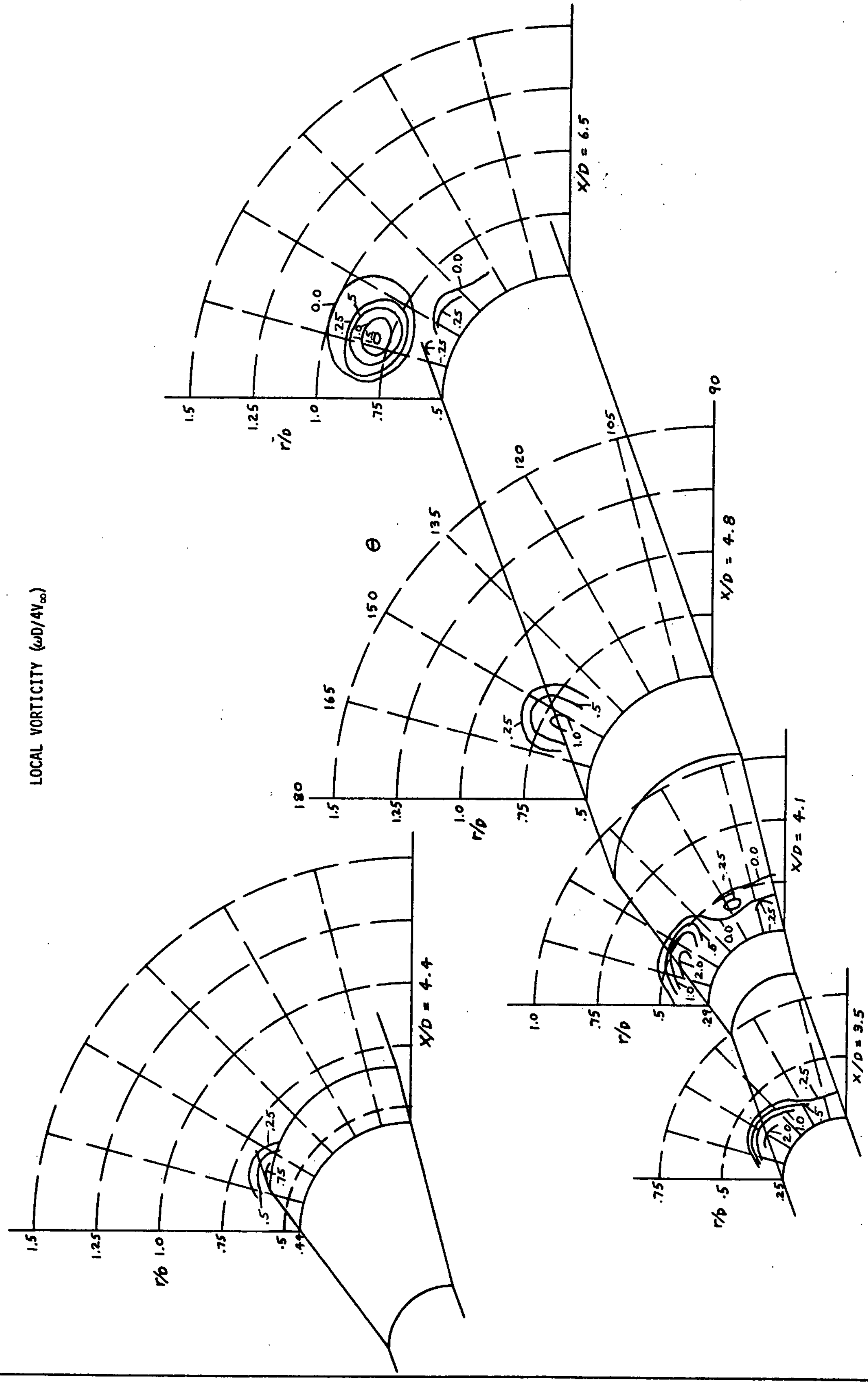

FIGURE 8 - CONSTANT LOCAL VORTICITY CONTOURS (M_∞=1.96, R_e=9.8X10^{6}ft^{-1})

(b) α_∞= 14.5°

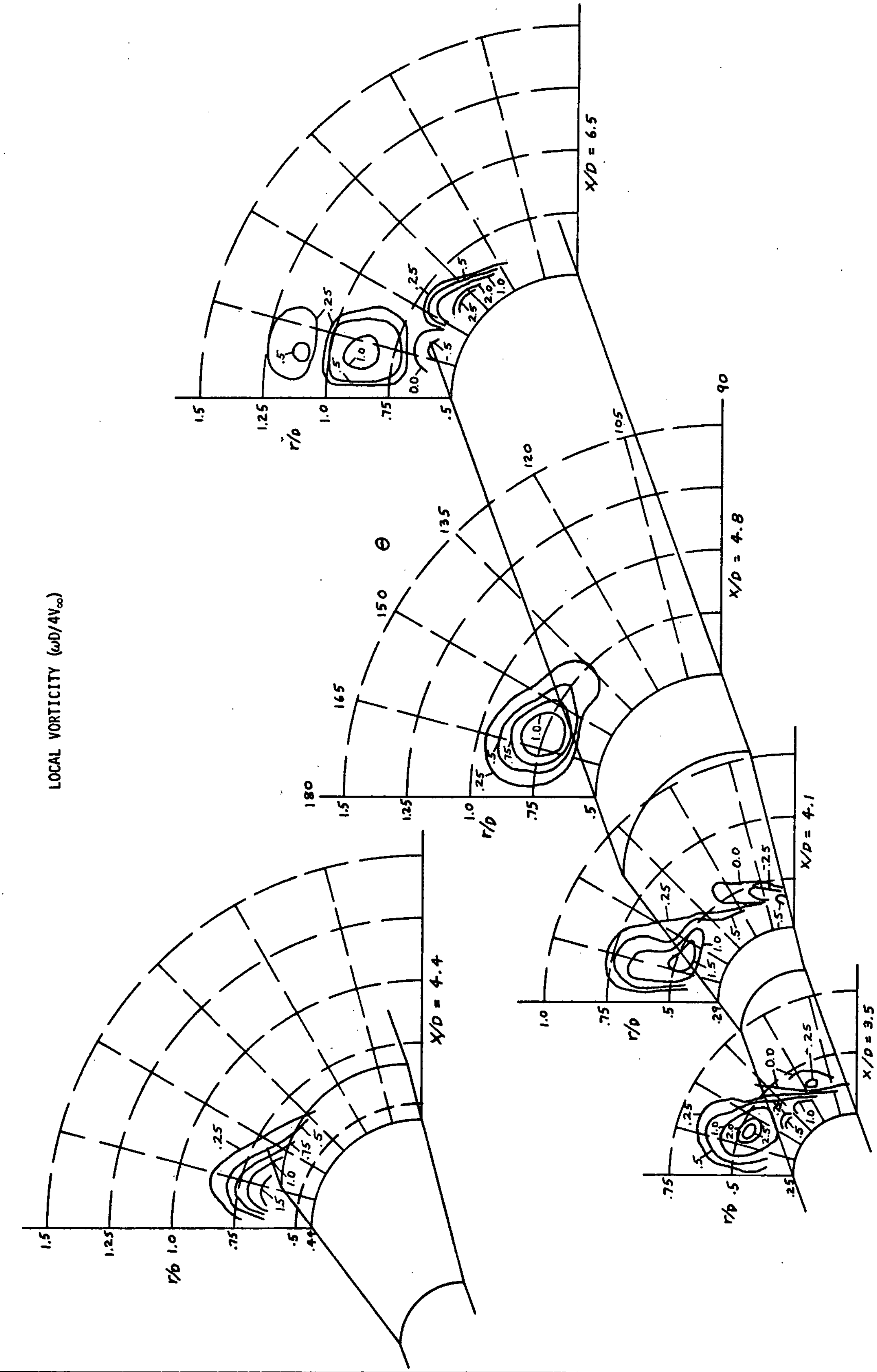

FIGURE 8 - CONSTANT LOCAL VORTICITY CONTOURS (M_∞ =1.96, R_e=9.8X10^{6}ft^{-1})

(c) α_∞= 20.3°

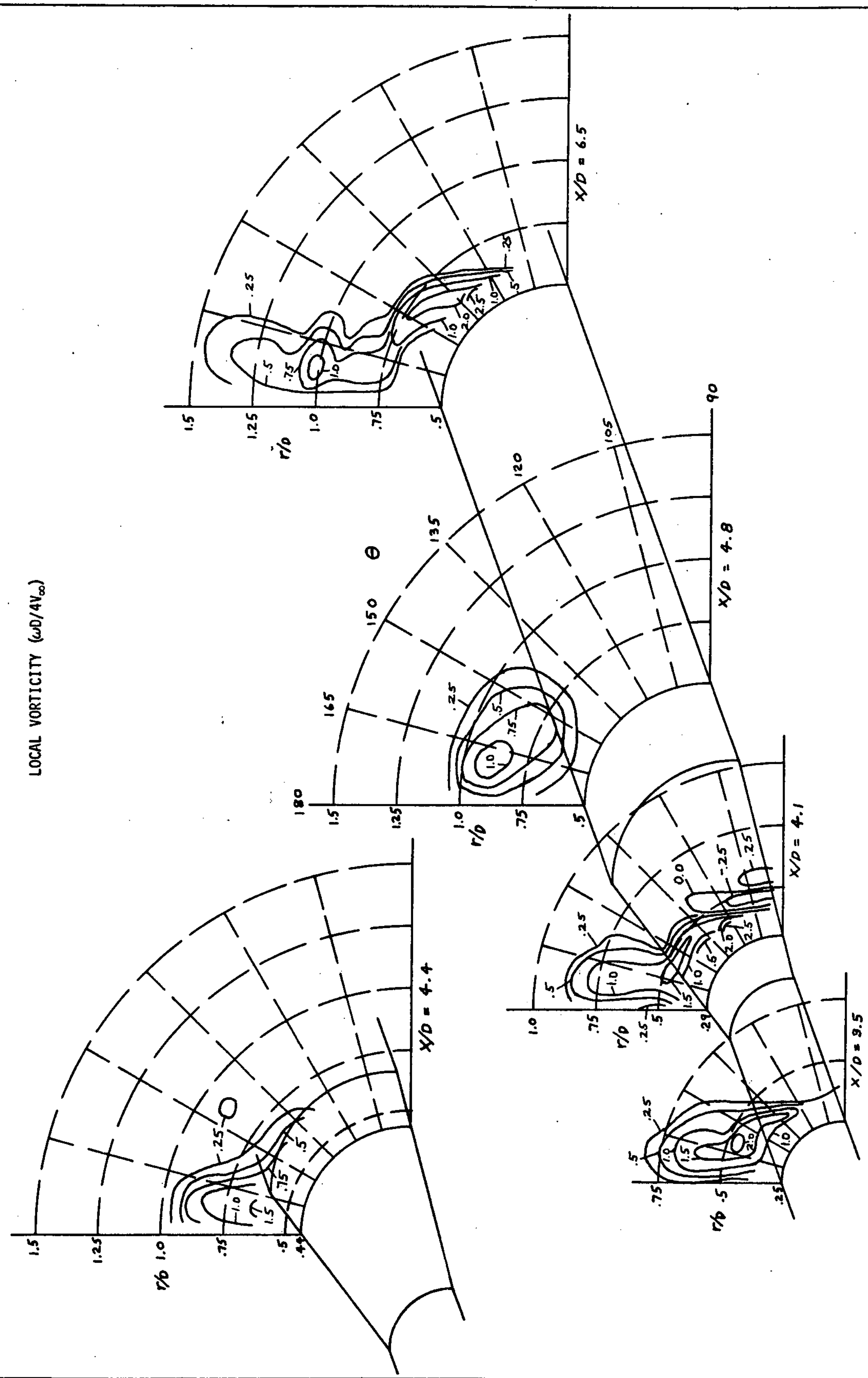

FIGURE 8 - CONSTANT LOCAL VORTICITY CONTOURS (M_∞=1.96, R_e=9.8X10^6ft^{-1})

(d) α_∞= 24.8°

LOCAL TOTAL PRESSURE RATIO (P_t/P_{t_∞})

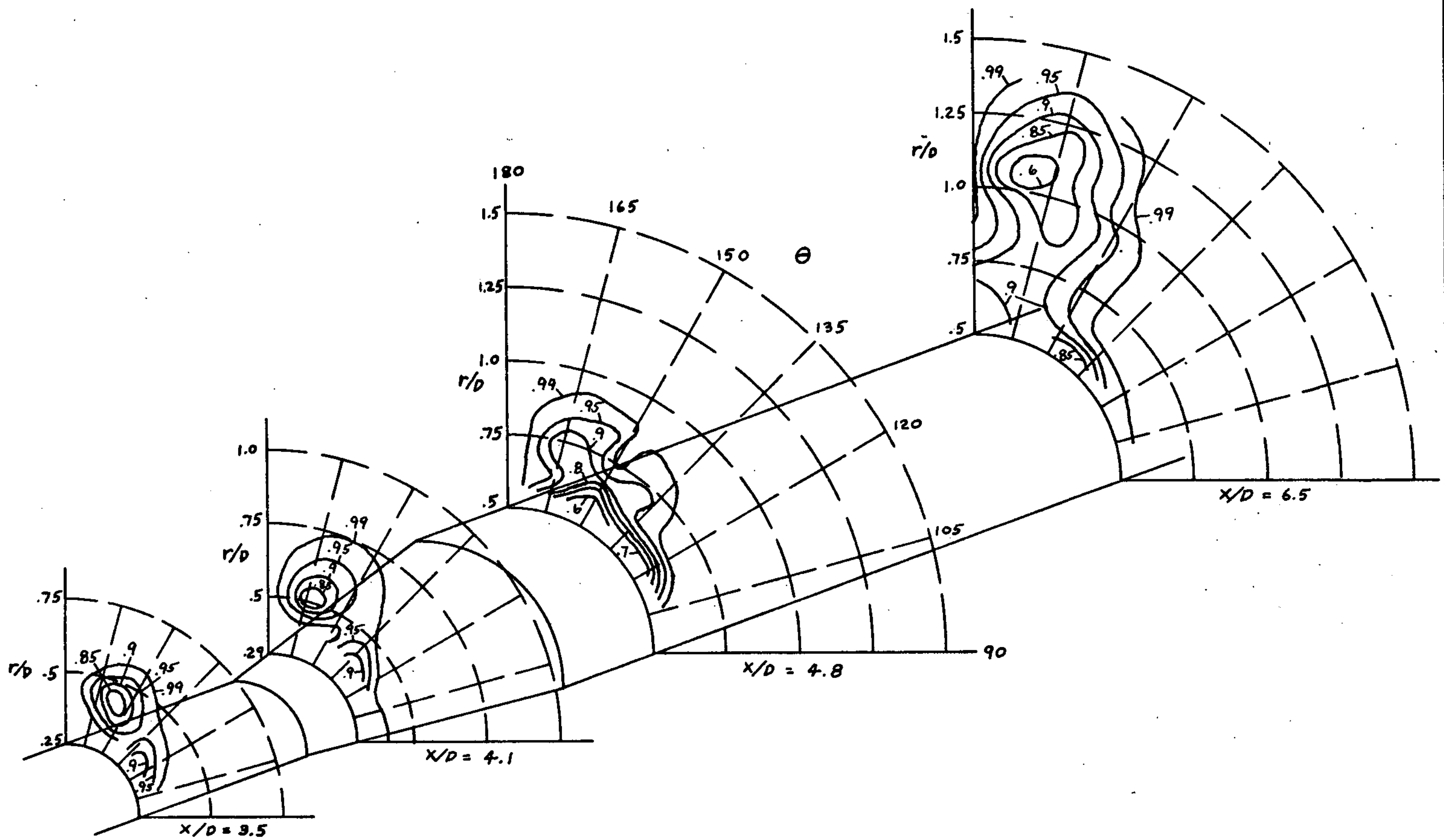

FIGURE 9 - CONSTANT LOCAL TOTAL PRESSURE RATIO CONTOURS (M_∞=0.8, R_e=4.4X10^{6}ft^{-1})

(a) α_∞= 20.1°

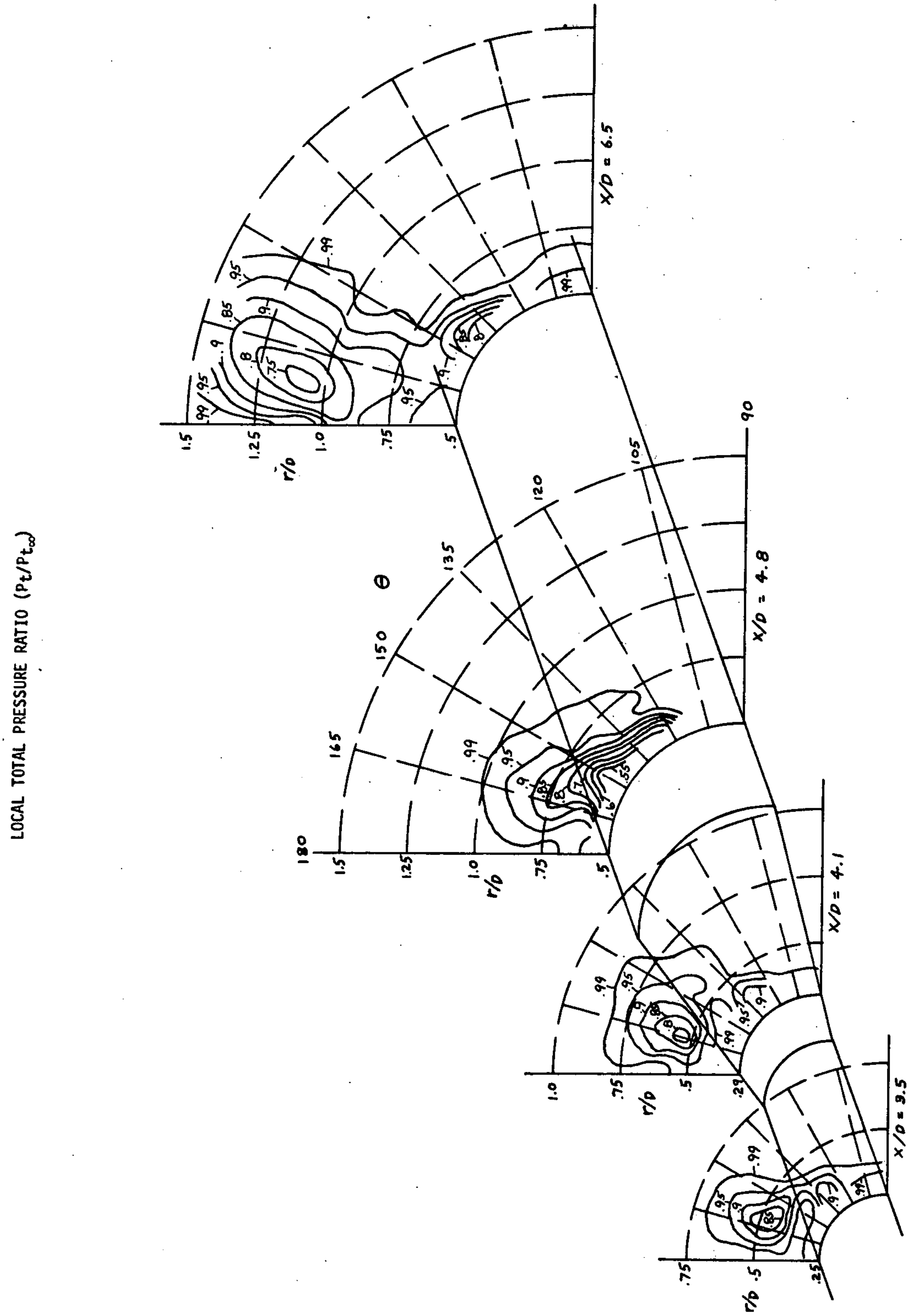

FIGURE 9 - CONSTANT LOCAL TOTAL PRESSURE RATIO CONTOURS (M_∞ =0.8, R_e=4.4X10^{6}ft^{-1})

(b) α_∞= 24.6°

LOCAL TOTAL PRESSURE RATIO (P_t/P_{t_∞})

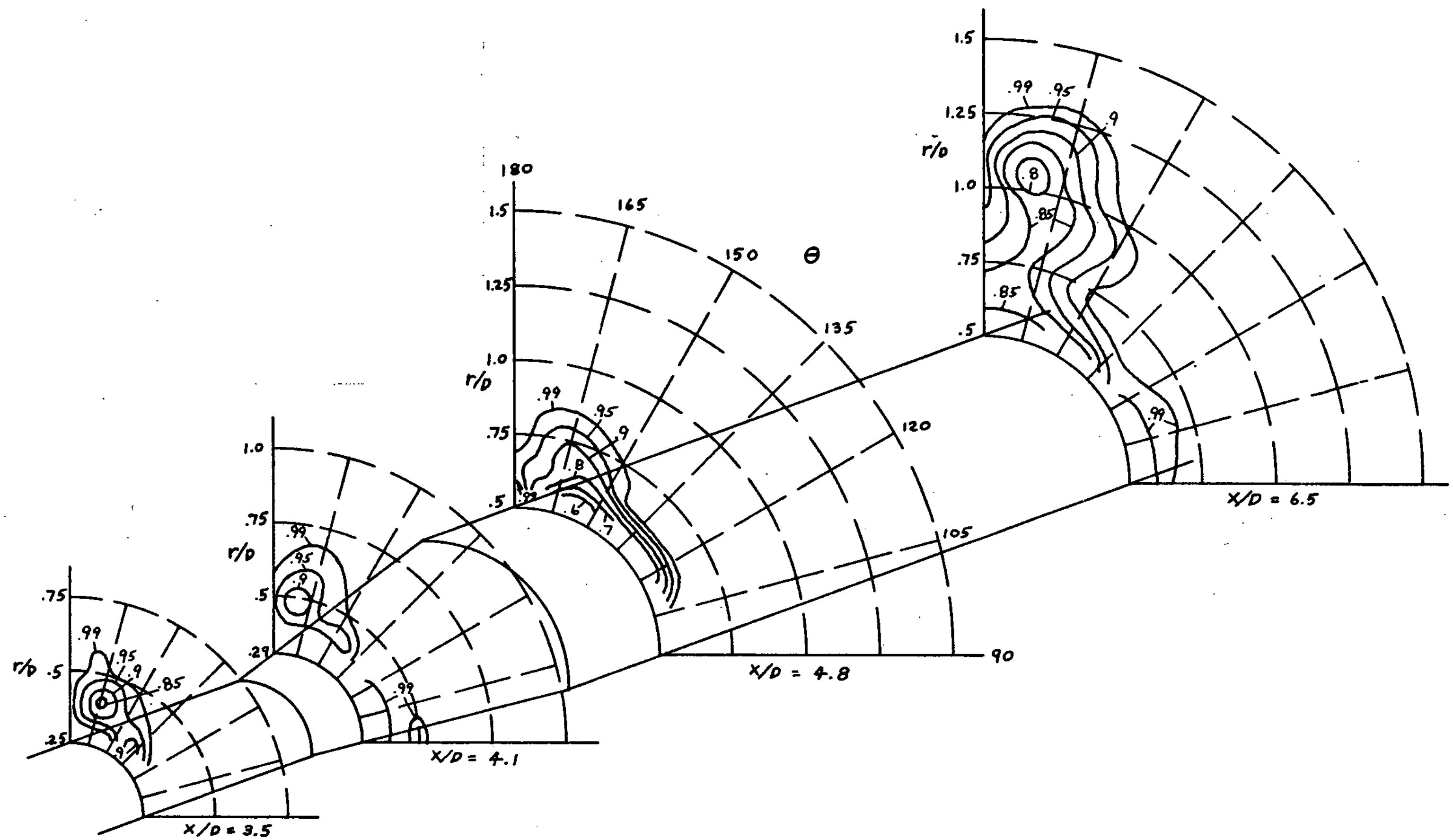

FIGURE 10 - CONSTANT LOCAL TOTAL PRESSURE RATIO CONTOURS (M_∞=0.8, R_e=7.9X10^{6}ft^{-1})

(a) α_∞= 20.1°

LOCAL TOTAL PRESSURE RATIO (P_t/P_{t_∞})

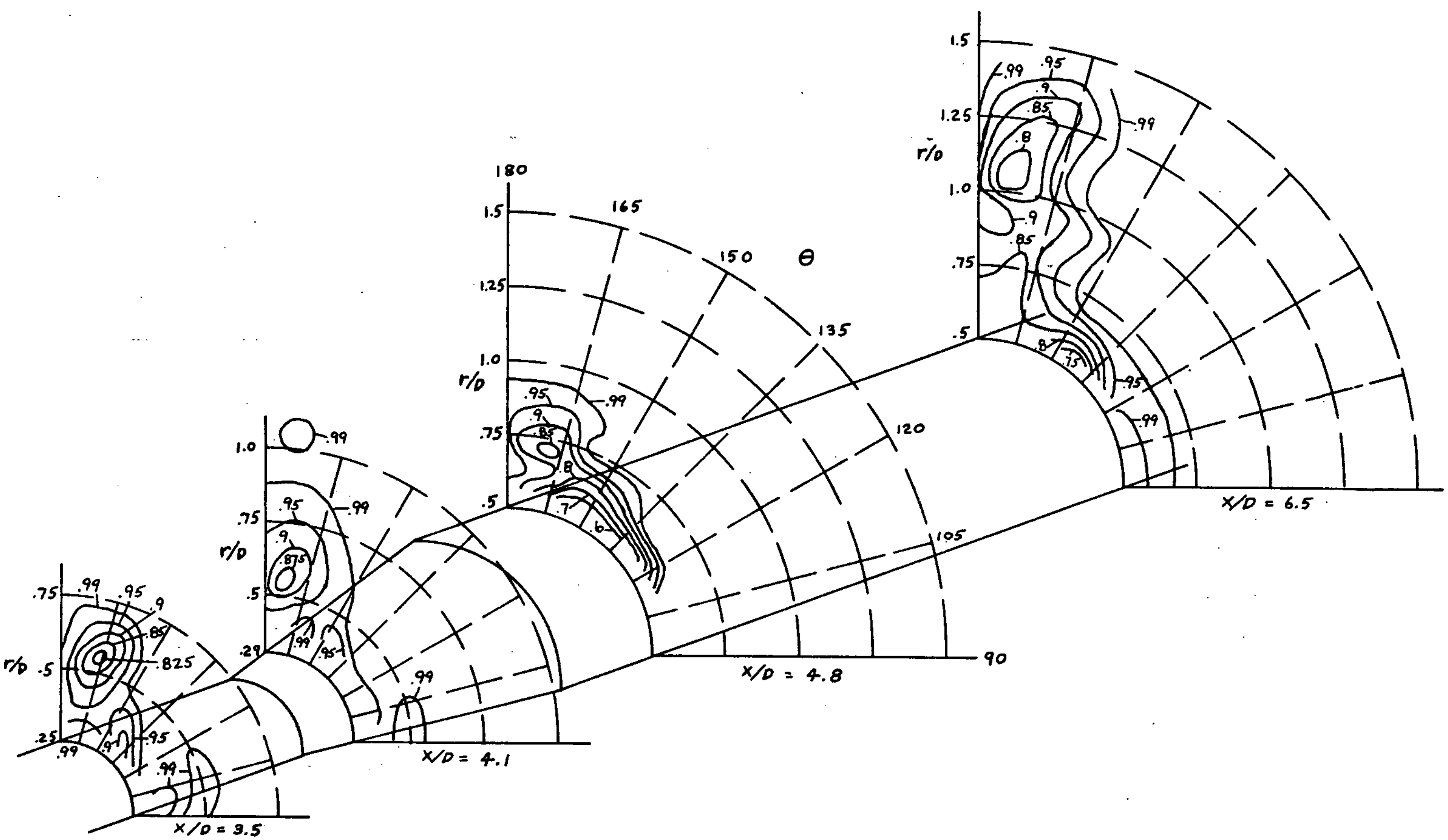

FIGURE 10 - CONSTANT LOCAL TOTAL PRESSURE RATIO CONTOURS (M_∞ =0.8, R_e=7.9X10^6ft^{-1})

(b) α_∞= 24.6°

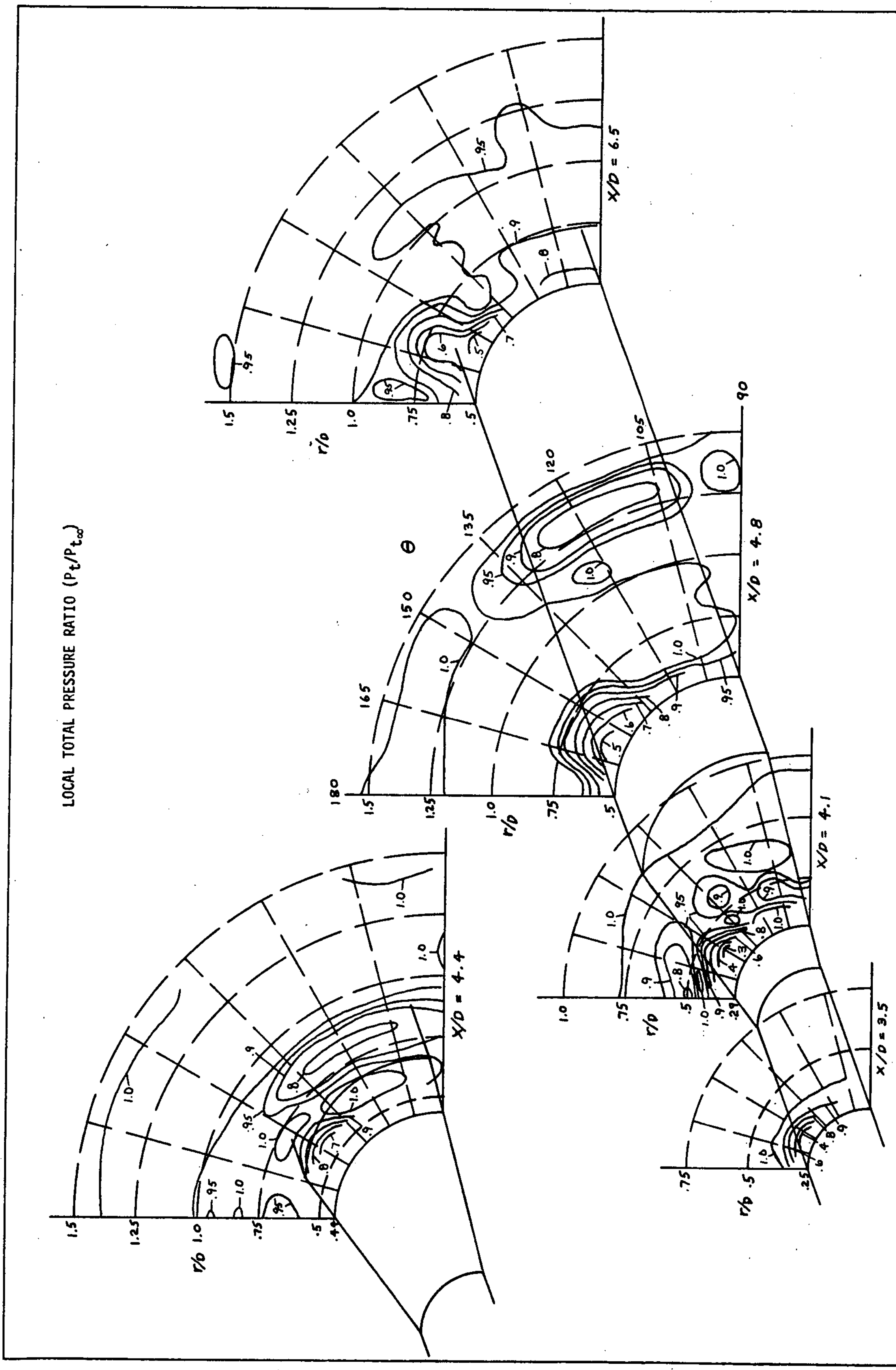

FIGURE 11 - CONSTANT LOCAL TOTAL PRESSURE RATIO CONTOURS (M_∞ =1.96, R_e=9.8X10^{6}ft^{-1})

(a) α_∞ = 10.0°

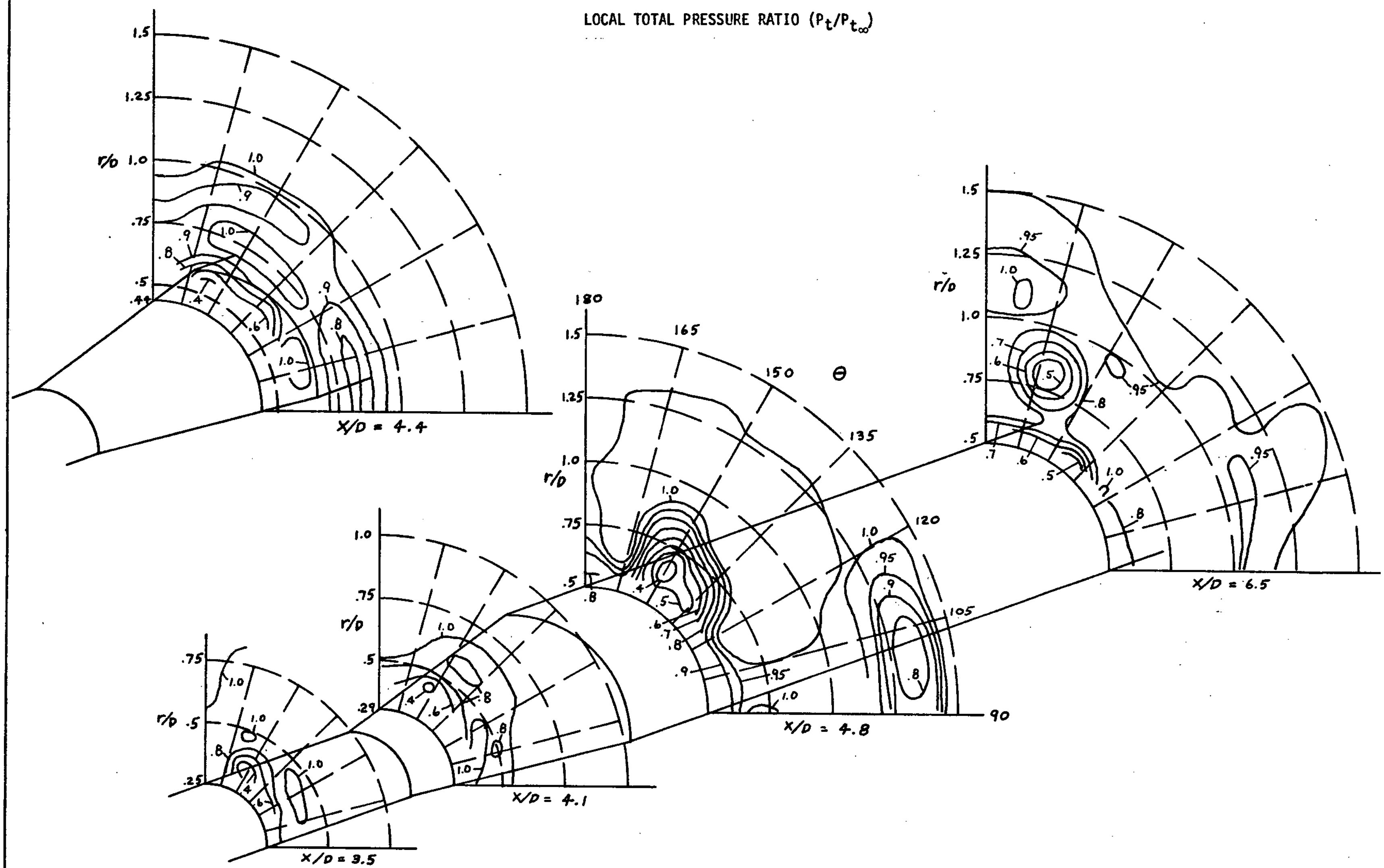

FIGURE 11 - CONSTANT LOCAL TOTAL PRESSURE RATIO CONTOURS (M_∞=1.96, R_e=9.8X10^{6}ft^{-1})

(b) α_∞= 14.5°

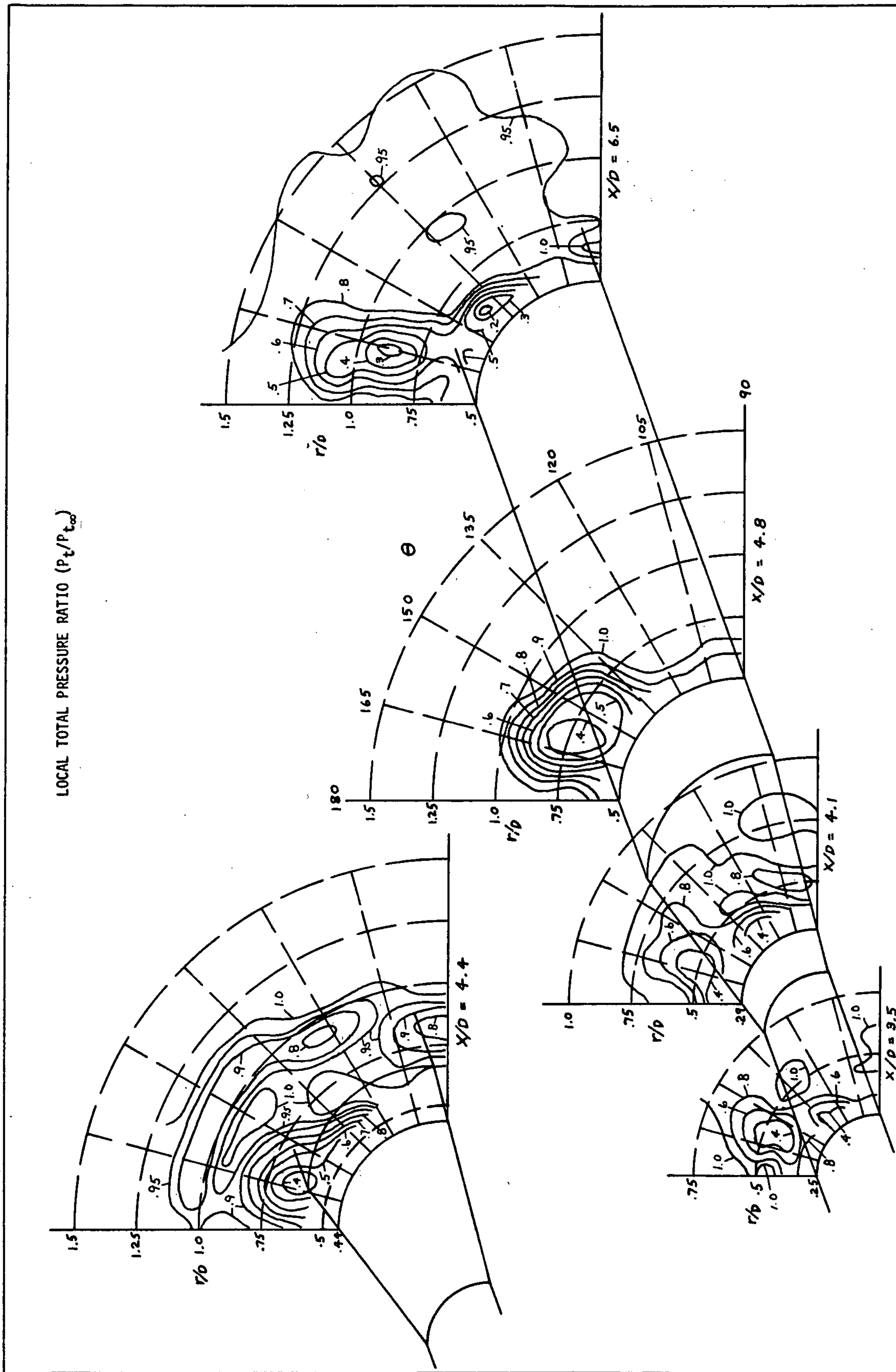

FIGURE 11 - CONSTANT LOCAL TOTAL PRESSURE RATIO CONTOURS (M_∞=1.96, R_e=9.8X10^{6}ft-1)

(c) α_∞ = 20.3°

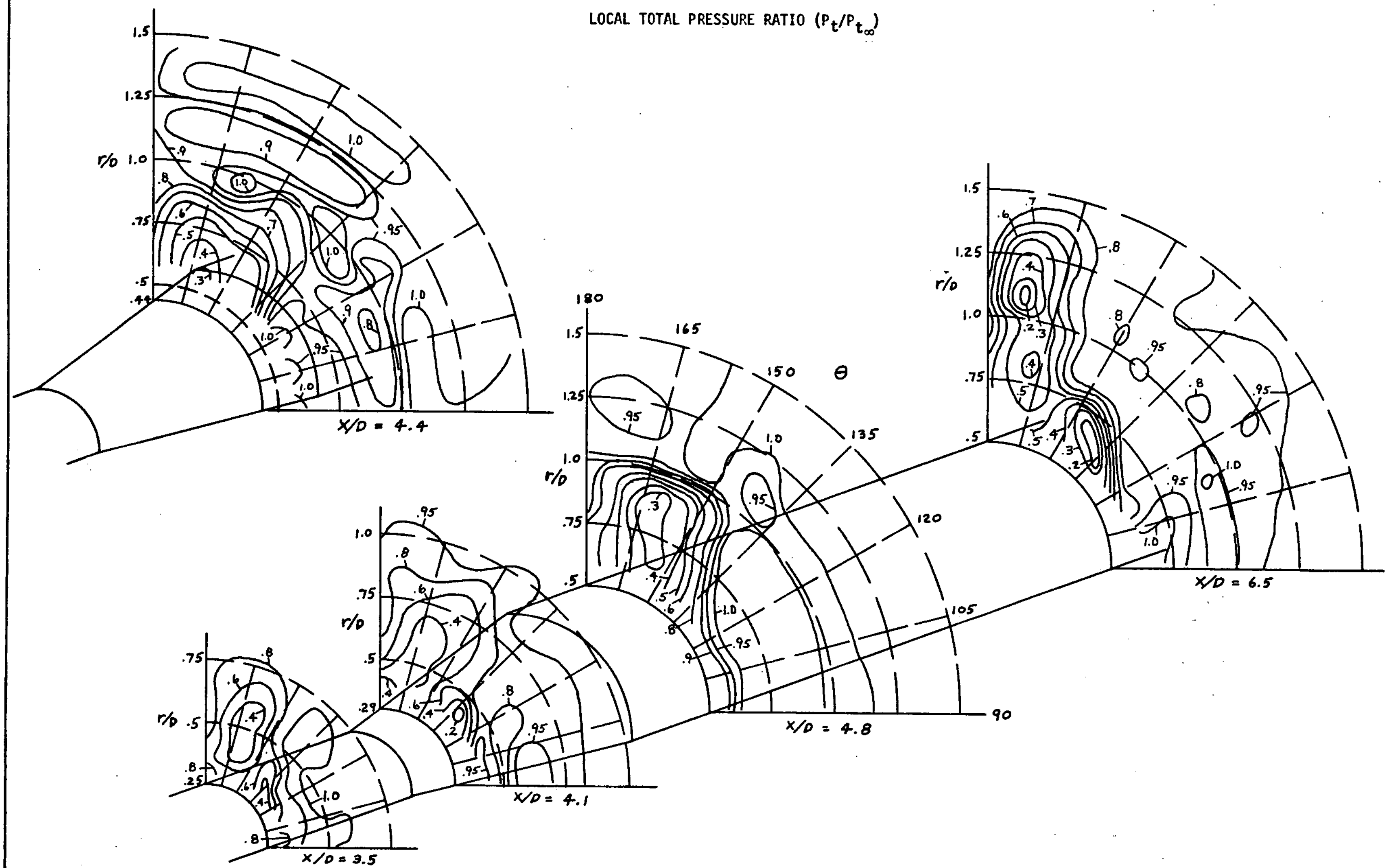

FIGURE 11 - CONSTANT LOCAL TOTAL PRESSURE RATIO CONTOURS (M_∞=1.96, R_e=9.8X10^{6}ft^{-1})

(d) α_∞ = 24.8°

LOCAL MACH NUMBER (M)

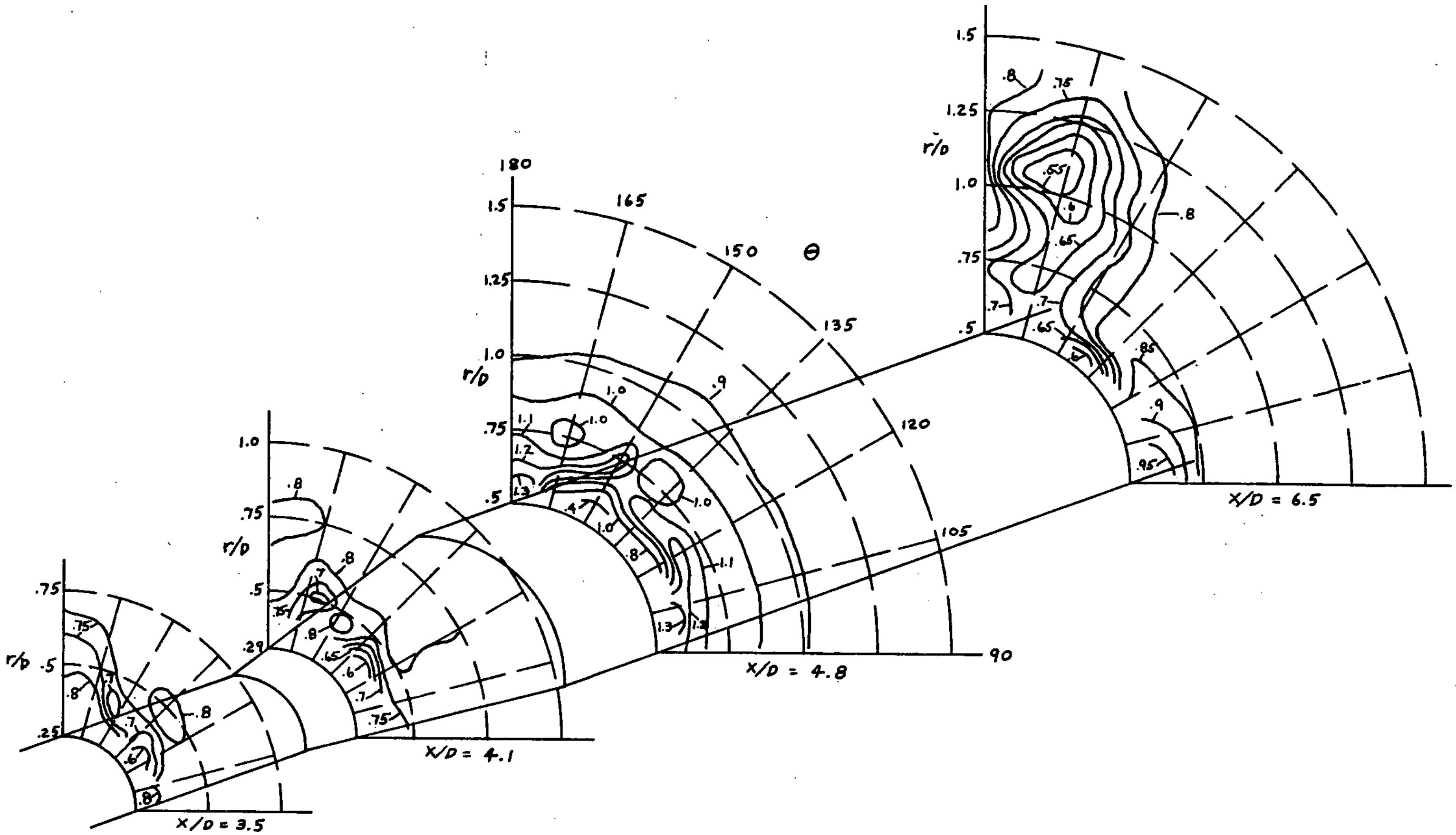

FIGURE 12 - CONSTANT LOCAL MACH NUMBER CONTOURS (M_∞ =0.8, R_e=4.4X10^{6}ft^{-1})

(a) α_∞= 20.1°

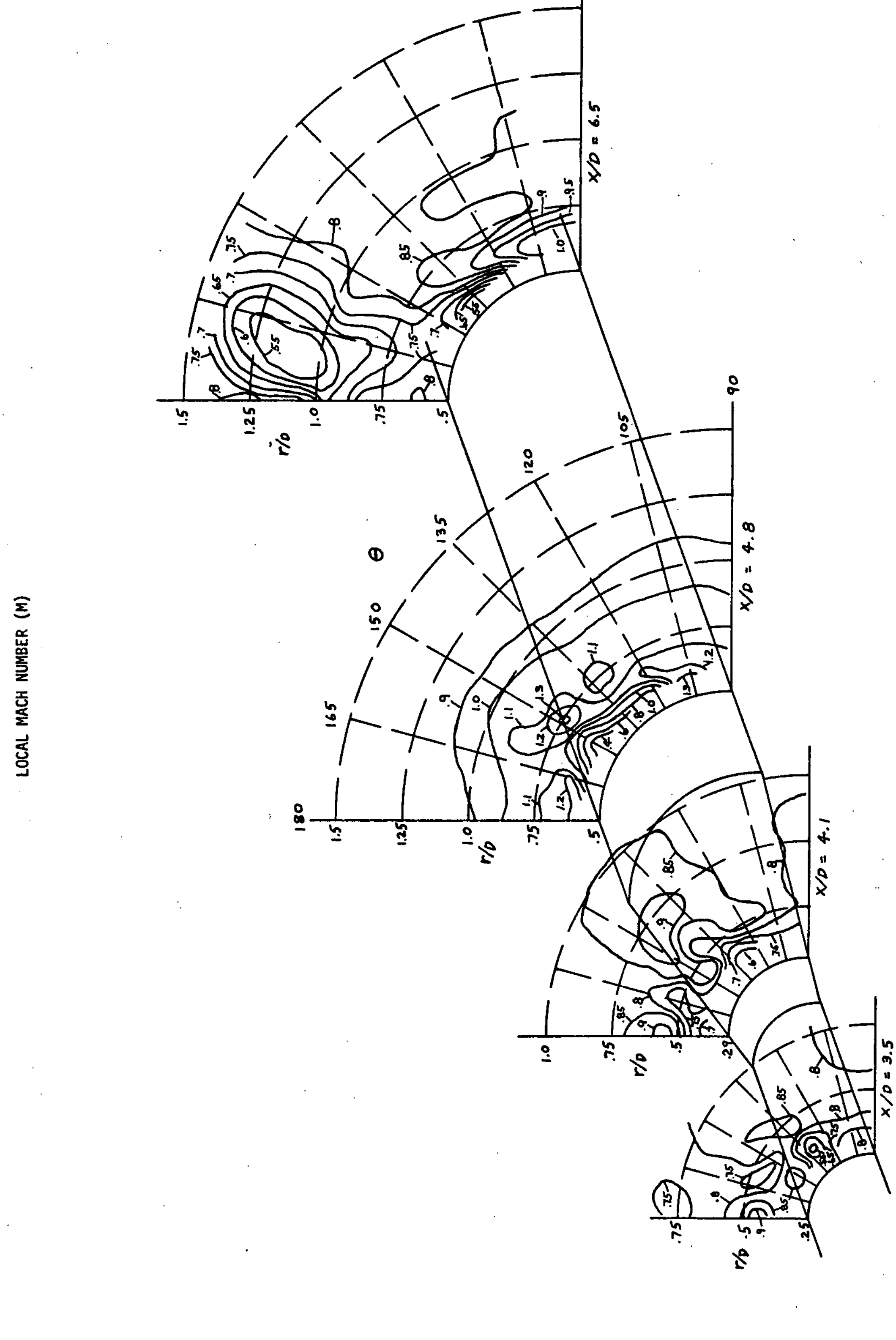

FIGURE 12 - CONSTANT LOCAL MACH NUMBER CONTOURS (M_∞ = 0.8, R_e=4.4X10^6ft^{-1})

(b) α_∞ = 24.6°

LOCAL MACH NUMBER (M)

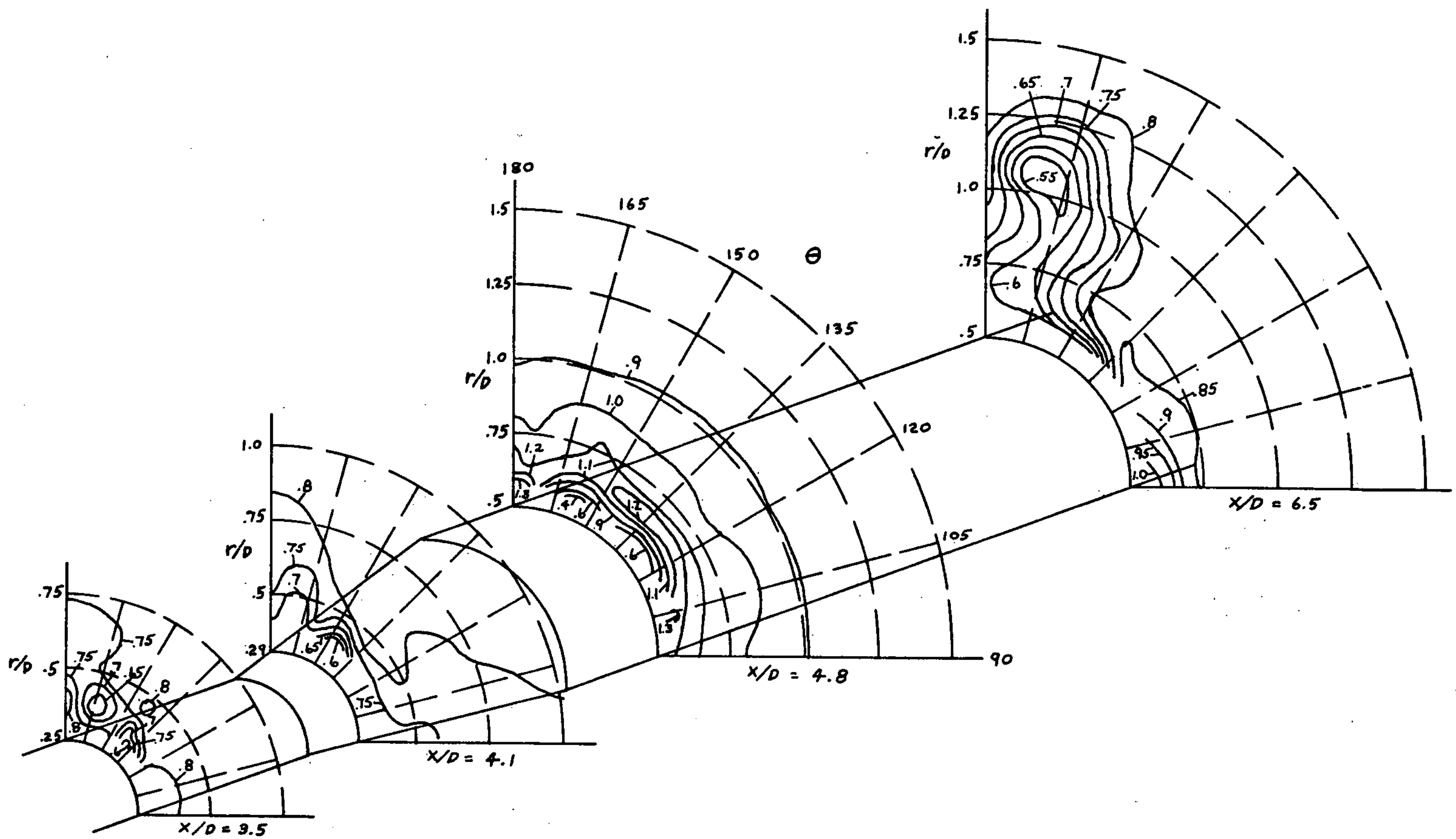

FIGURE 13 - CONSTANT LOCAL MACH NUMBER CONTOURS ($M_\infty = 0.8$, $R_e = 7.9 \times 10^6 ft^{-1}$)

(a) $\alpha_\infty = 20.1°$

LOCAL MACH NUMBER (M)

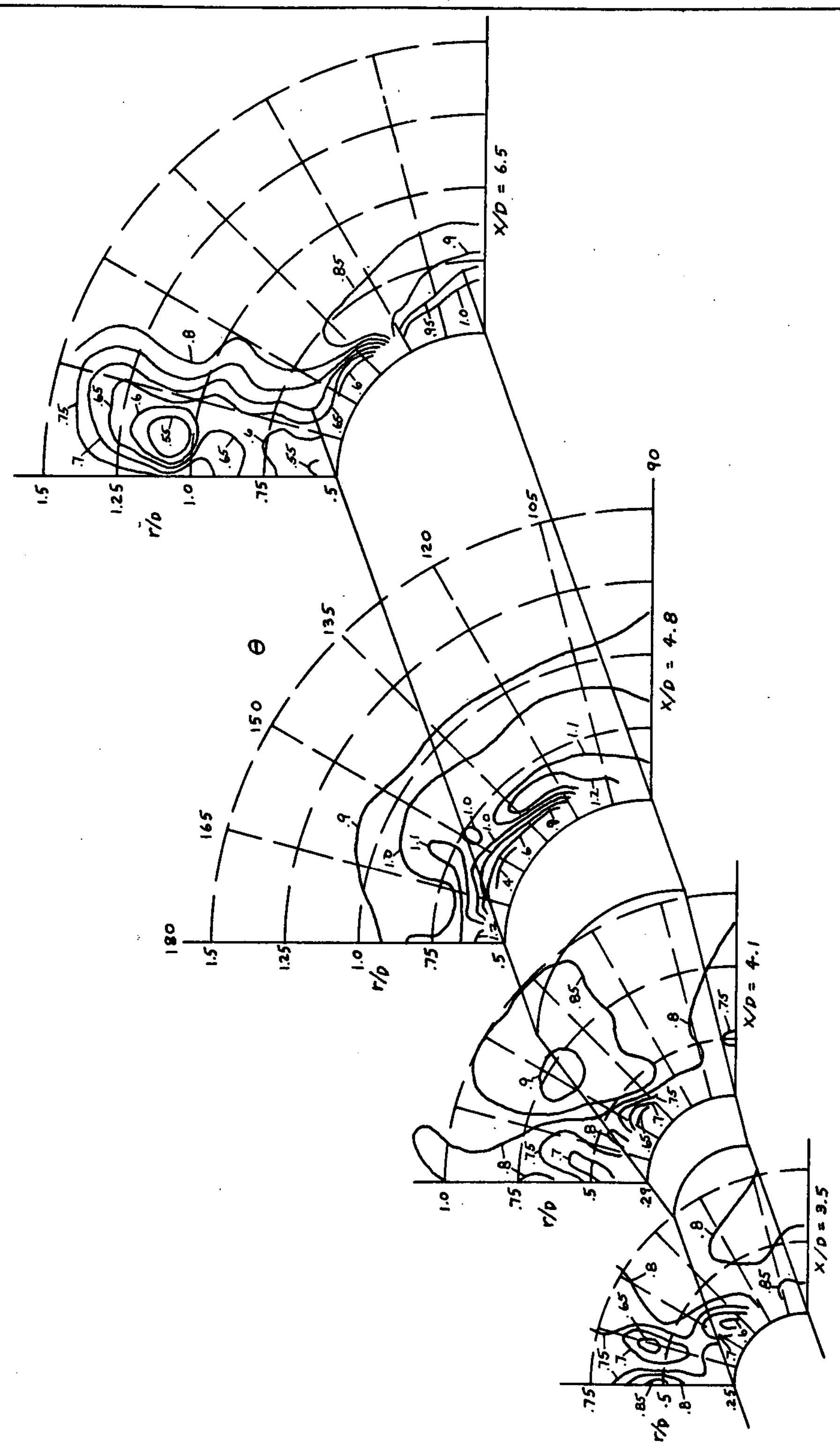

FIGURE 13 - CONSTANT LOCAL MACH NUMBER CONTOURS (M_∞=0.8, R_e=7.9X10^{6}ft^{-1})

(b) α_∞= 24.6°

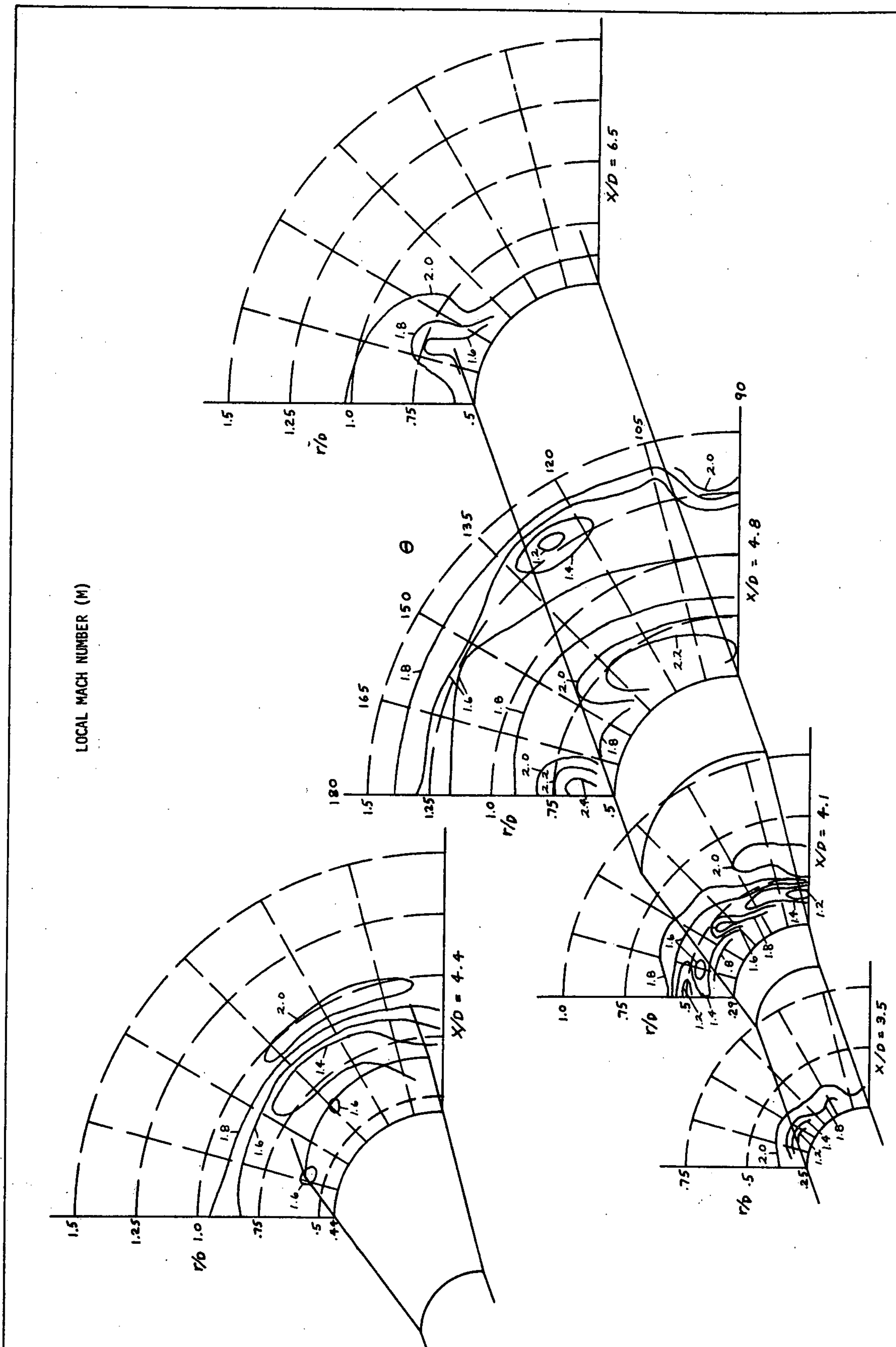

FIGURE 14 - CONSTANT LOCAL MACH NUMBER CONTOURS (M_∞=1.96, R_e=9.8X10^{6}ft^{-1})

(a) α_∞ = 10.0°

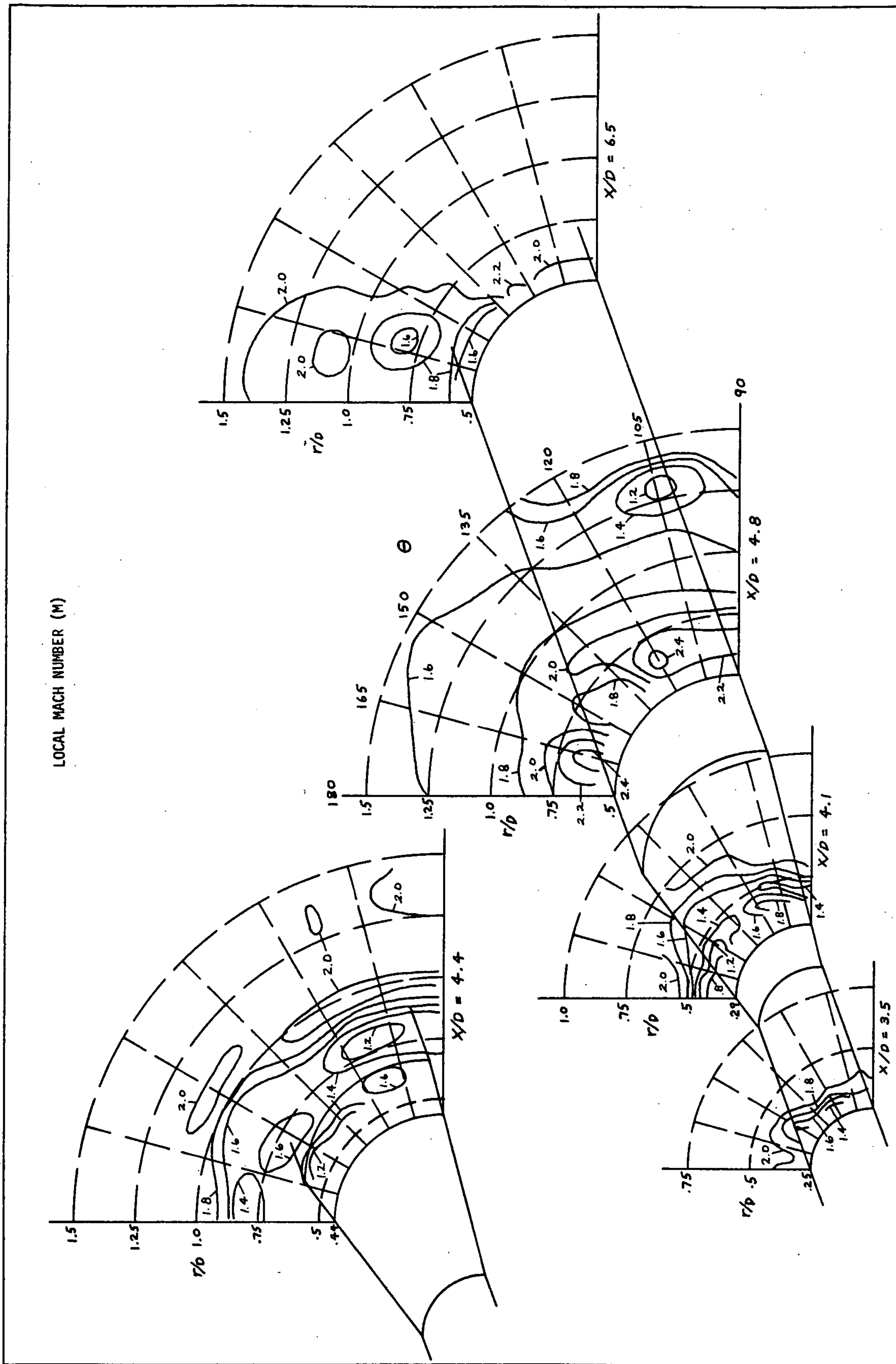

FIGURE 14 - CONSTANT LOCAL MACH NUMBER CONTOURS (M_∞=1.96, R_e=9.8X10^6ft^{-1})

(b) α_∞ = 14.5°

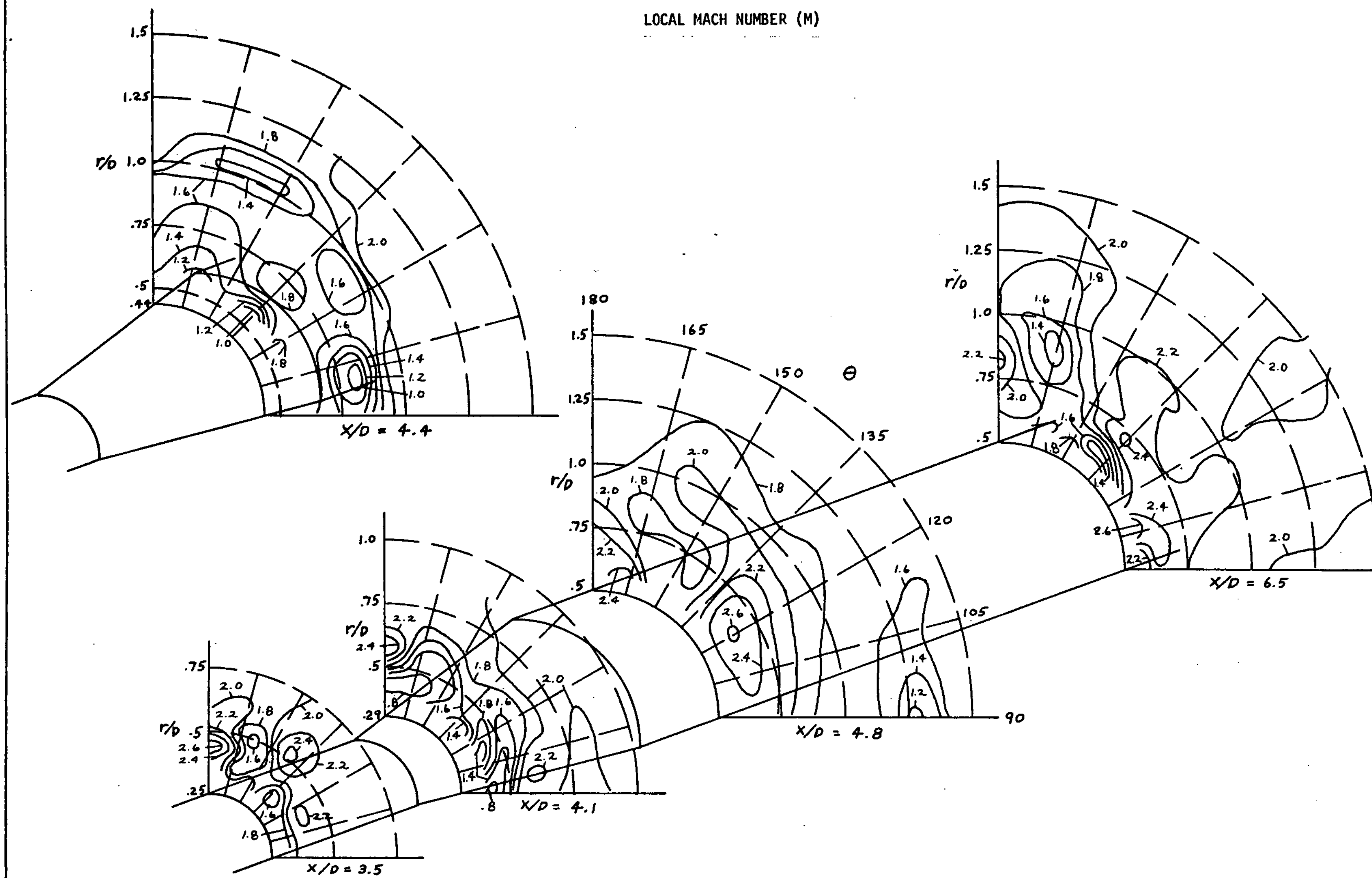

FIGURE 14 - CONSTANT LOCAL MACH NUMBER CONTOURS (M_∞=1.96, R_e=9.8X10^{6}ft^{-1})

(c) α_∞ = 20.3°

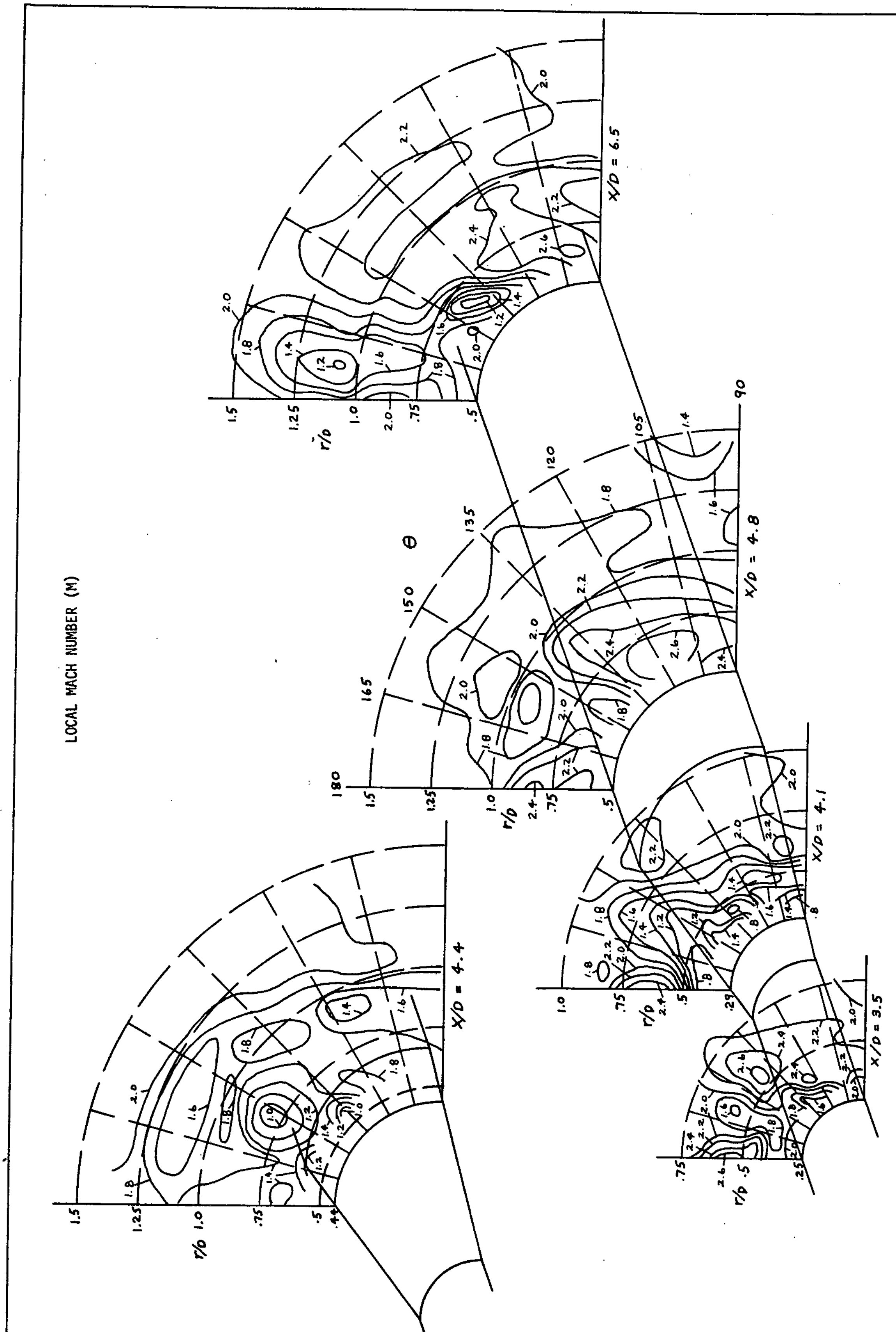

FIGURE 14 - CONSTANT LOCAL MACH NUMBER CONTOURS (M_∞=1.96, R_E=9.8X10^6ft^{-1})

(d) α_∞ = 24.8°

LOCAL PRESSURE COEFFICIENT (C_p)

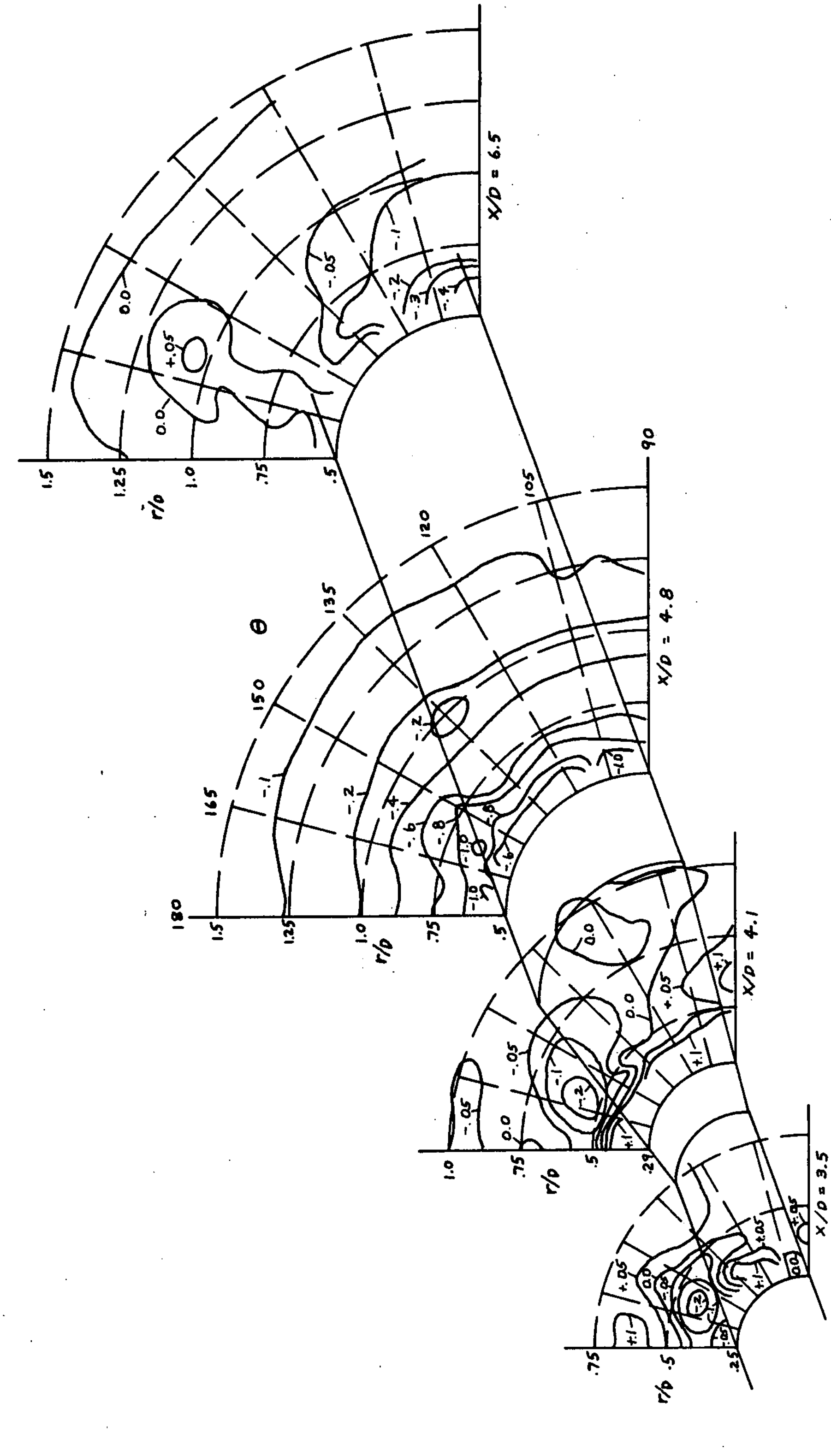

FIGURE 15 - CONSTANT LOCAL PRESSURE COEFFICIENT CONTOURS (M_∞=0.8, R_e=4.4X10^6ft^{-1})

(a) α_∞ = 20.1°

LOCAL PRESSURE COEFFICIENT (C_p)

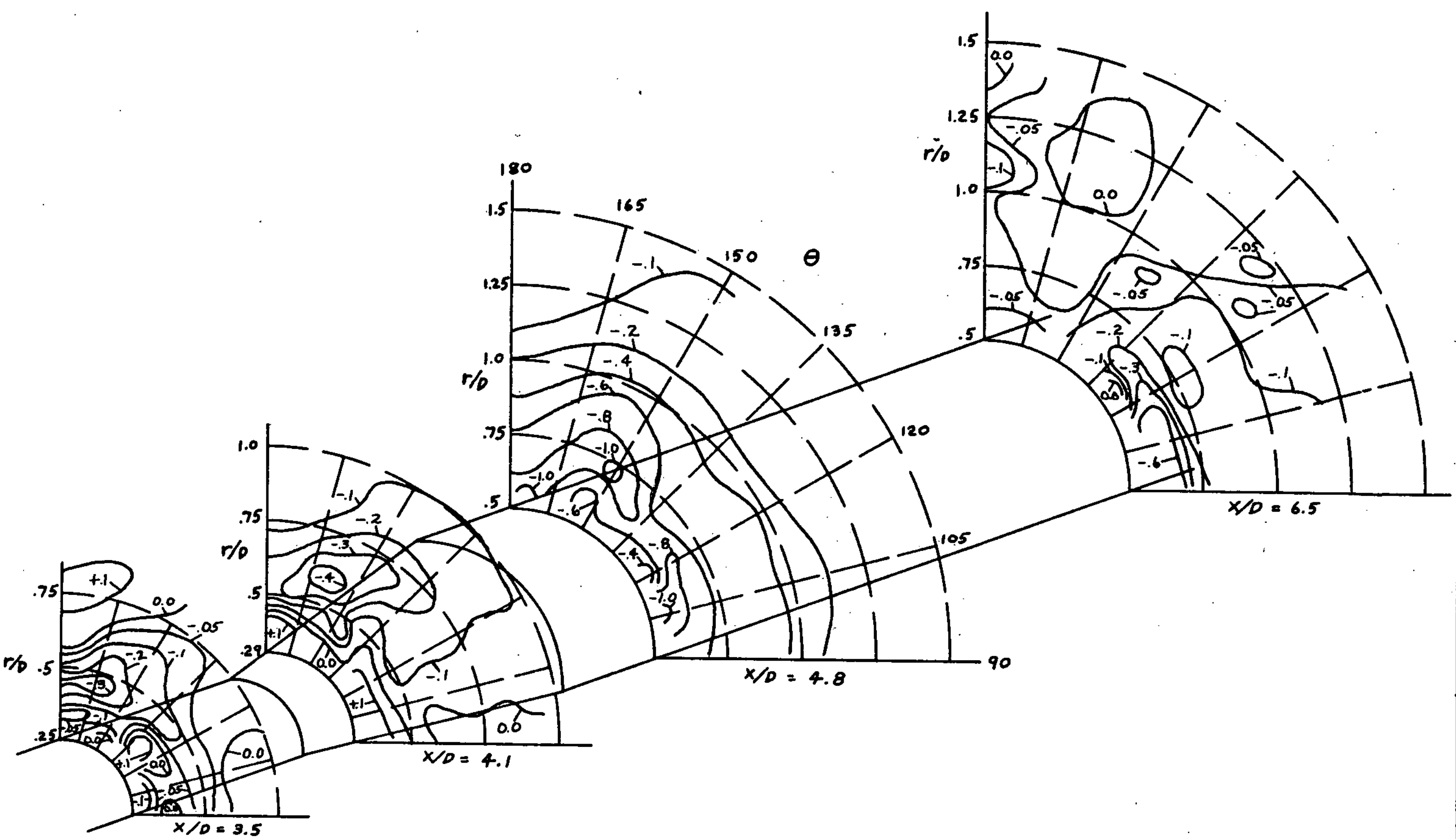

FIGURE 15 - CONSTANT LOCAL PRESSURE COEFFICIENT CONTOURS (M_∞=0.8, R_e=4.4X10^{6}ft^{-1})

(b) α_∞= 24.6°

LOCAL PRESSURE COEFFICIENT (C_p)

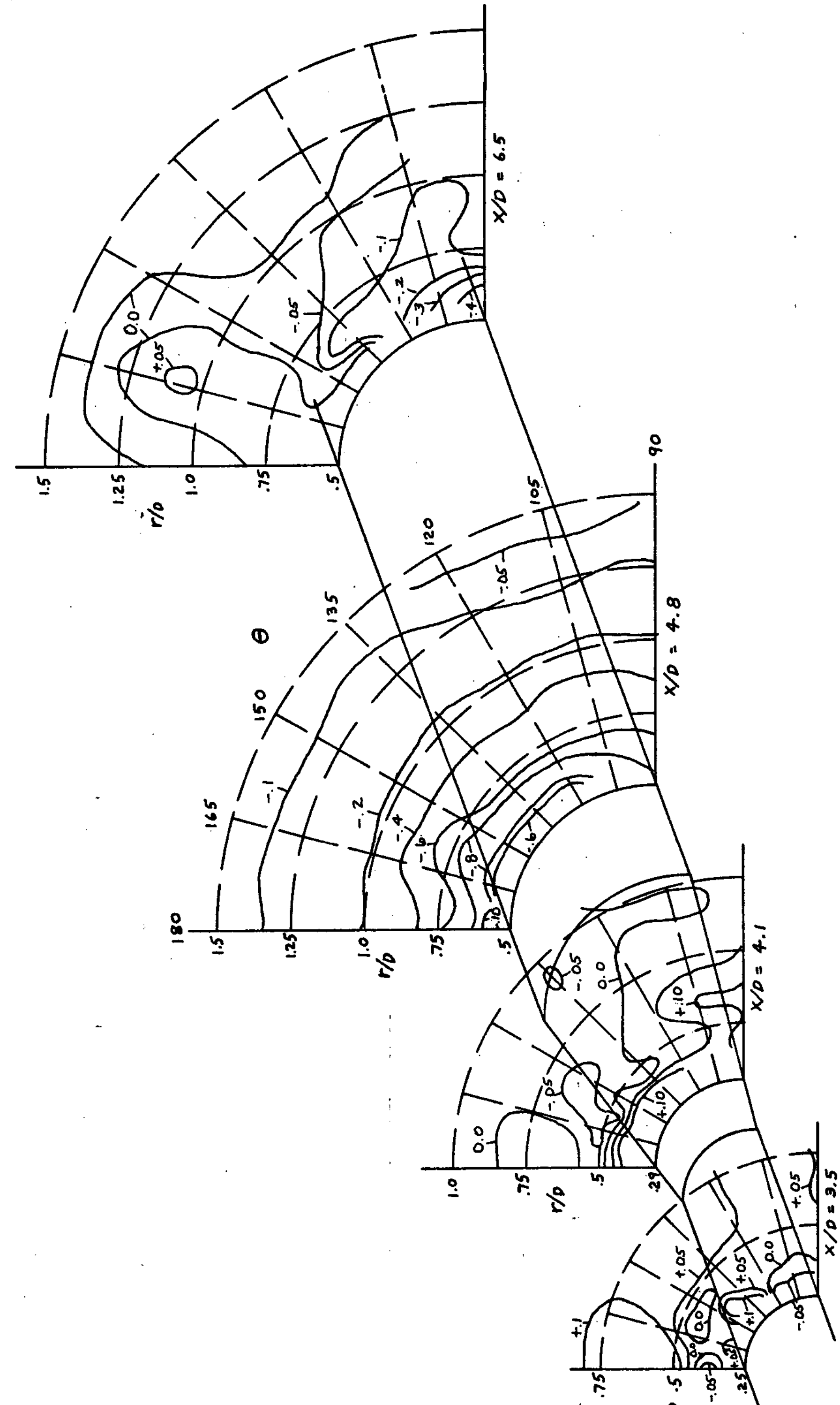

FIGURE 16 - CONSTANT LOCAL PRESSURE COEFFICIENT CONTOURS (M_∞=0.8, R_e=7.9X10^6ft^{-1})

(a) α_∞ = 20.1°

LOCAL PRESSURE COEFFICIENT (C_p)

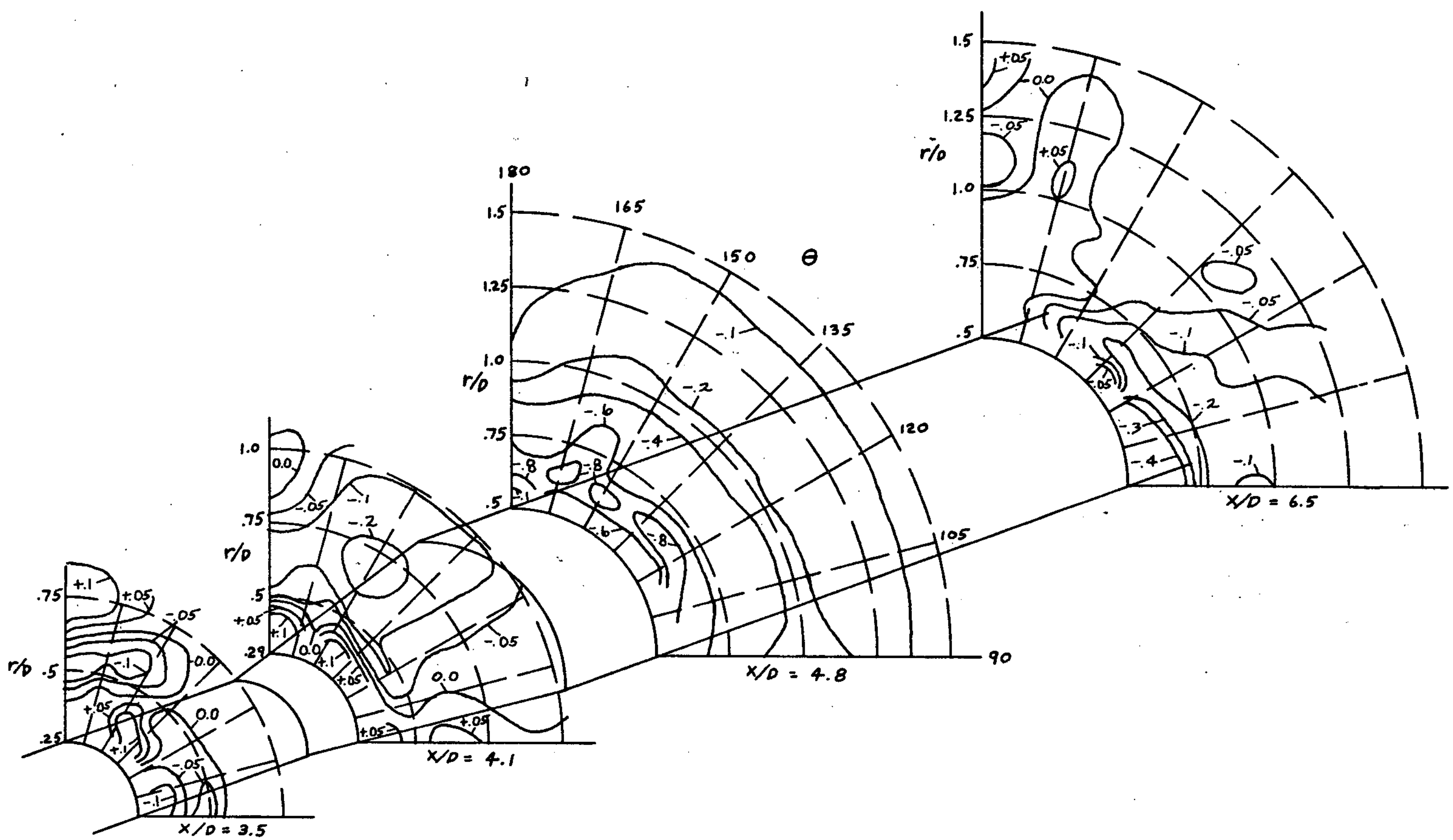

FIGURE 16 - CONSTANT LOCAL PRESSURE COEFFICIENT CONTOURS (M_∞ =0.8, R_e=7.9X10^{6}ft^{-1})

(b) α_∞ = 24.6°

LOCAL PRESSURE COEFFICIENT (C_p)

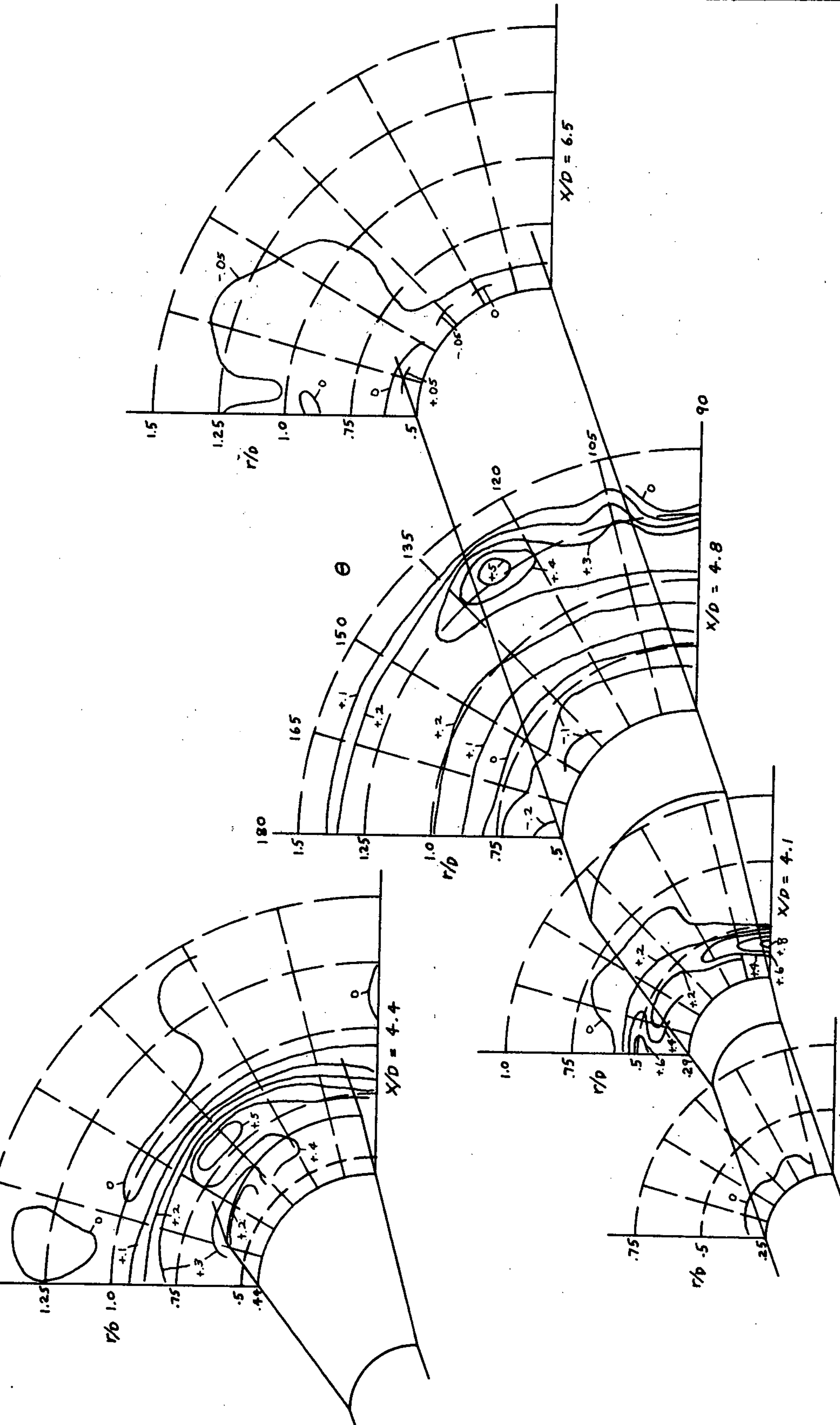

FIGURE 17 - CONSTANT LOCAL PRESSURE COEFFICIENT CONTOURS (M_∞=1.96, R_e=9.8X10^6 ft^{-1})

(a) α_∞ = 10.0°

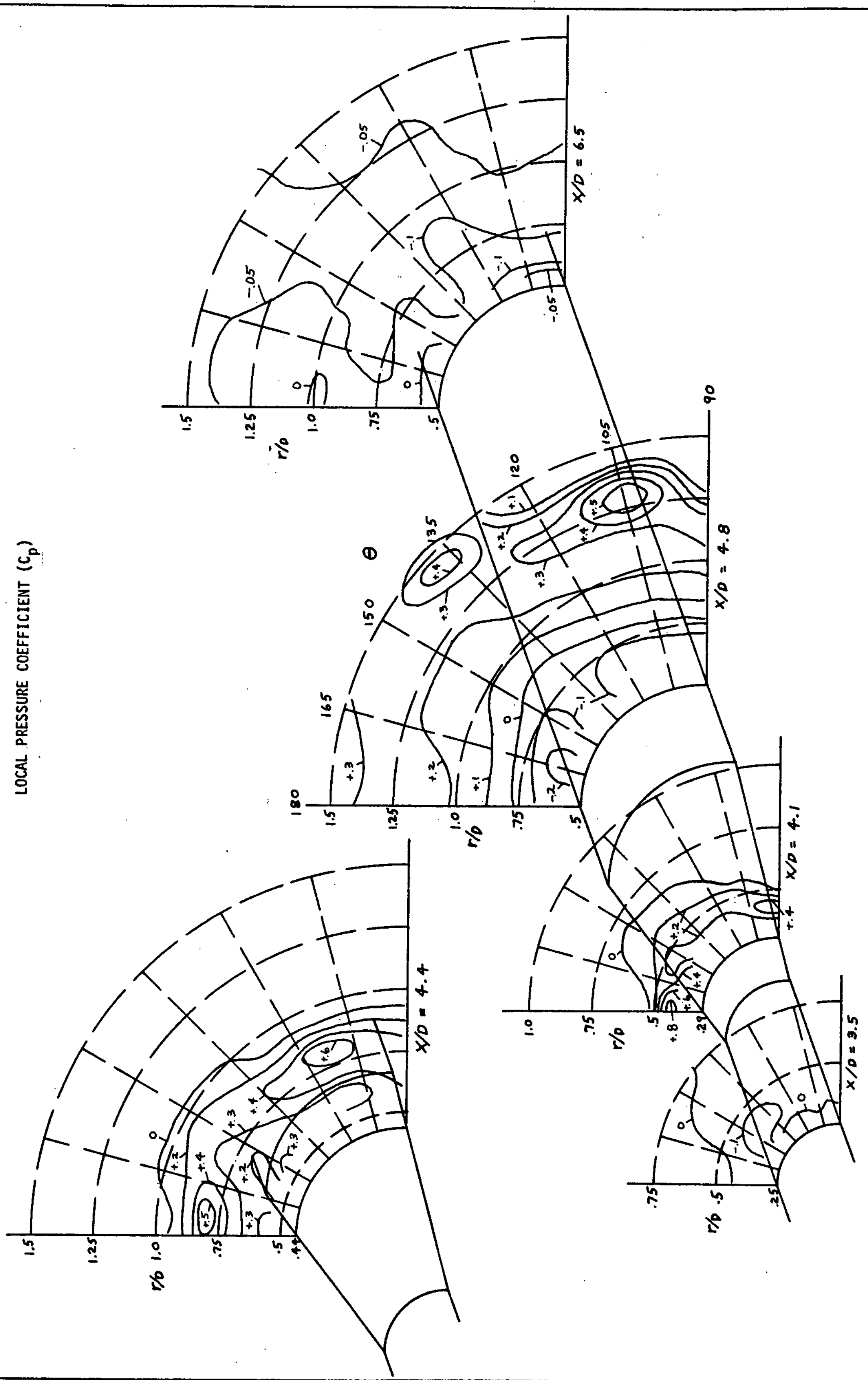

FIGURE 17 - CONSTANT LOCAL PRESSURE COEFFICIENT CONTOURS (M_∞=1.96, R_e=9.8X10^6ft^{-1})

(b) α_∞ = 14.5°

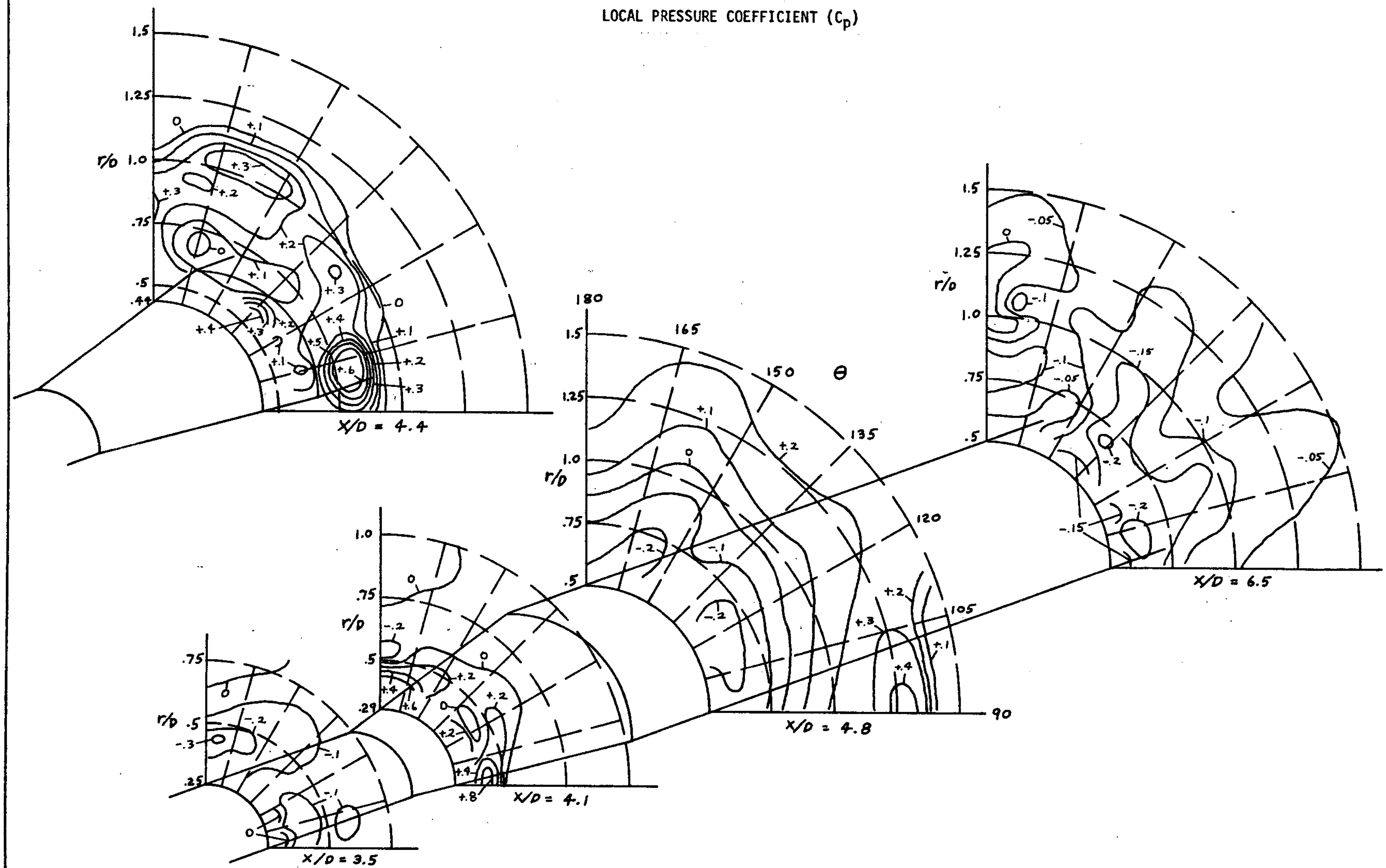

FIGURE 17 - CONSTANT LOCAL PRESSURE COEFFICIENT CONTOURS ($M_\infty = 1.96$, $R_e = 9.8 \times 10^6 ft^{-1}$)

(c) $\alpha_\infty = 20.3°$

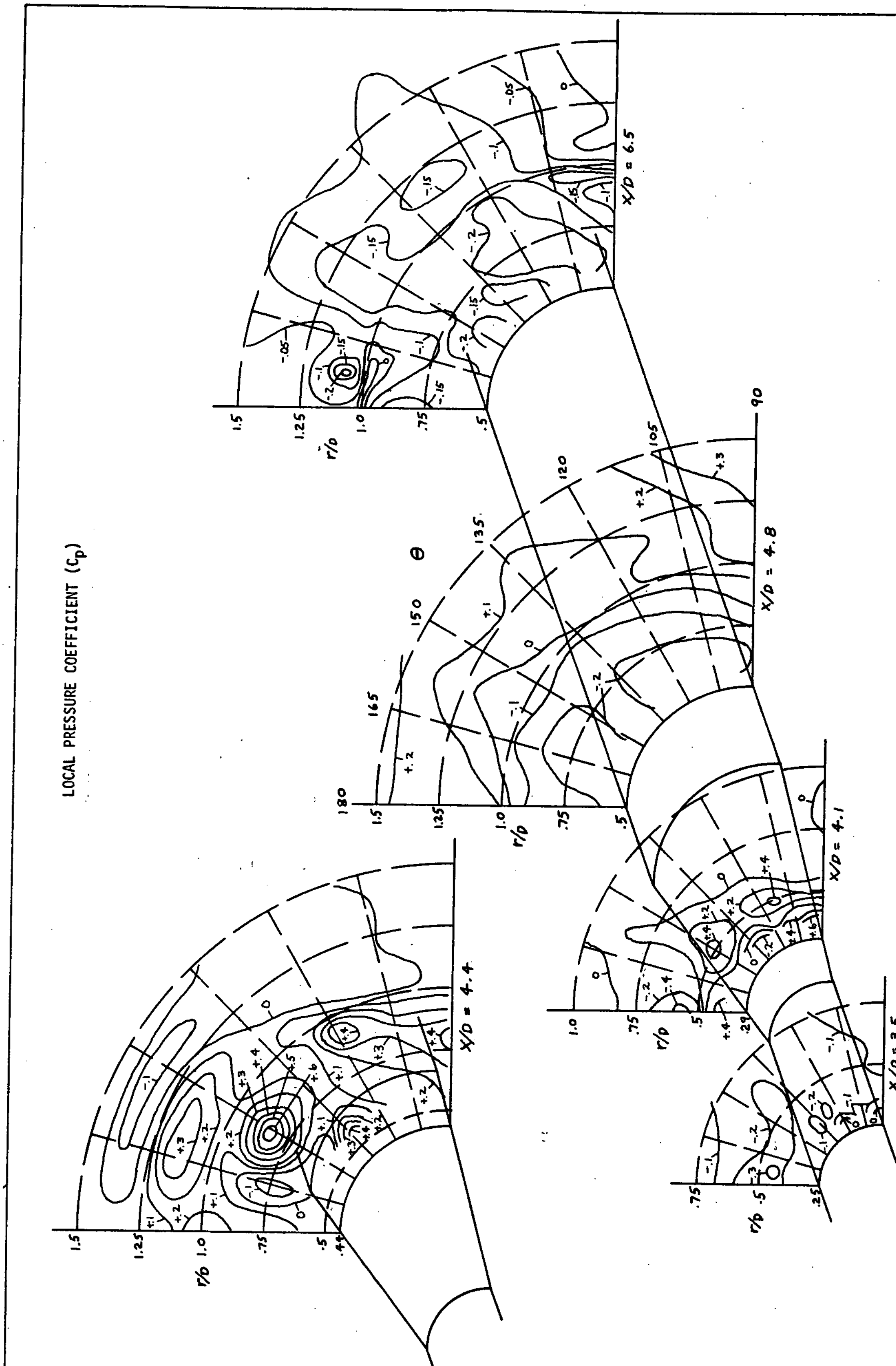

FIGURE 17 - CONSTANT LOCAL PRESSURE COEFFICIENT CONTOURS (M_∞=1.96, R_e=9.8X106ft^{-1})

(d) α_c = 24.8°

U1108/SC4020
0022 0000

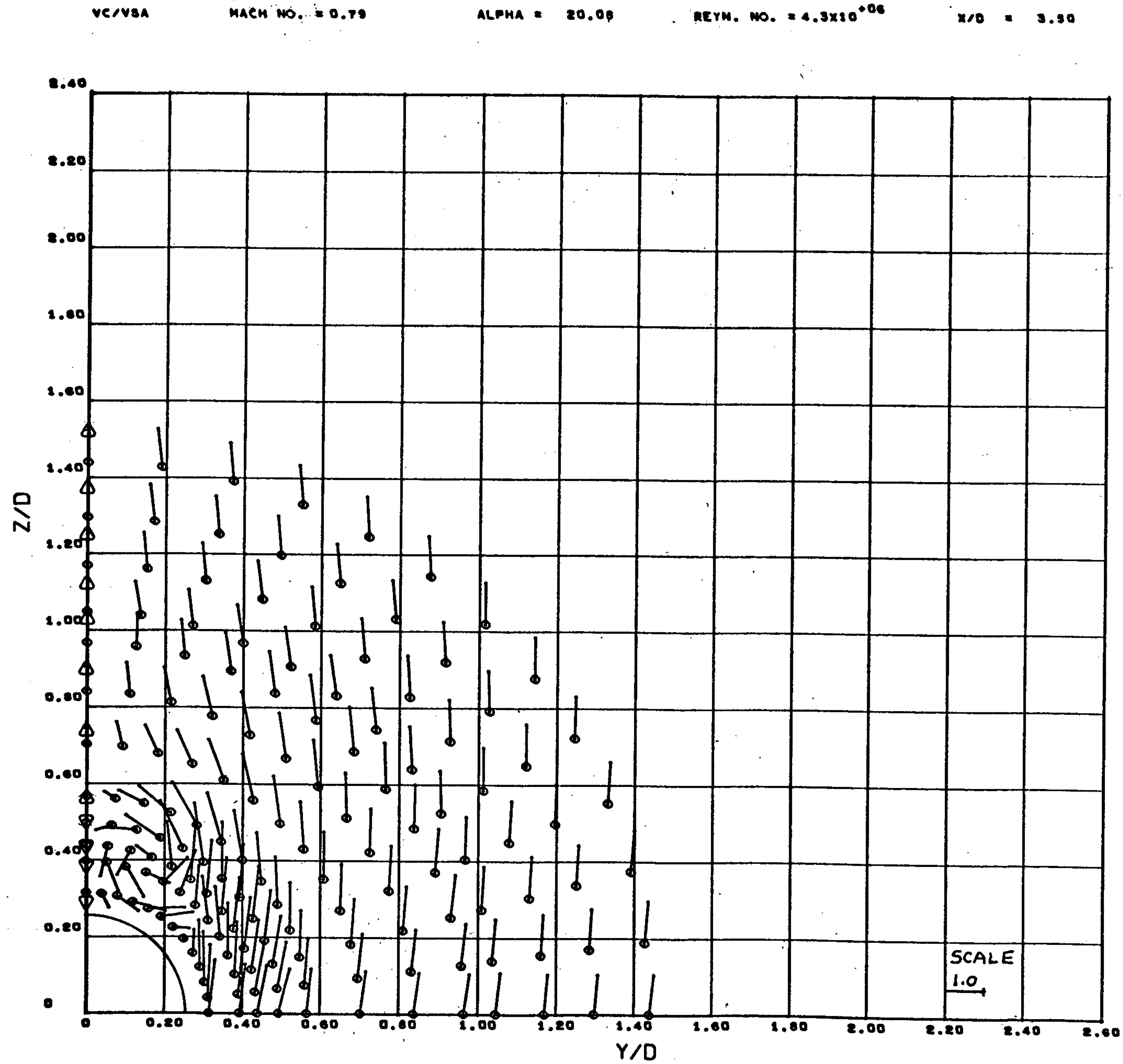

Figure 18a - Local Crossflow Velocity Vectors ~ $\frac{V_c}{V_\infty \sin\alpha}$

U1108/SC4020
0018 0000

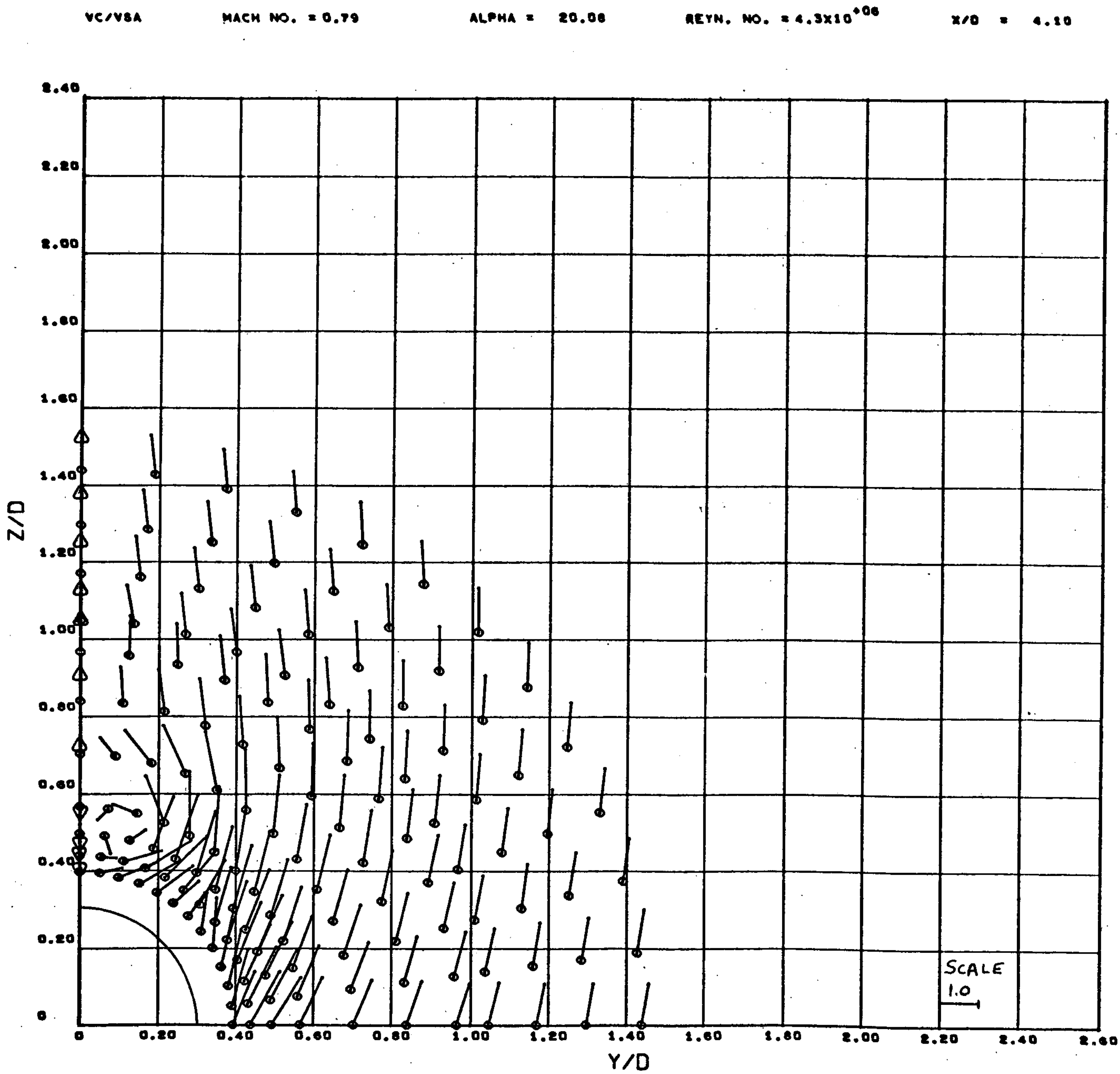

Figure 18a (cont'd) - Local Crossflow Velocity Vectors ~ $\frac{V_c}{V_\infty \sin\alpha}$

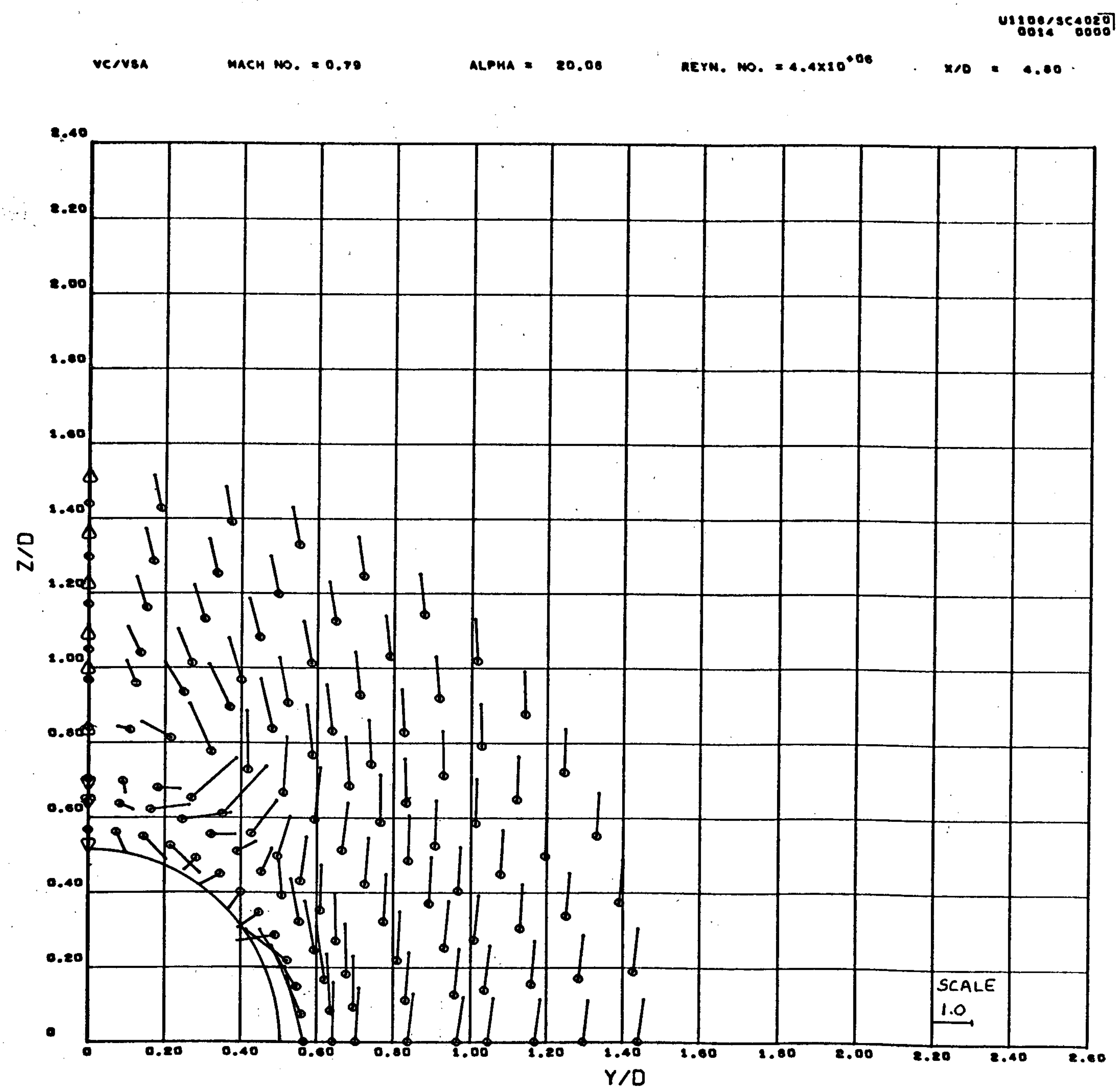

Figure 18a (cont'd) - Local Crossflow Velocity Vectors ~ $\frac{V_c}{V_\infty \sin\alpha}$

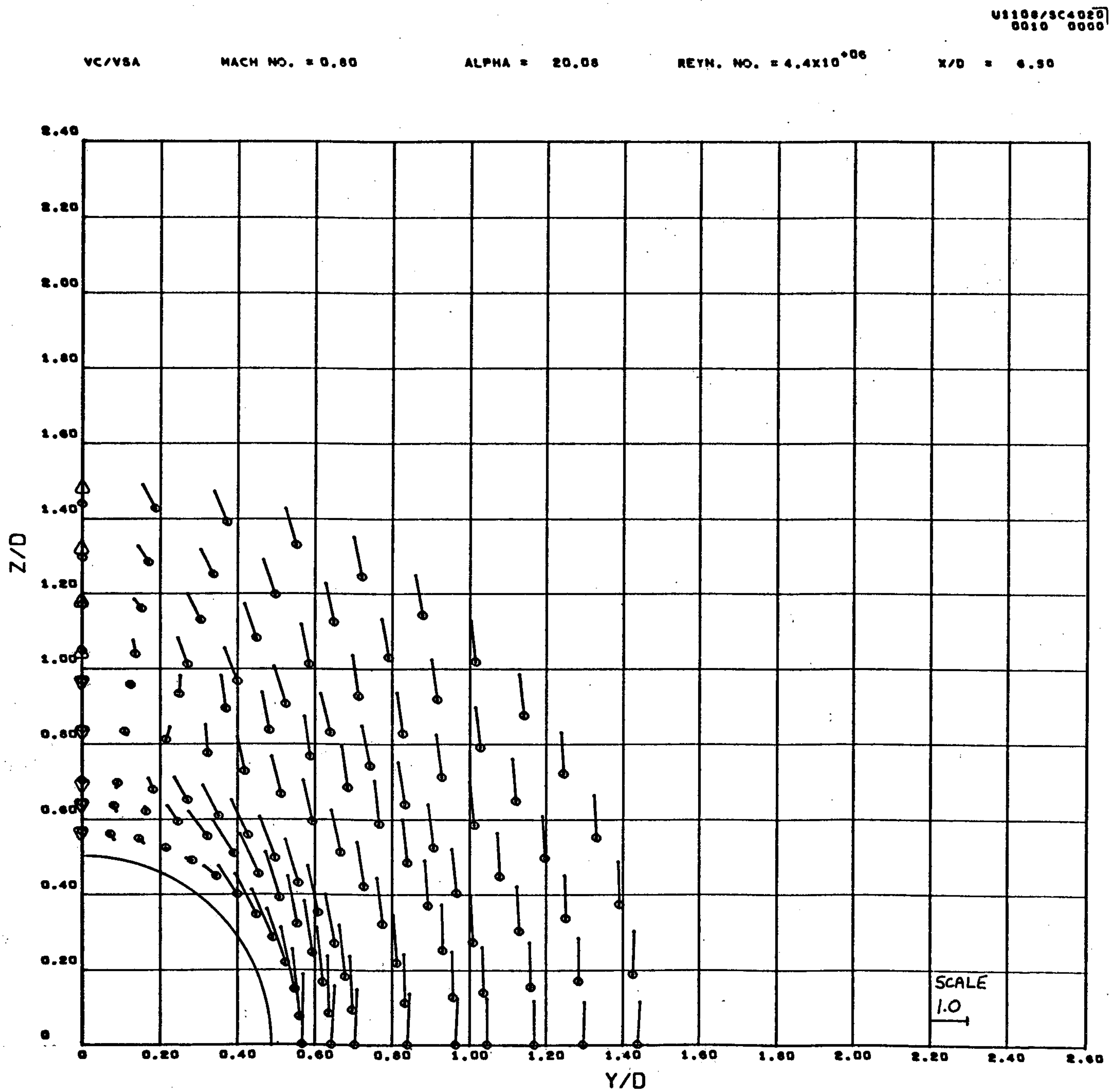

Figure 18a (cont'd) - Local Crossflow Velocity Vectors ~ $\frac{V_c}{V_\infty \sin\alpha}$

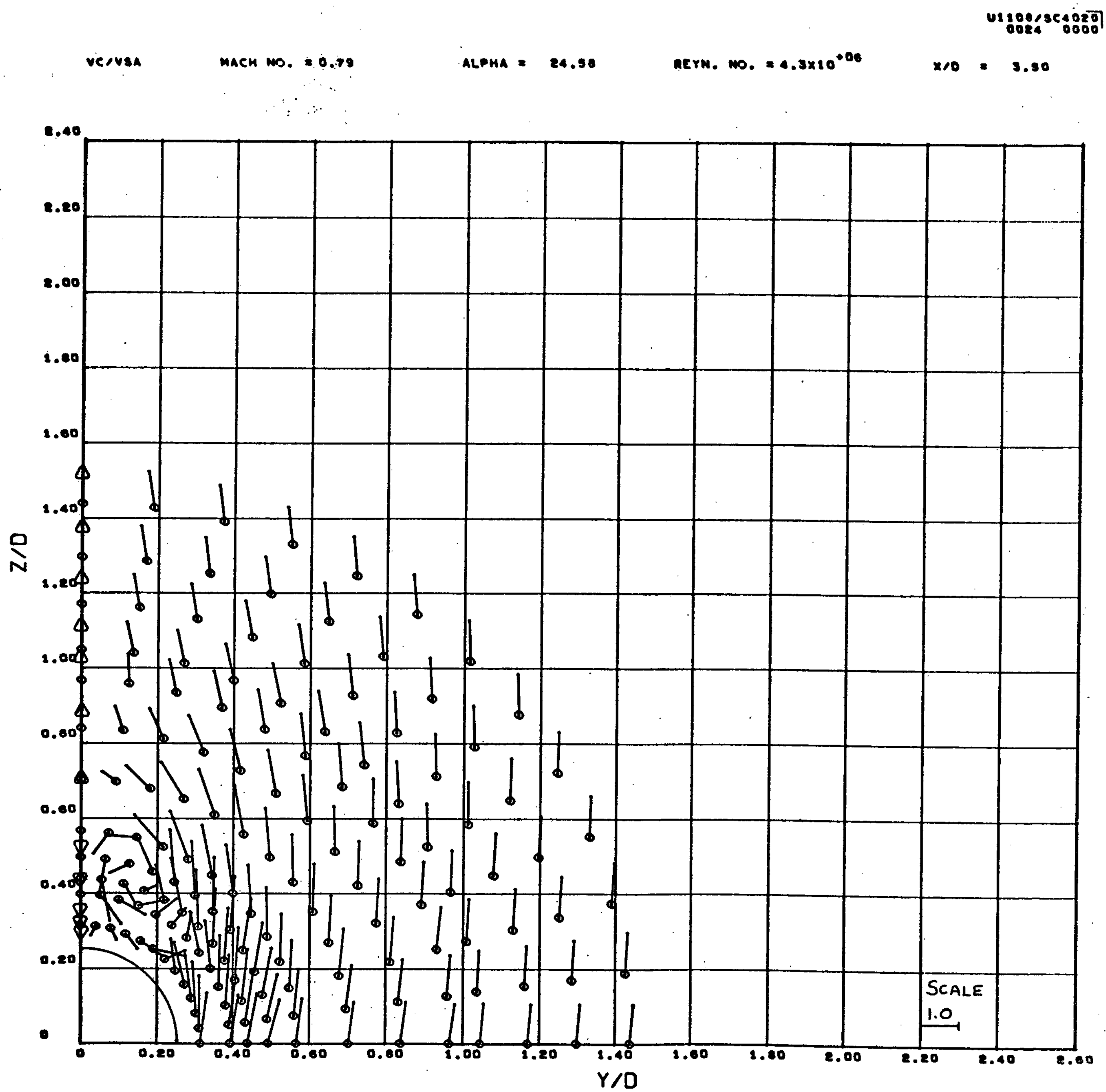

Figure 18b - Local Crossflow Velocity Vectors ~ $\frac{V_c}{V_\infty \sin\alpha}$

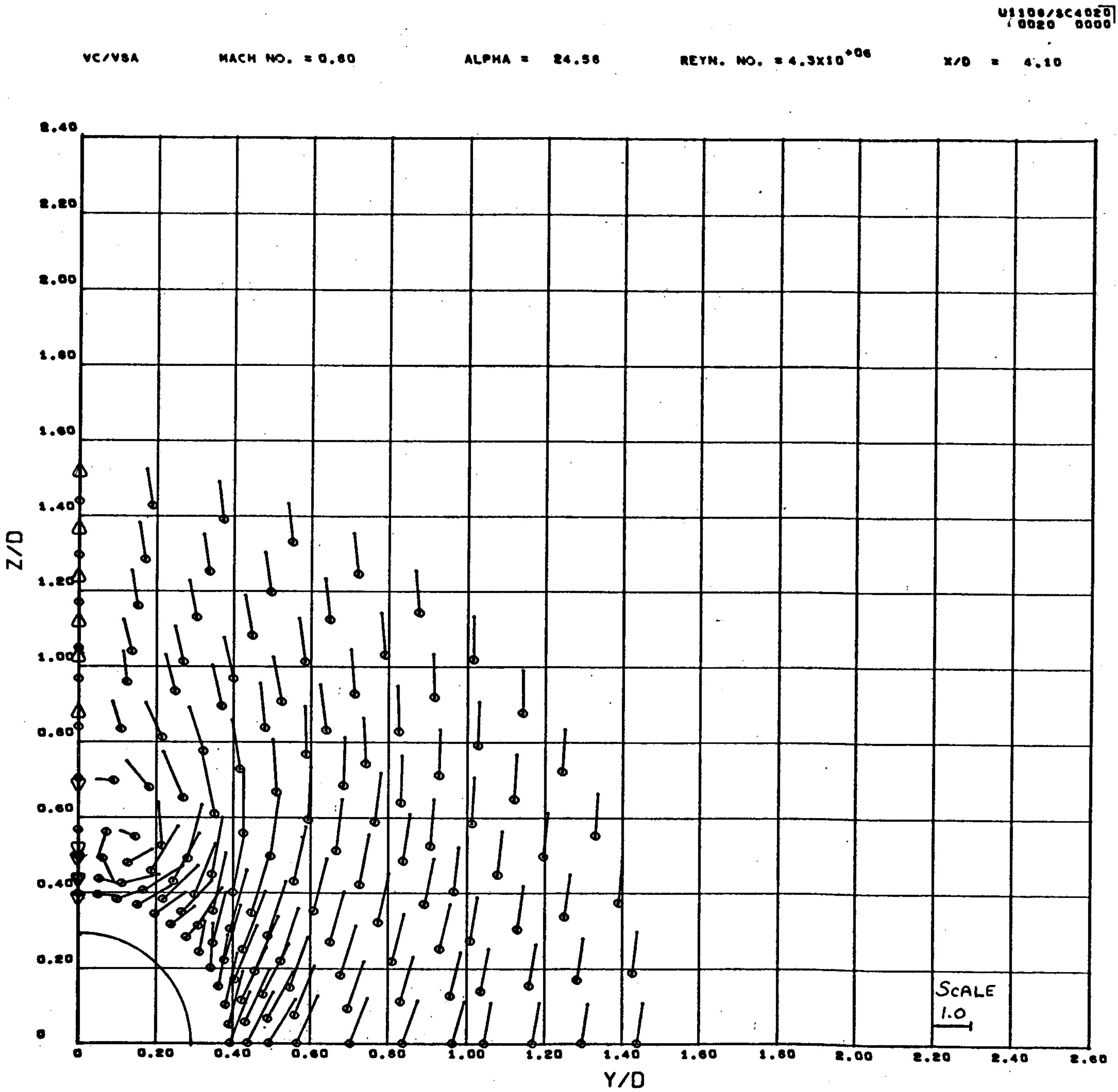

Figure 18b (cont'd) - Local Crossflow Velocity Vectors ~ $\frac{V_c}{V_\infty \sin\alpha}$

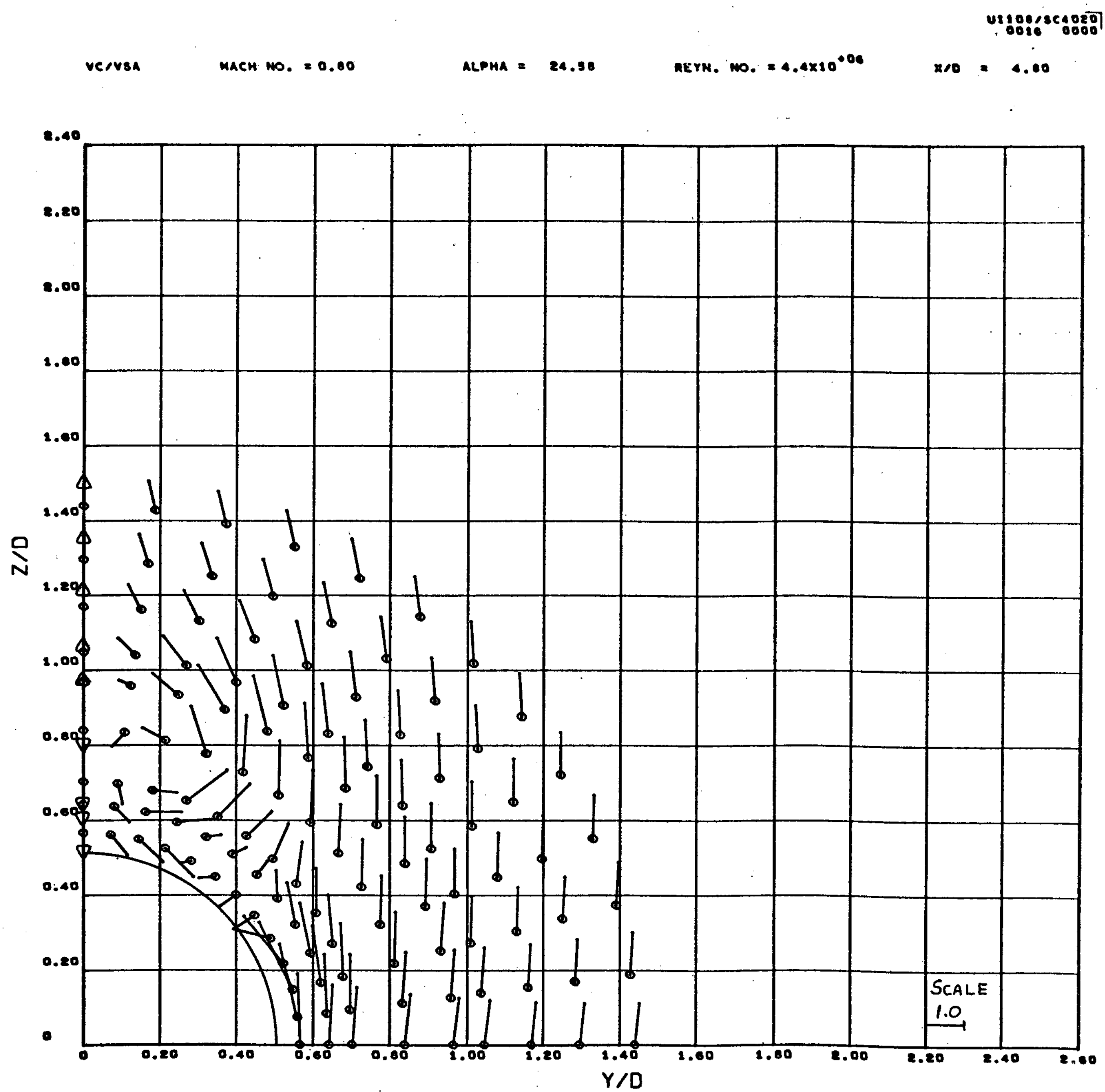

Figure 18b (cont'd) - Local Crossflow Velocity Vectors $\sim \frac{V_c}{V_\infty \sin\alpha}$

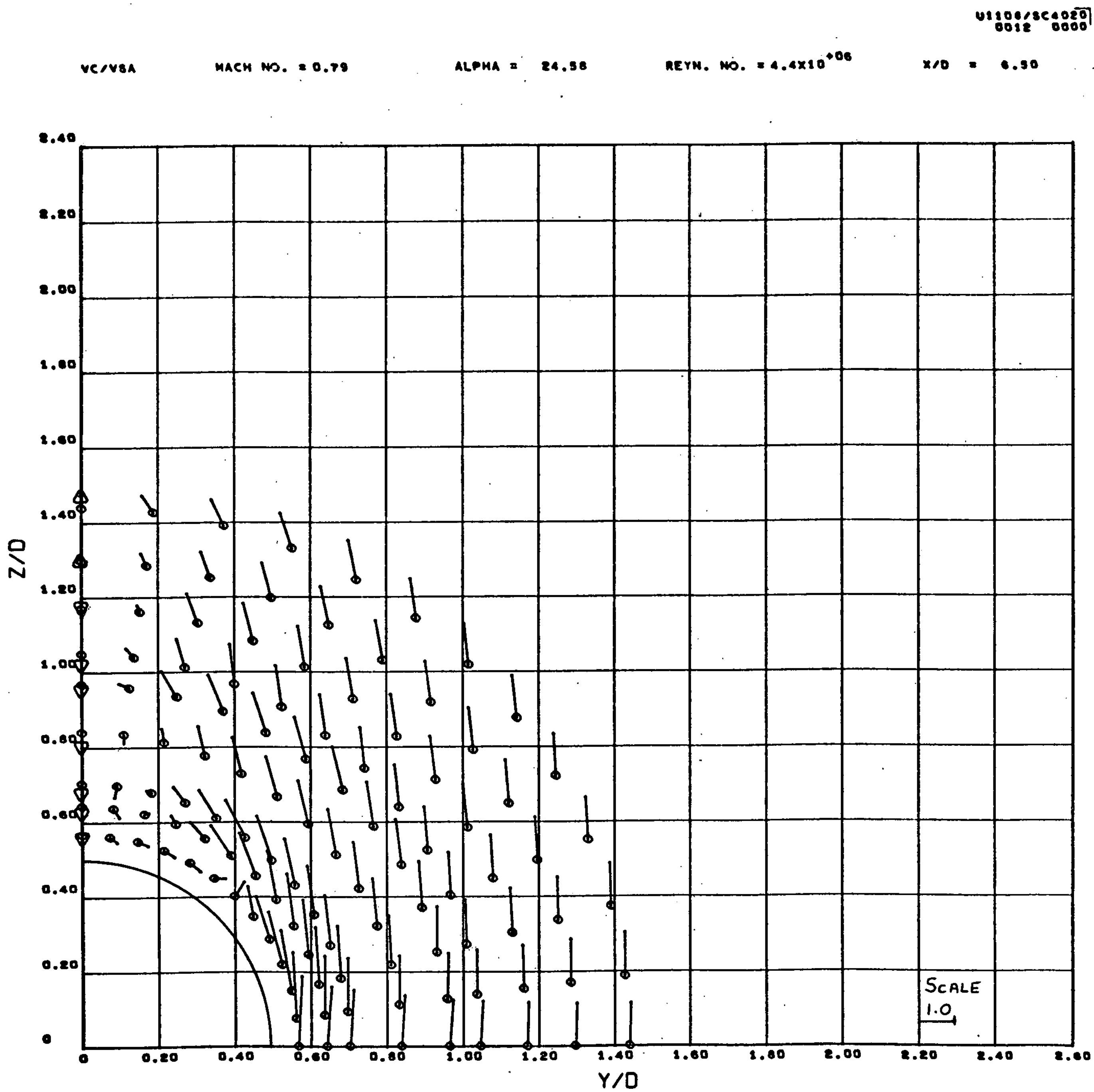

Figure 18b (cont'd) - Local Crossflow Velocity Vectors ~ $\frac{V_c}{V_\infty \sin\alpha}$

f

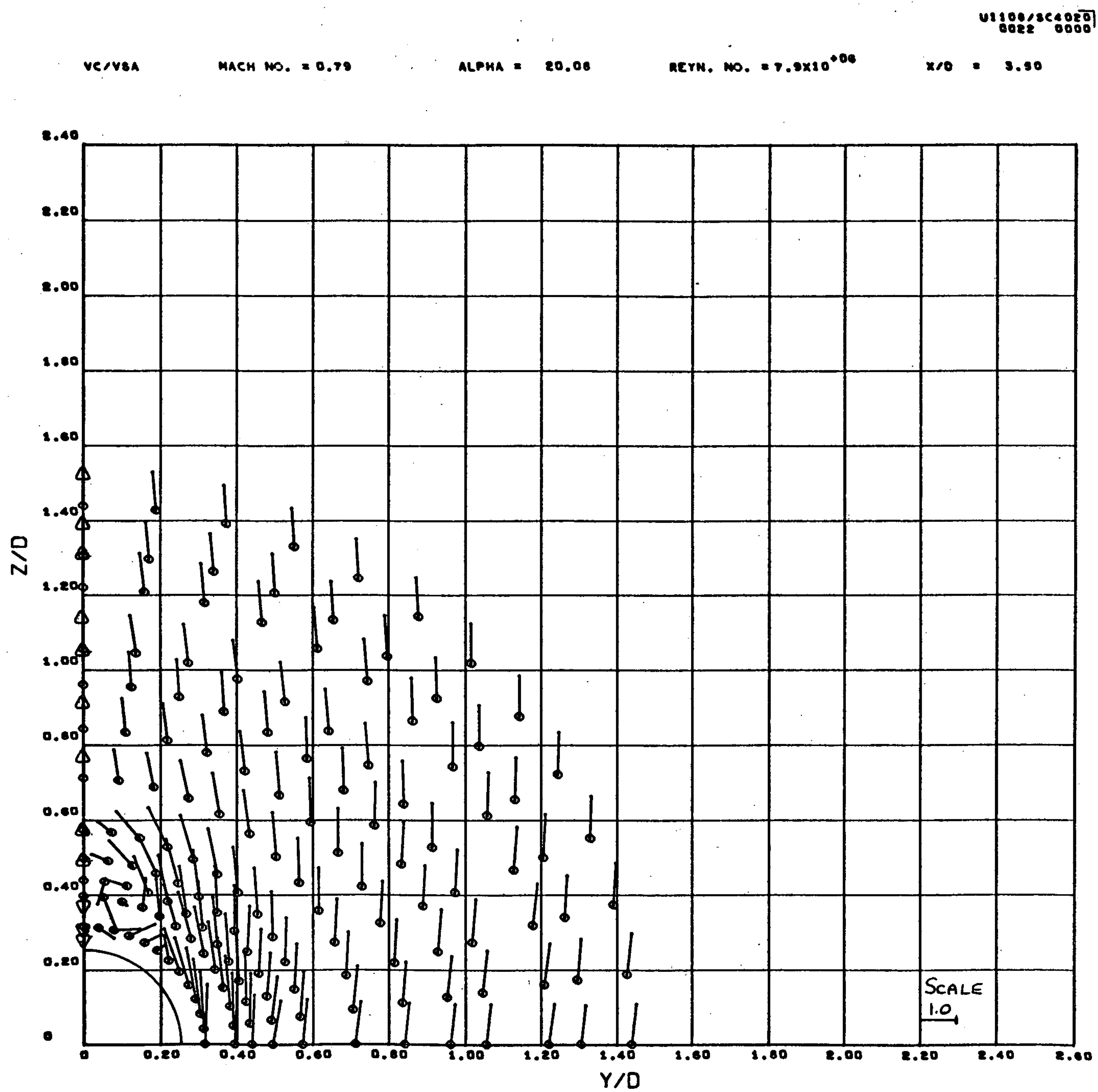

Figure 19a - Local Crossflow Velocity Vectors $\sim \frac{V_c}{V_\infty \sin\alpha}$

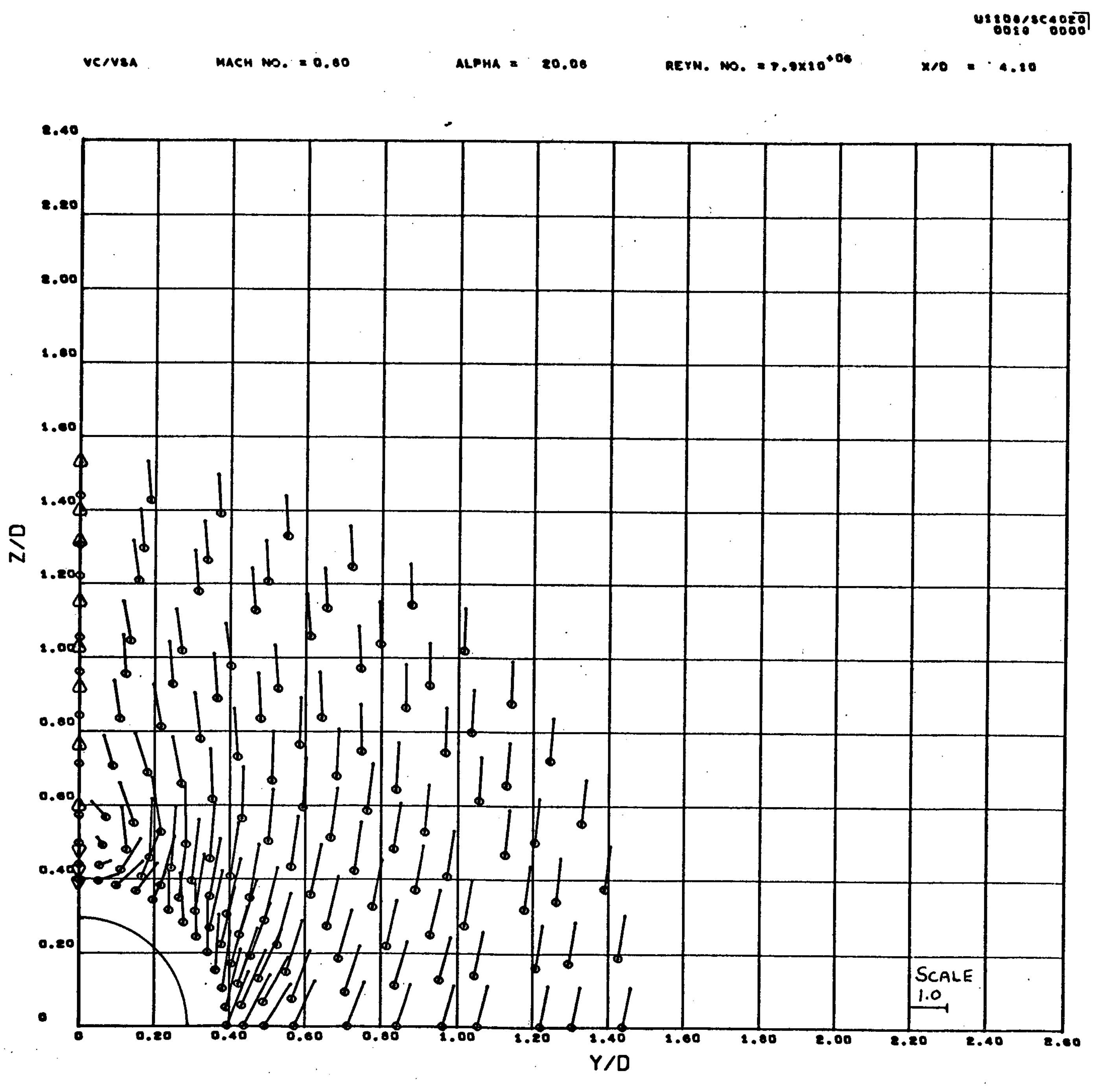

Figure 19a (cont'd) - Local Crossflow Velocity Vectors ~ $\frac{V_c}{V_\infty \sin\alpha}$

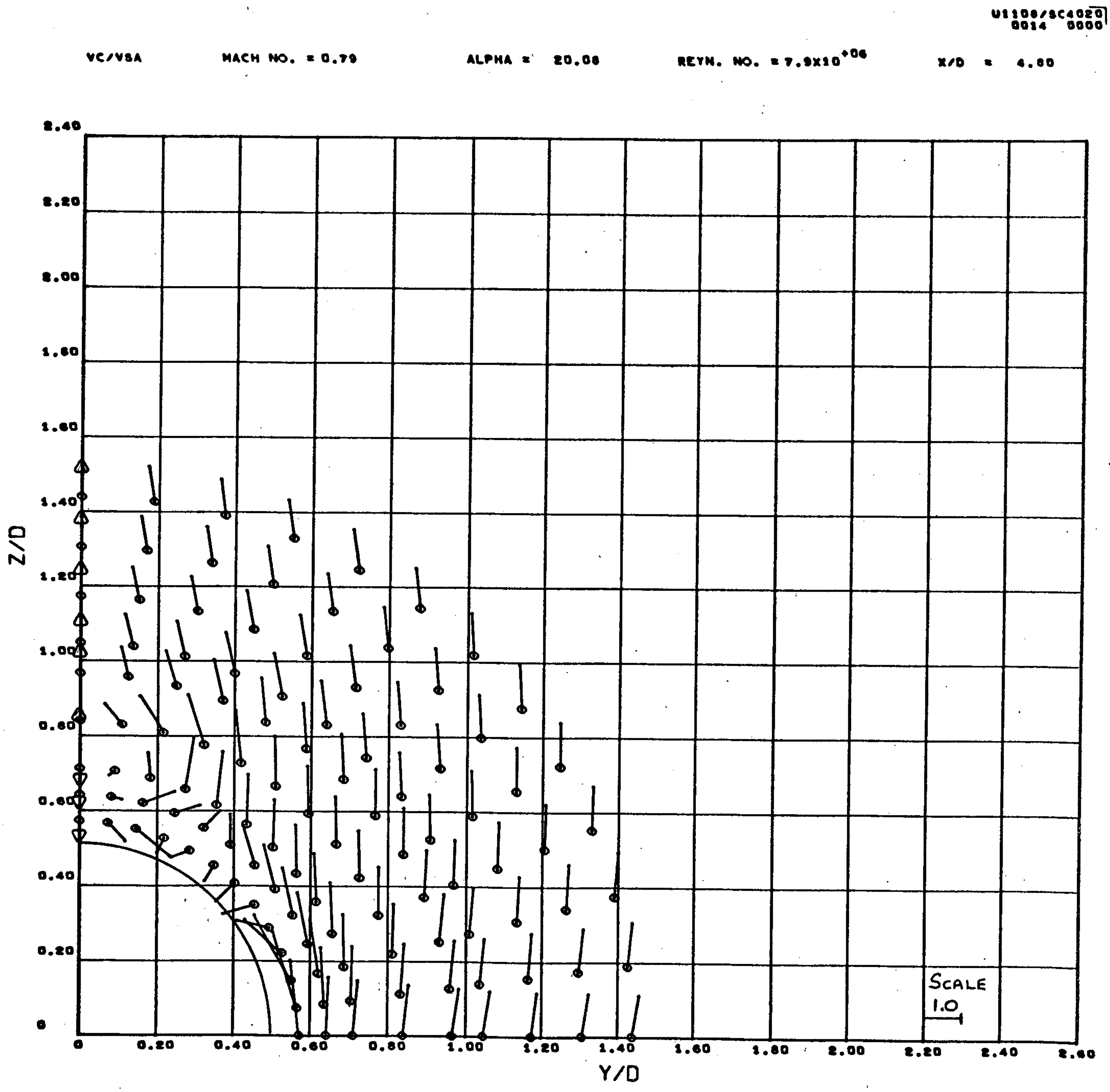

Figure 19a (cont'd) - Local Crossflow Velocity Vectors ~ $\frac{V_c}{V_\infty \sin\alpha}$

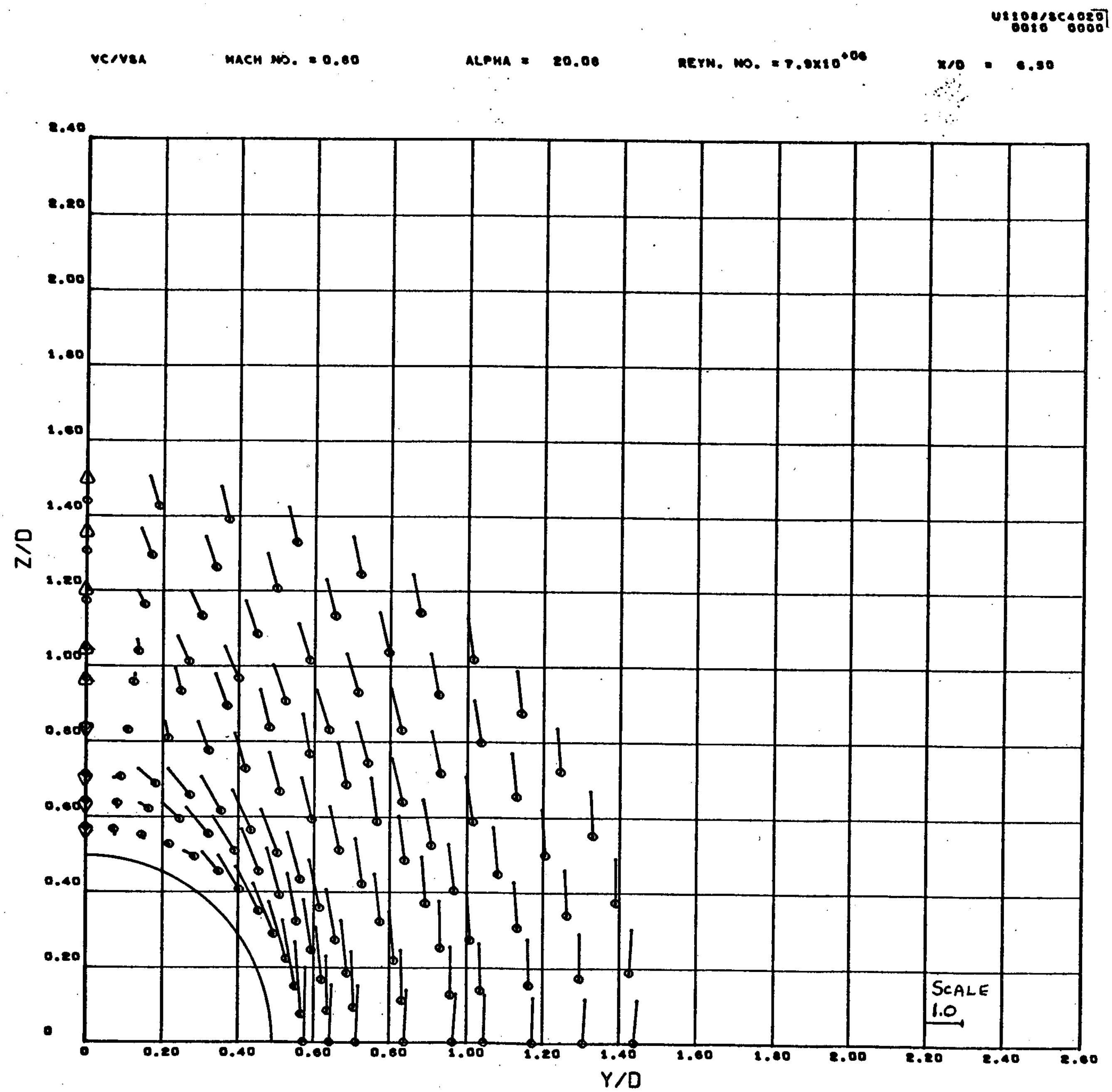

Figure 19a (cont'd) - Local Crossflow Velocity Vectors ~ $\frac{V_c}{V_\infty \sin\alpha}$

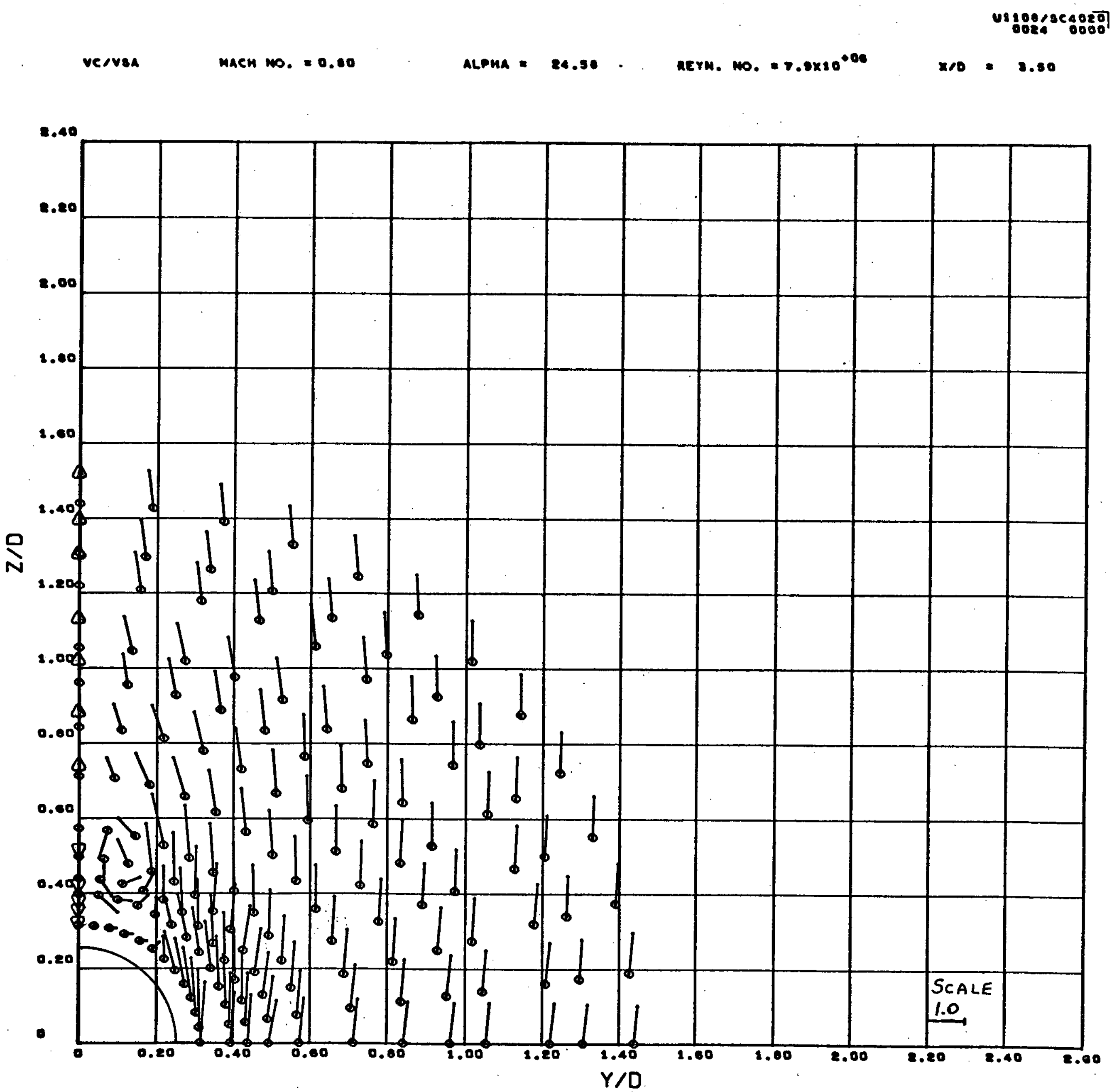

Figure 19b - Local Crossflow Velocity Vectors $\sim \frac{V_c}{V_\infty \sin\alpha}$

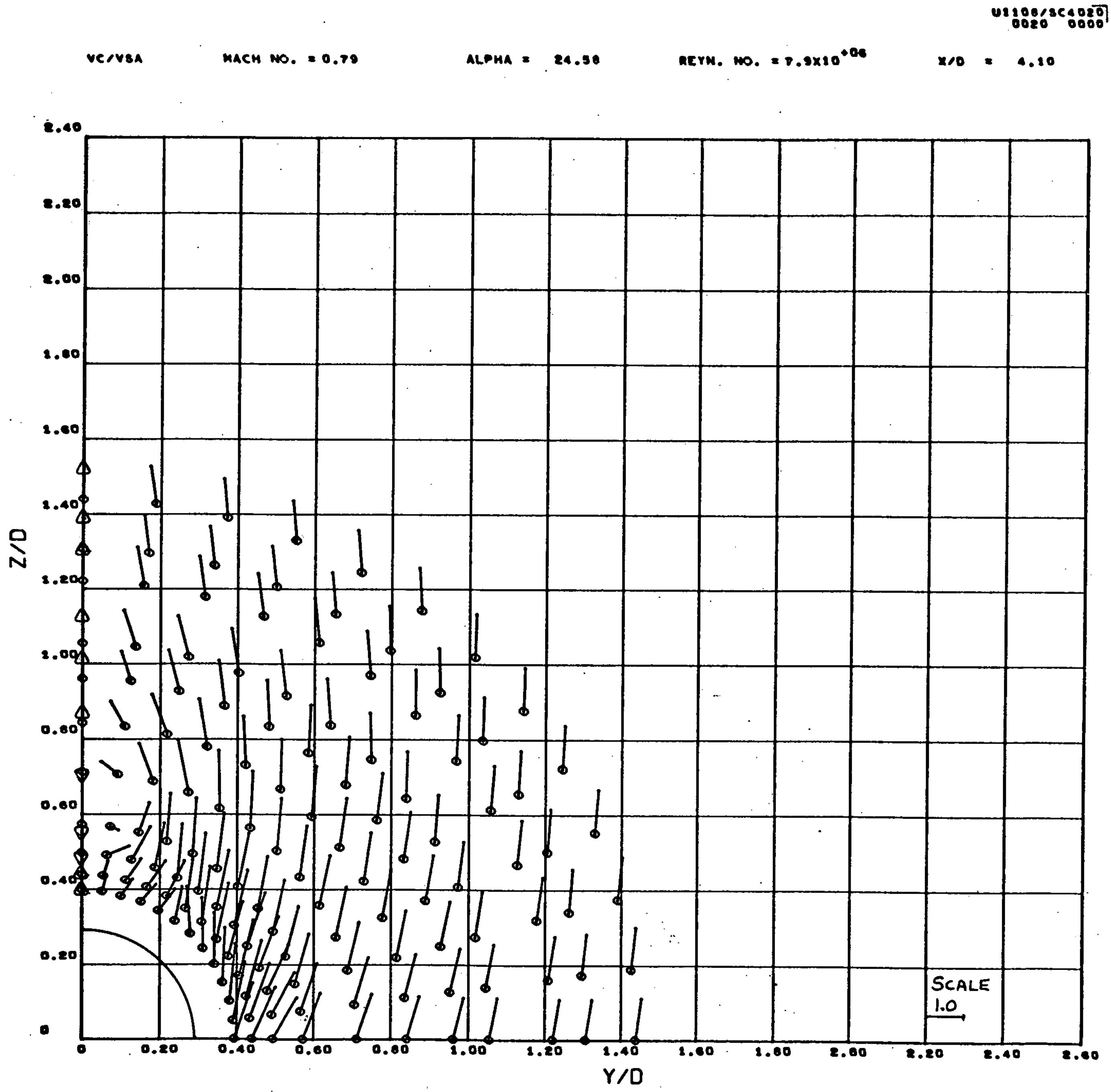

Figure 19b (cont'd) - Local Crossflow Velocity Vectors ~ $\frac{V_c}{V_\infty \sin\alpha}$

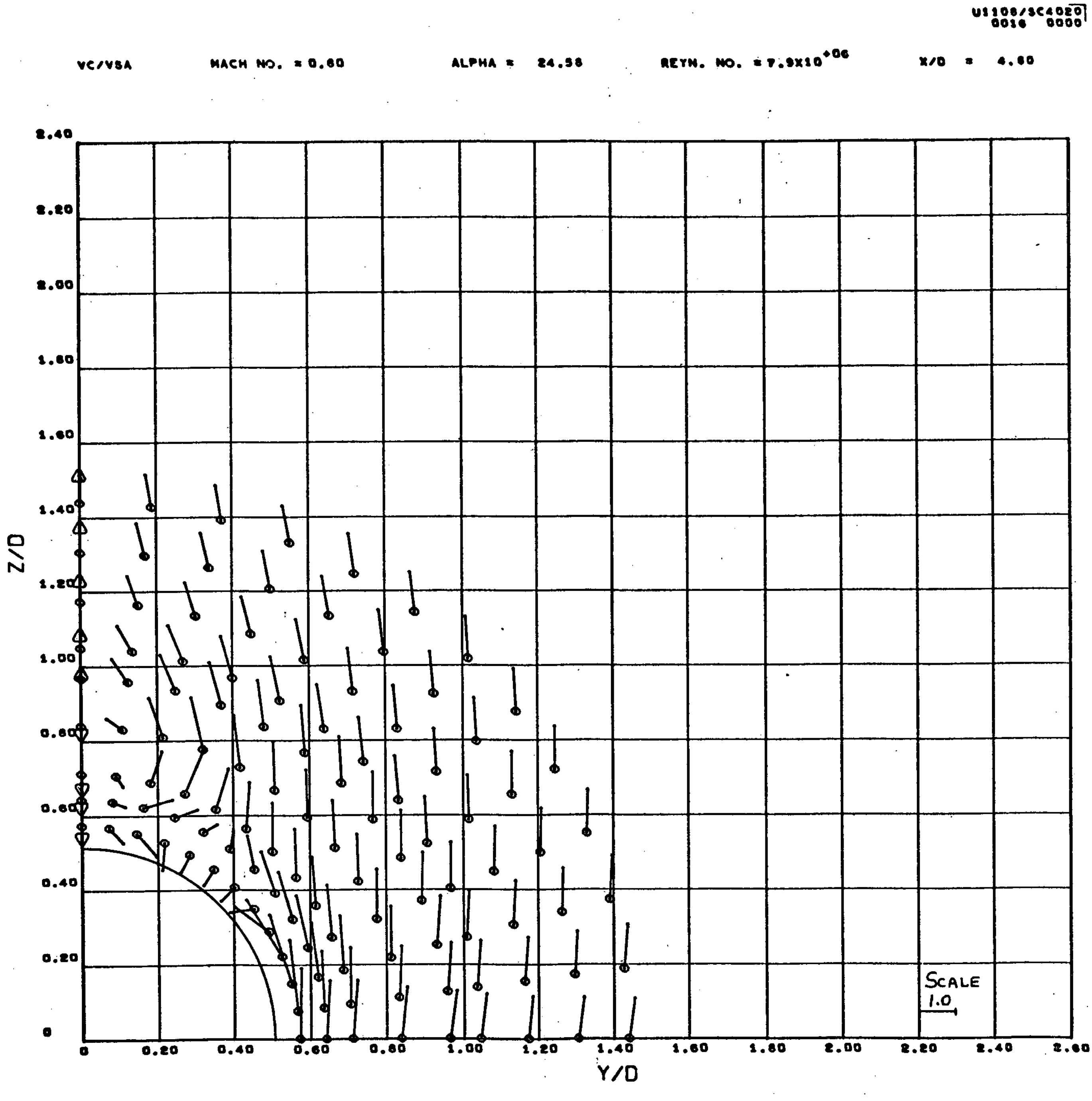

Figure 19b (cont'd) - Local Crossflow Velocity Vectors ~ $\frac{V_c}{V_\infty \sin\alpha}$

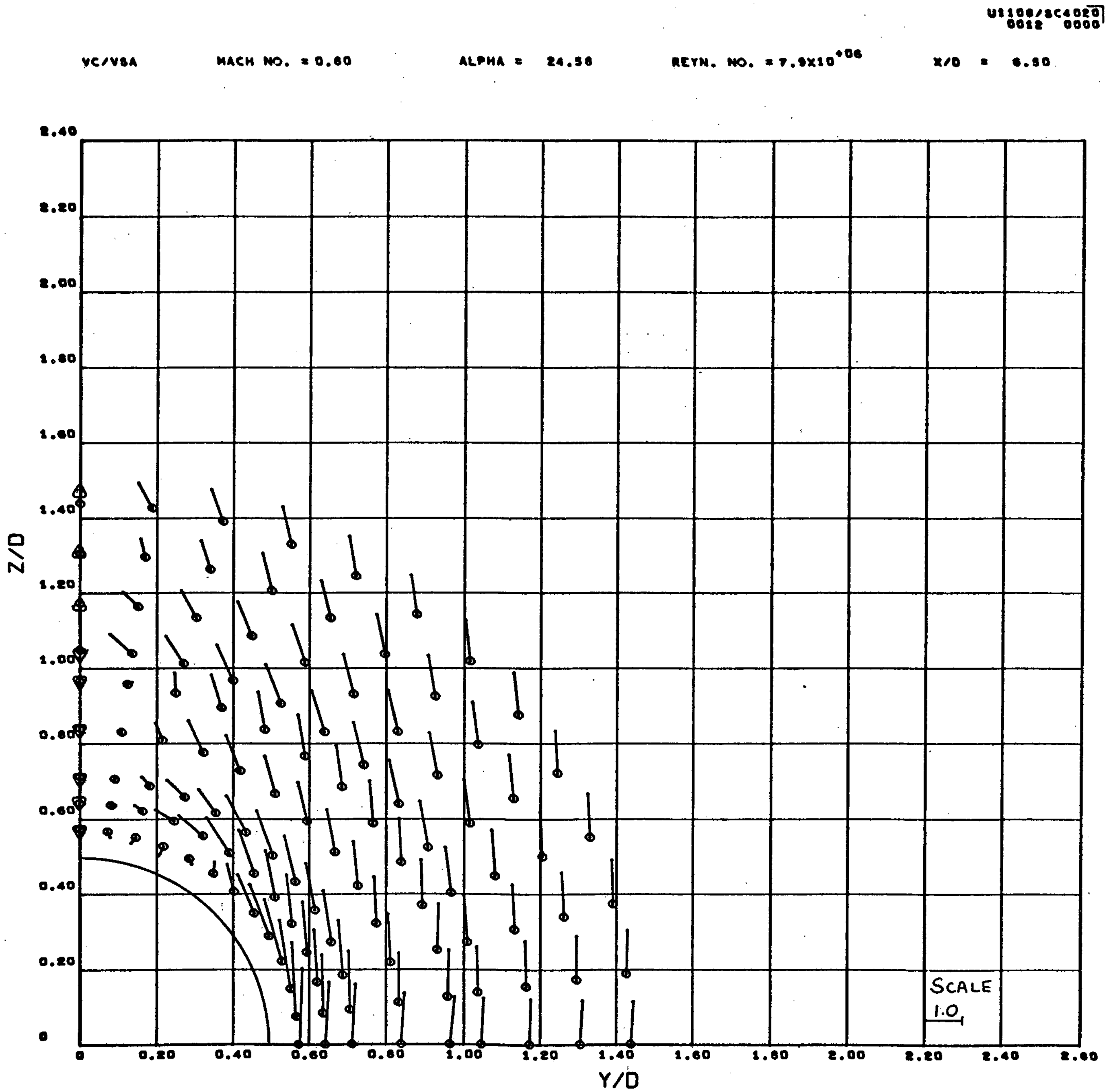

Figure 19b (cont'd) - Local Crossflow Velocity Vectors ~ $\frac{V_c}{V_\infty \sin\alpha}$

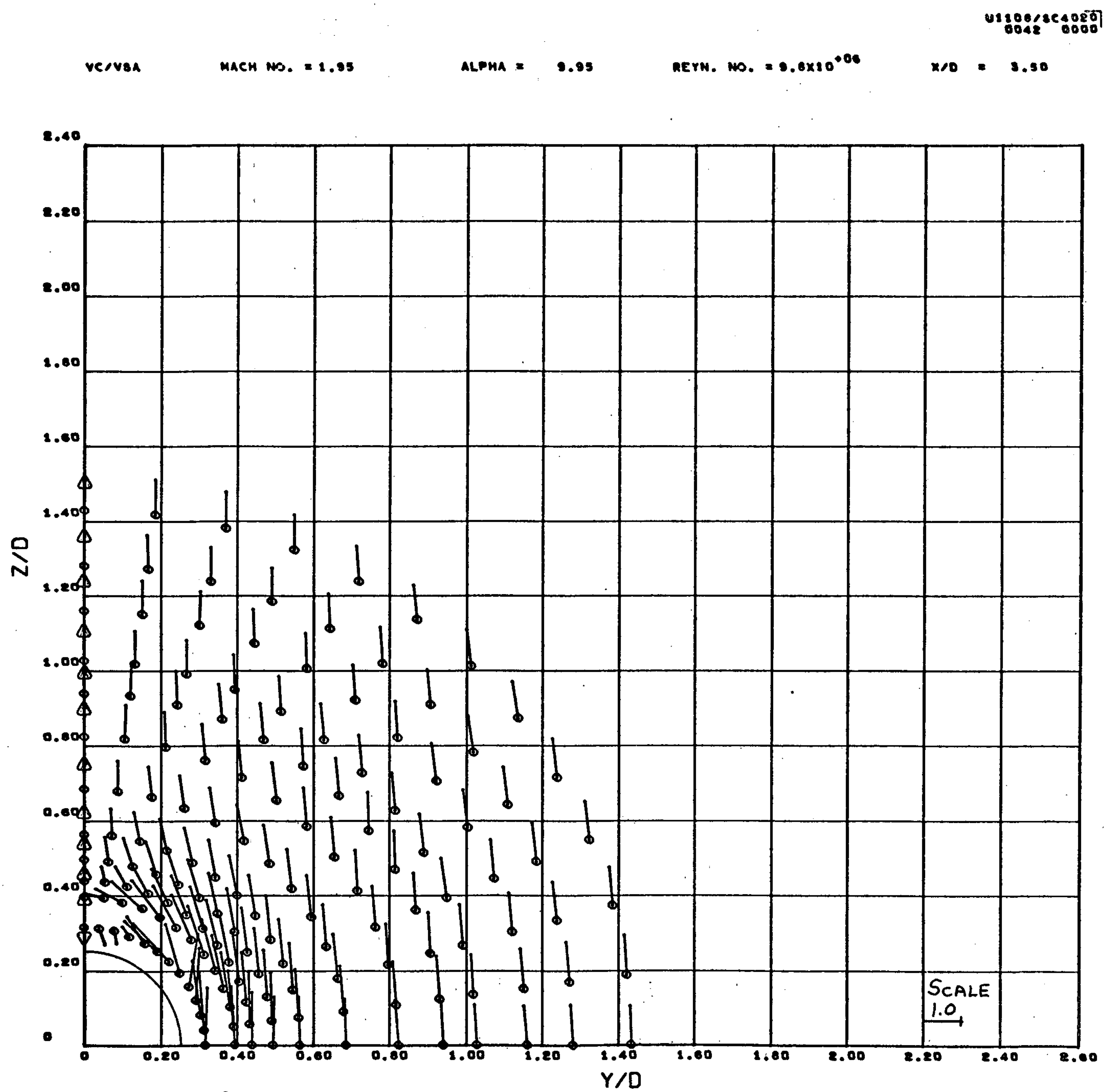

Figure 20a - Local Crossflow Velocity Vectors ~ $\frac{V_c}{V_\infty \sin\alpha}$

U1108/SC4020
0034 0000

VC/VSA MACH NO. = 1.96 ALPHA = 9.95 REYN. NO. = $9.7 \times 10^{+06}$ X/D = 4.10

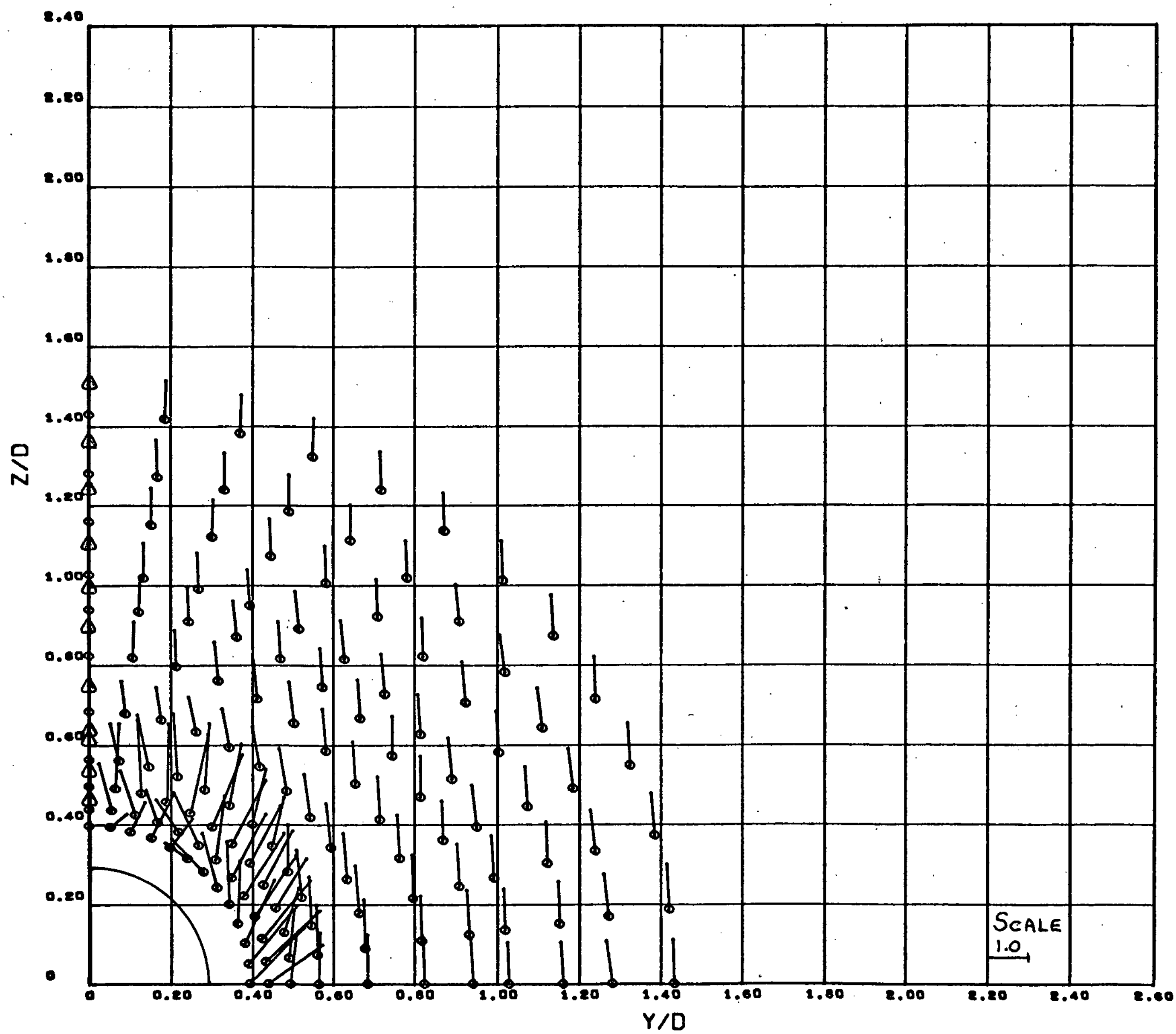

Figure 20a (cont'd) - Local Crossflow Velocity Vectors ~ $\frac{V_c}{V_\infty \sin\alpha}$

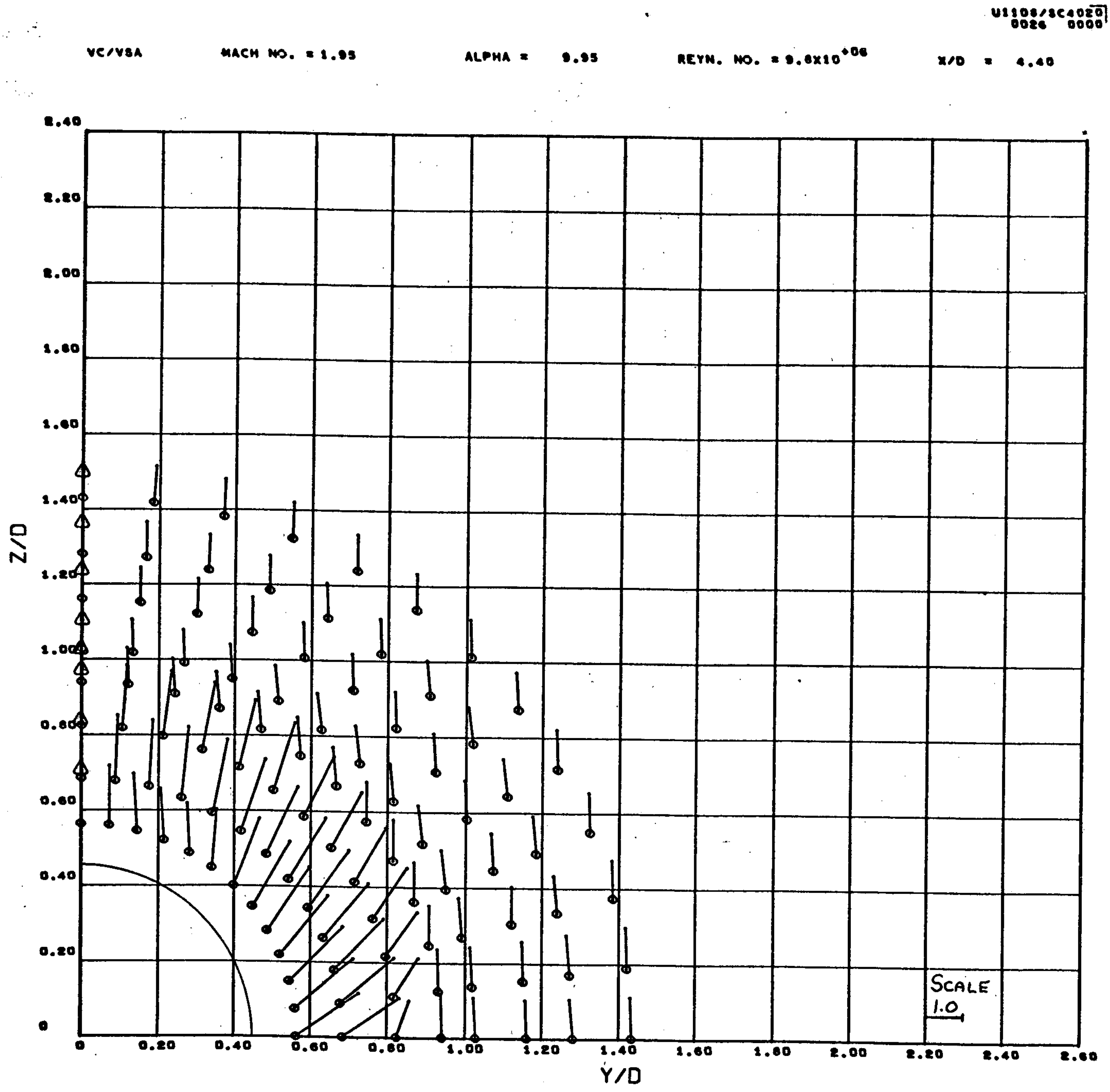

Figure 20a (cont'd) - Local Crossflow Velocity Vectors ~ $\frac{V_c}{V_\infty \sin\alpha}$

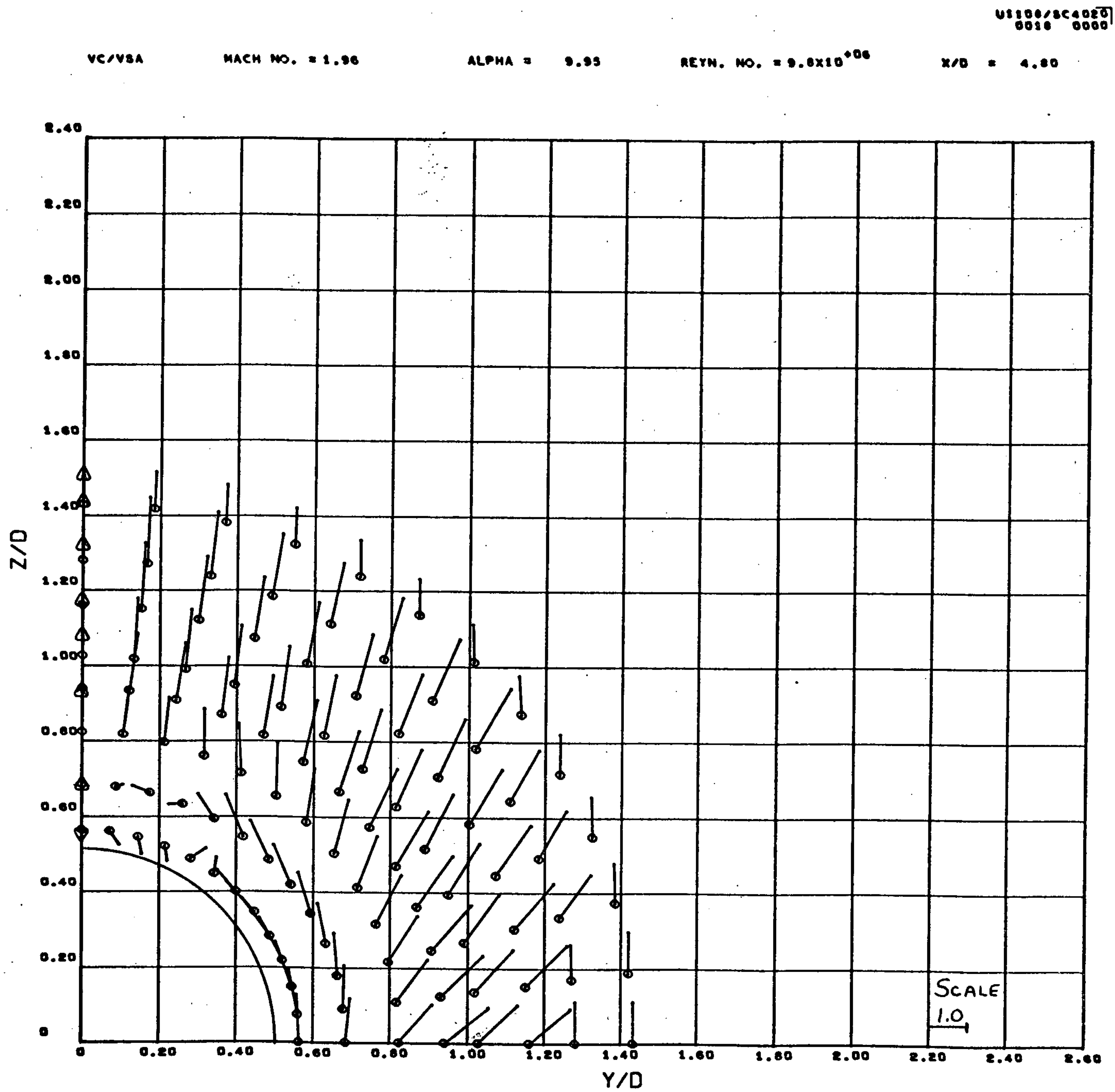

Figure 20a (cont'd) - Local Crossflow Velocity Vectors ~ $\frac{V_c}{V_\infty \sin\alpha}$

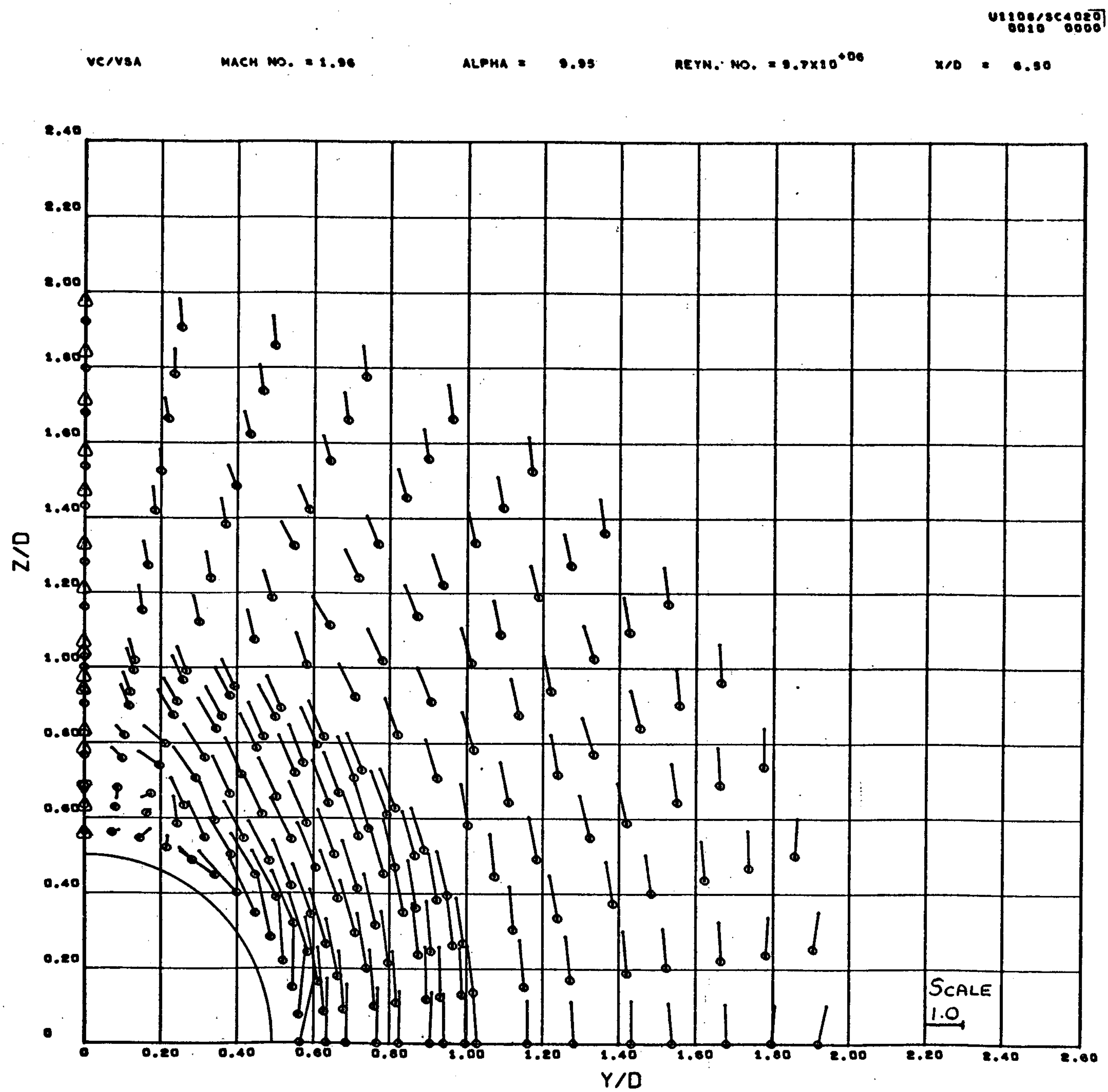

Figure 20a (cont'd) - Local Crossflow Velocity Vectors $\sim \frac{V_c}{V_\infty \sin\alpha}$

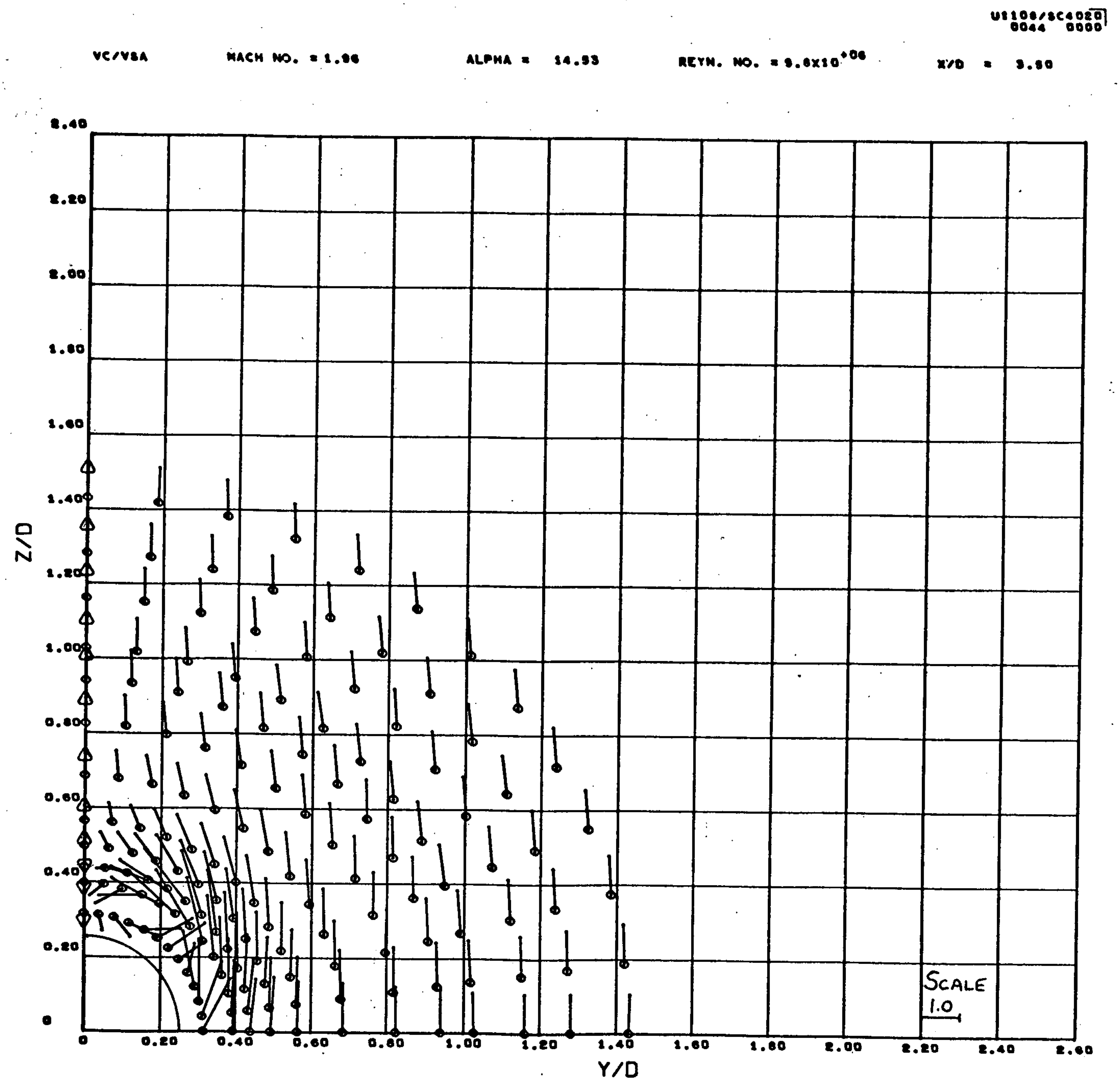

Figure 20b - Local Crossflow Velocity Vectors $\sim \frac{V_c}{V_\infty \sin\alpha}$

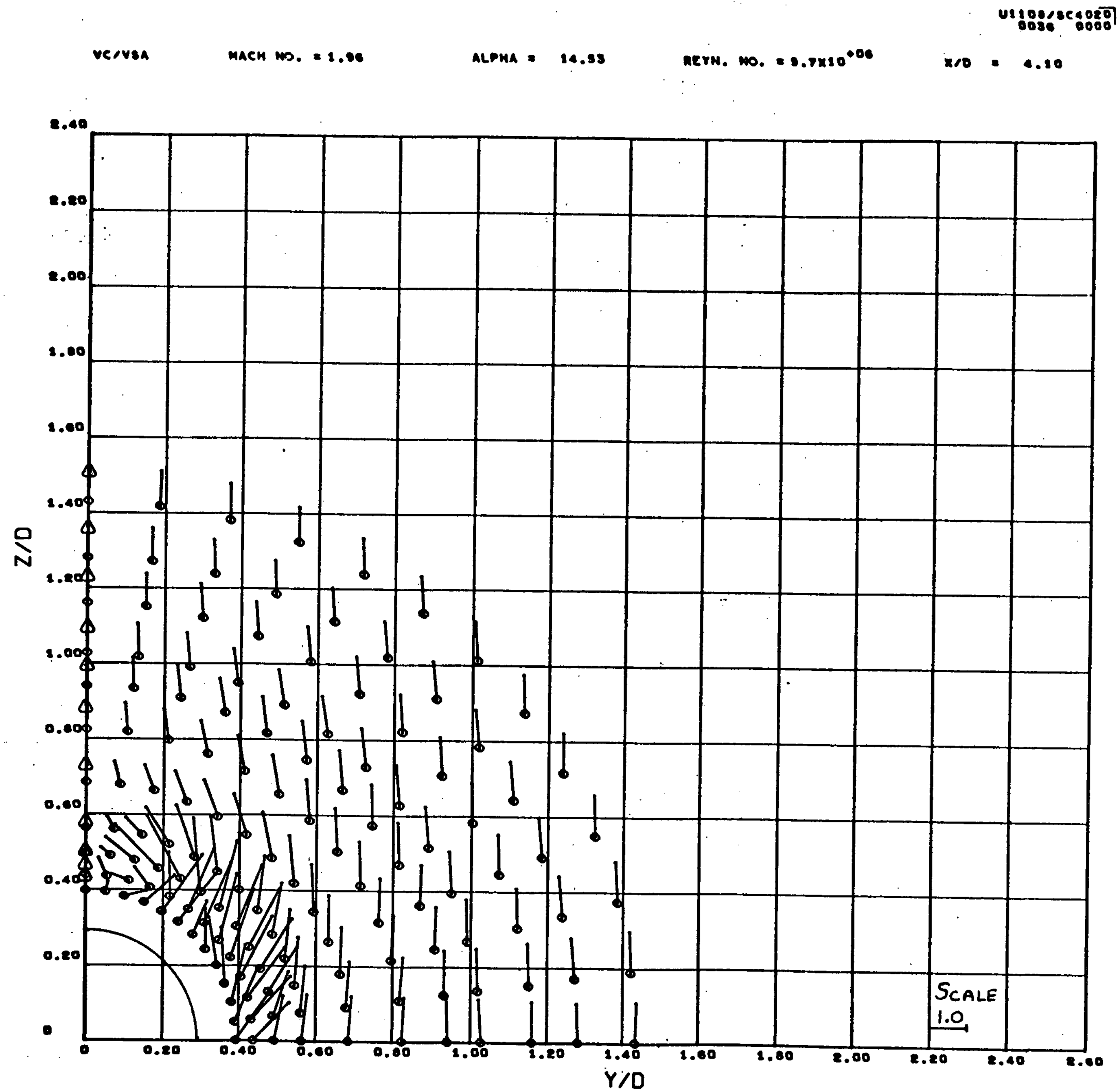

Figure 20b (cont'd) - Local Crossflow Velocity Vectors $\sim \frac{V_c}{V_\infty \sin\alpha}$

U1108/SC4020
0028 0000

VC/VSA MACH NO. = 1.95 ALPHA = 14.53 REYN. NO. = $9.8 \times 10^{+06}$ X/D = 4.40

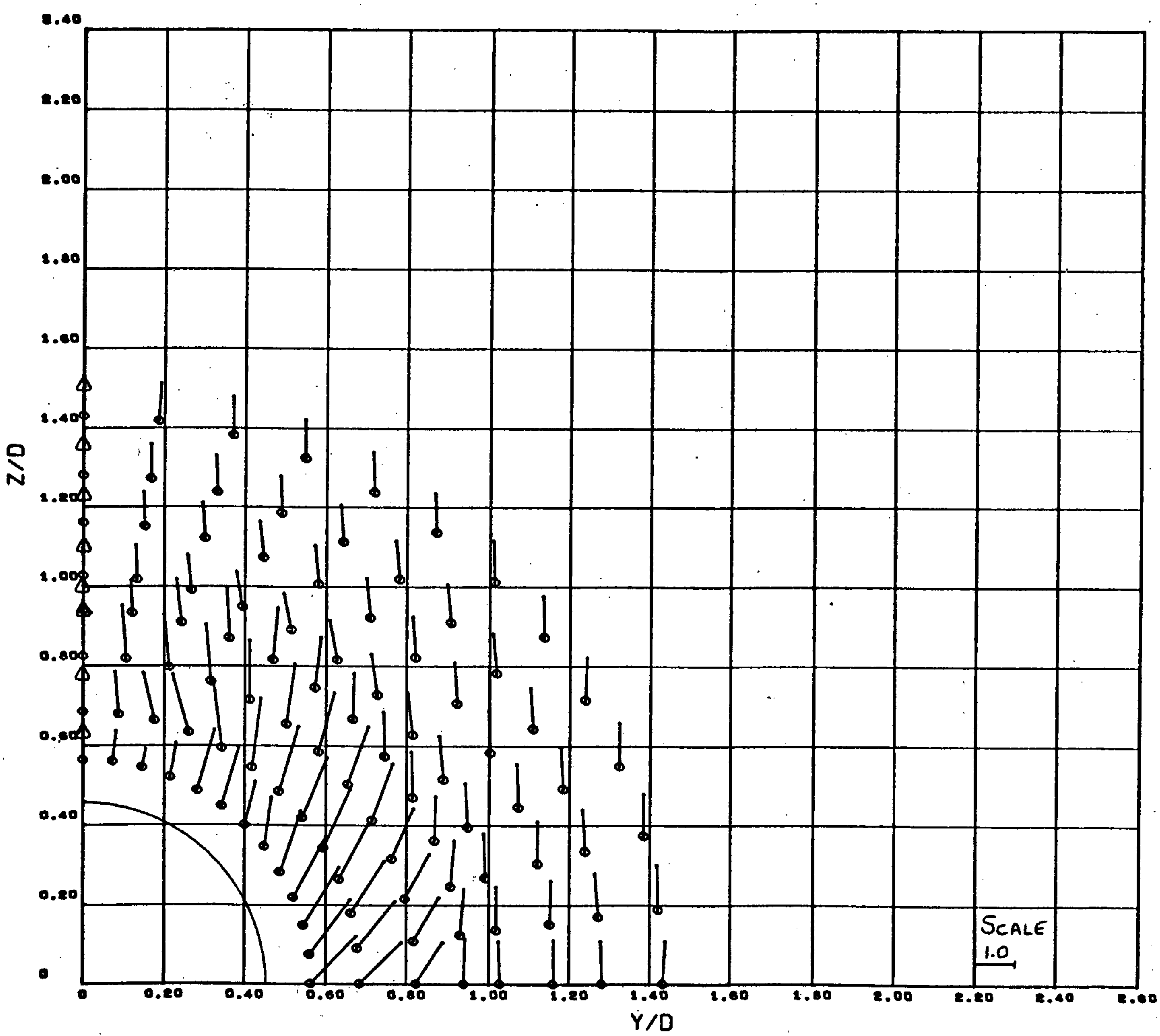

Figure 20b (cont'd) - Local Crossflow Velocity Vectors ~ $\frac{V_c}{V_\infty \sin\alpha}$

U1108/SC4020
0020 0000

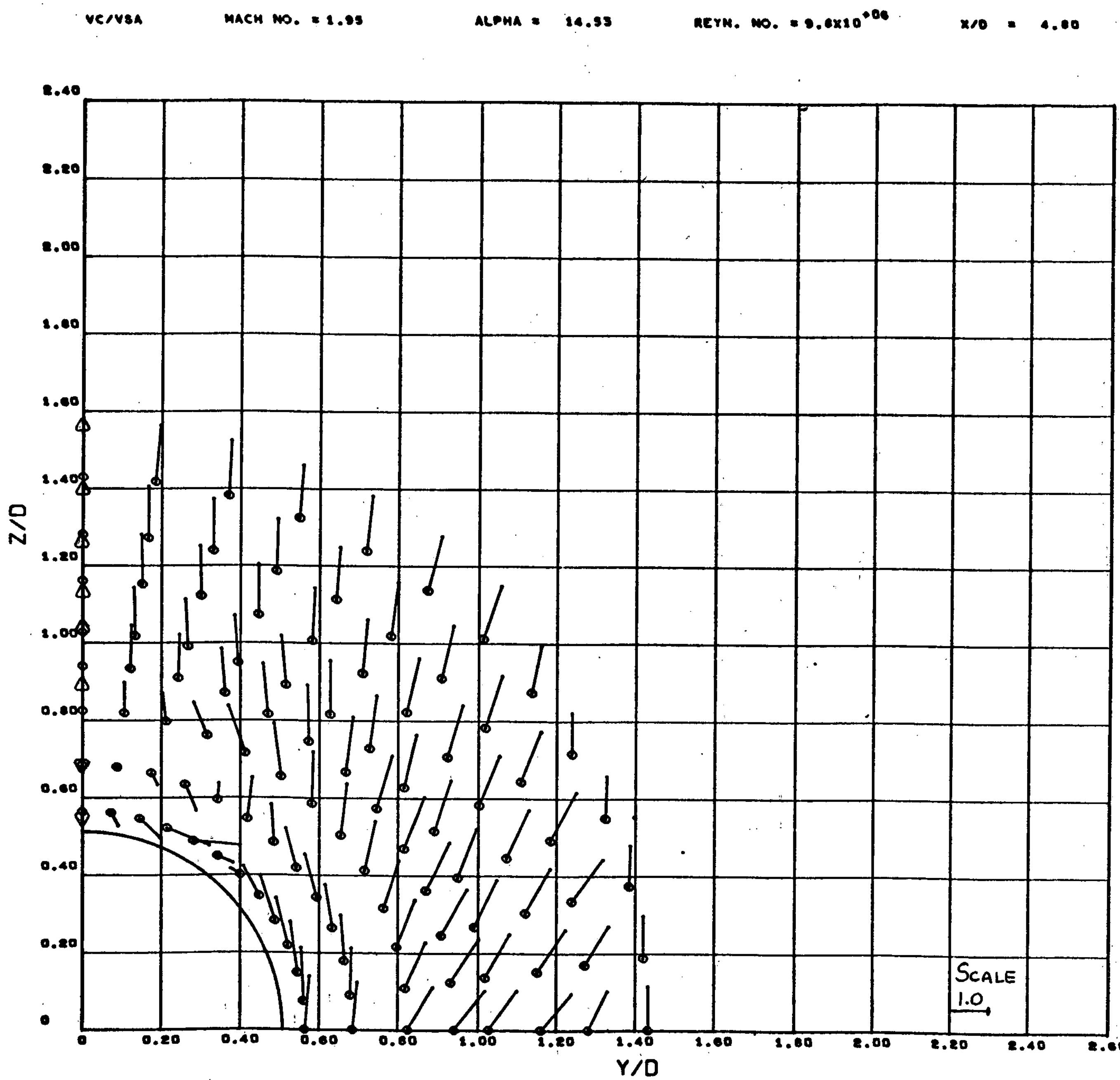

Figure 20b (cont'd) - Local Crossflow Velocity Vectors $\sim \frac{V_c}{V_\infty \sin\alpha}$

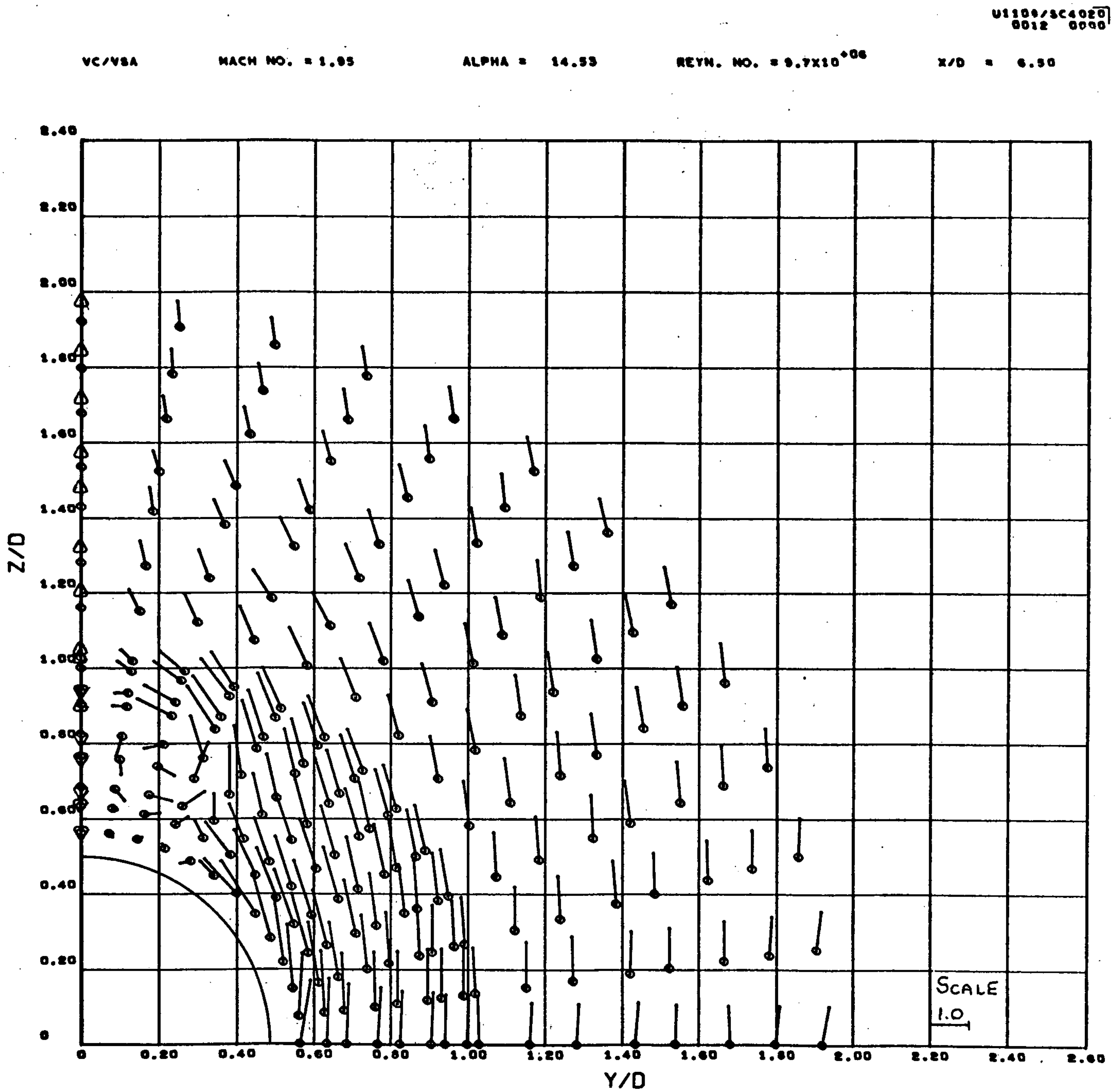

Figure 20b (cont'd) - Local Crossflow Velocity Vectors $\sim \frac{V_c}{V_\infty \sin\alpha}$

U1108/SC4020
0046 0000

VC/VSA MACH NO. = 1.96 ALPHA = 20.25 REYN. NO. = 9.8X10^{+06} X/D = 3.50

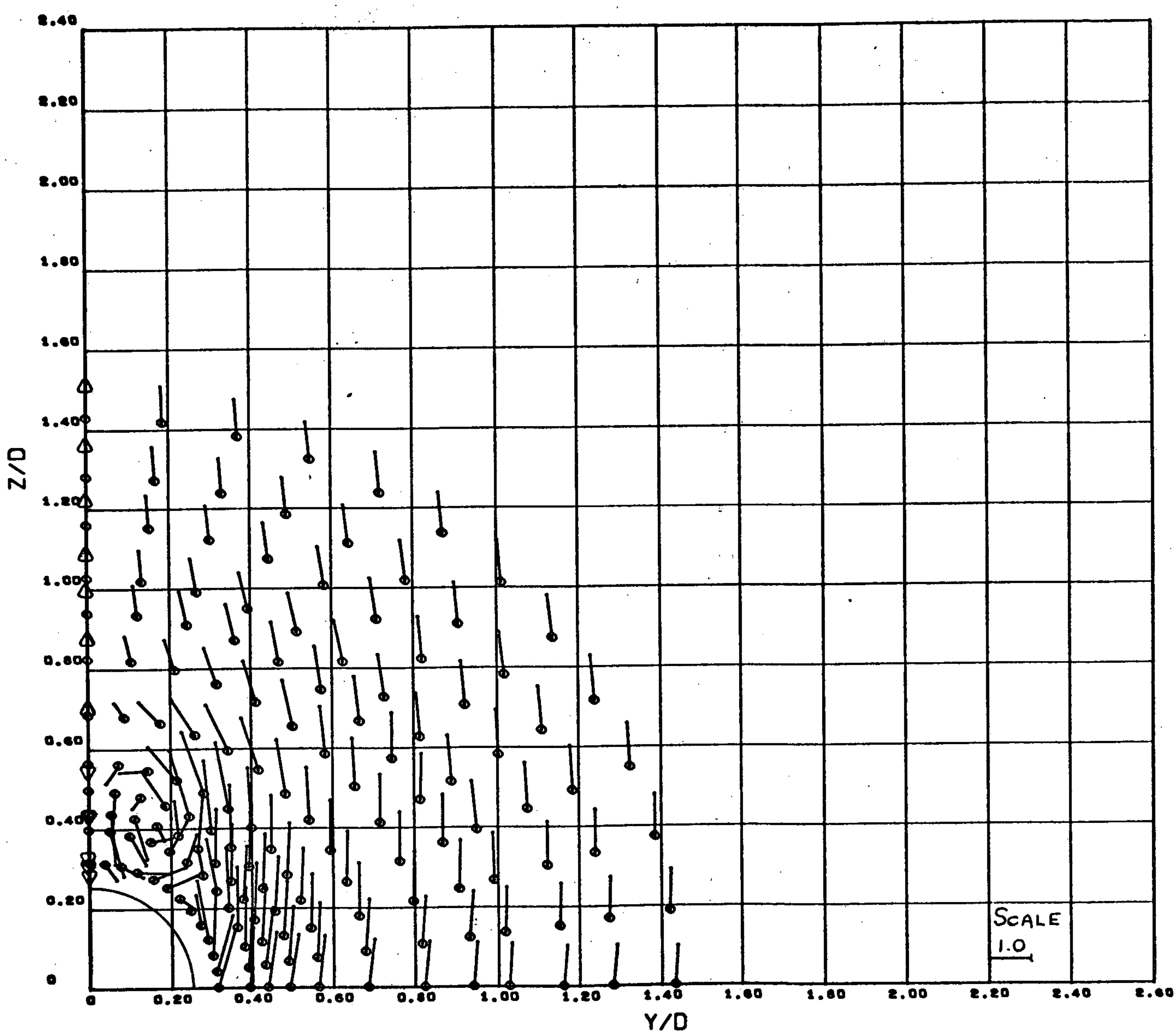

Figure 20c - Local Crossflow Velocity Vectors $\sim \frac{V_C}{V_\infty \sin\alpha}$

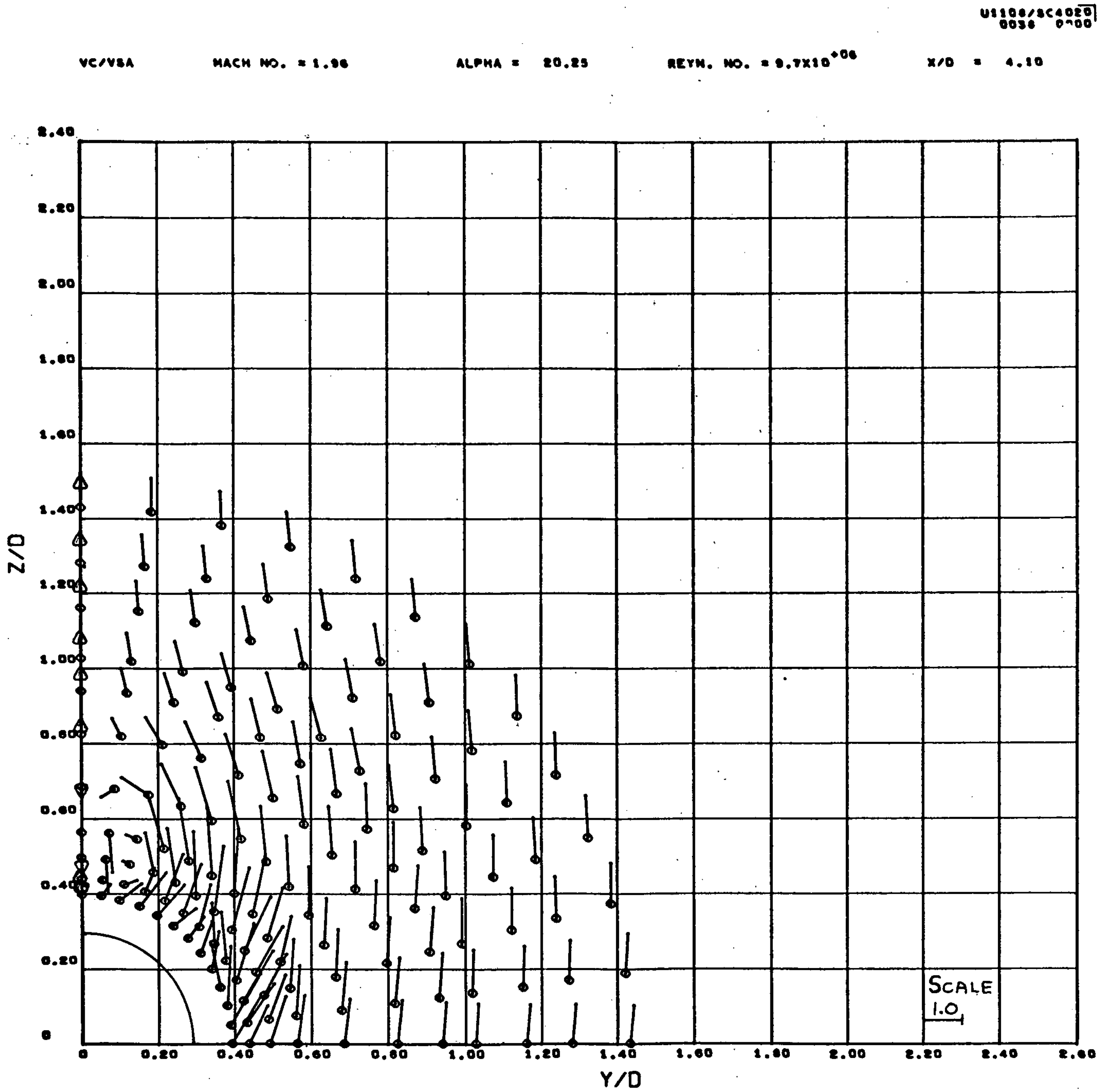

Figure 20c (cont'd) - Local Crossflow Velocity Vectors ~ $\dfrac{V_c}{V_\infty \sin\alpha}$

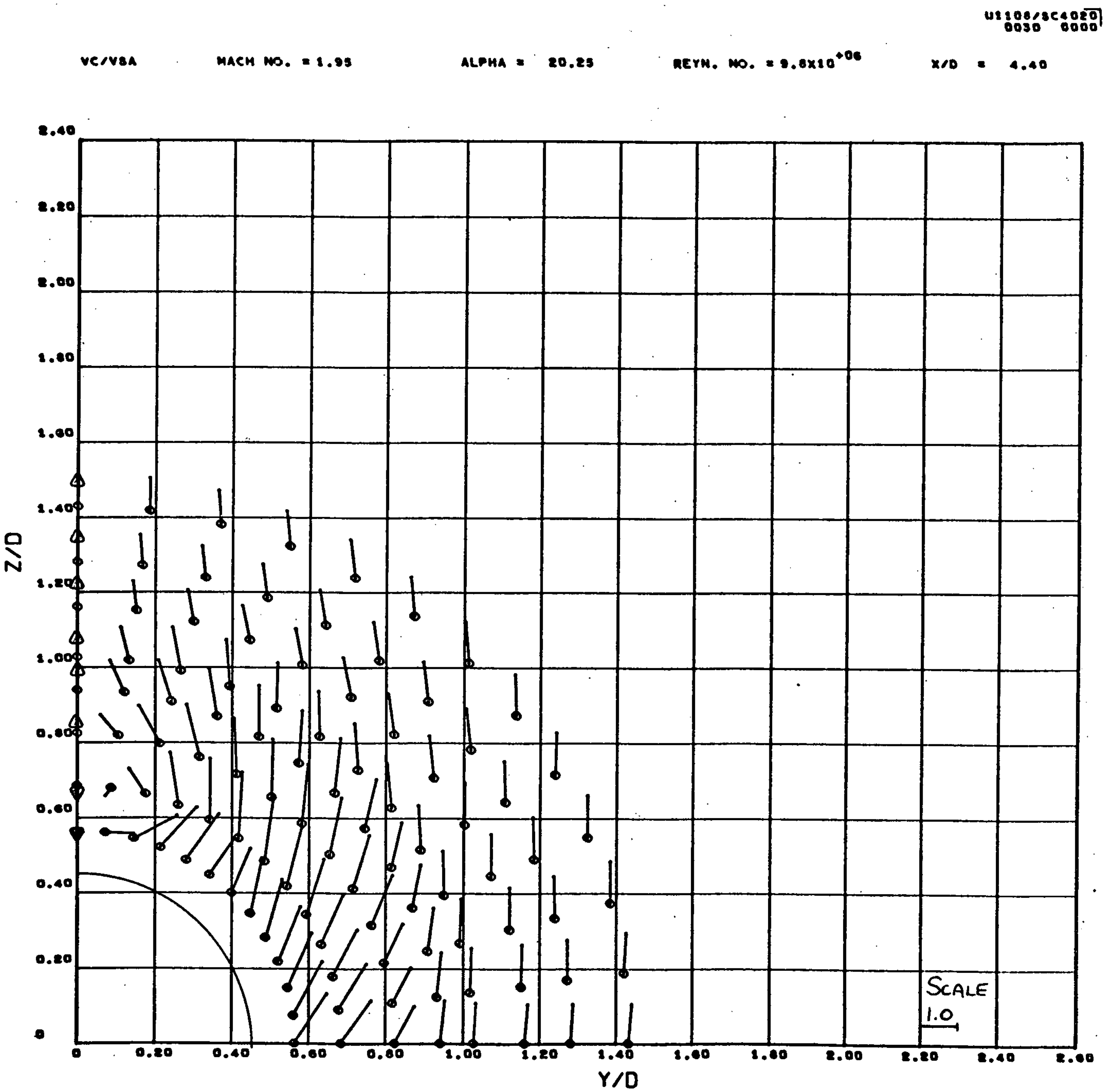

Figure 20c (cont'd) - Local Crossflow Velocity Vectors ~ $\frac{V_c}{V_\infty \sin\alpha}$

U1108/SC4020
0022 0000

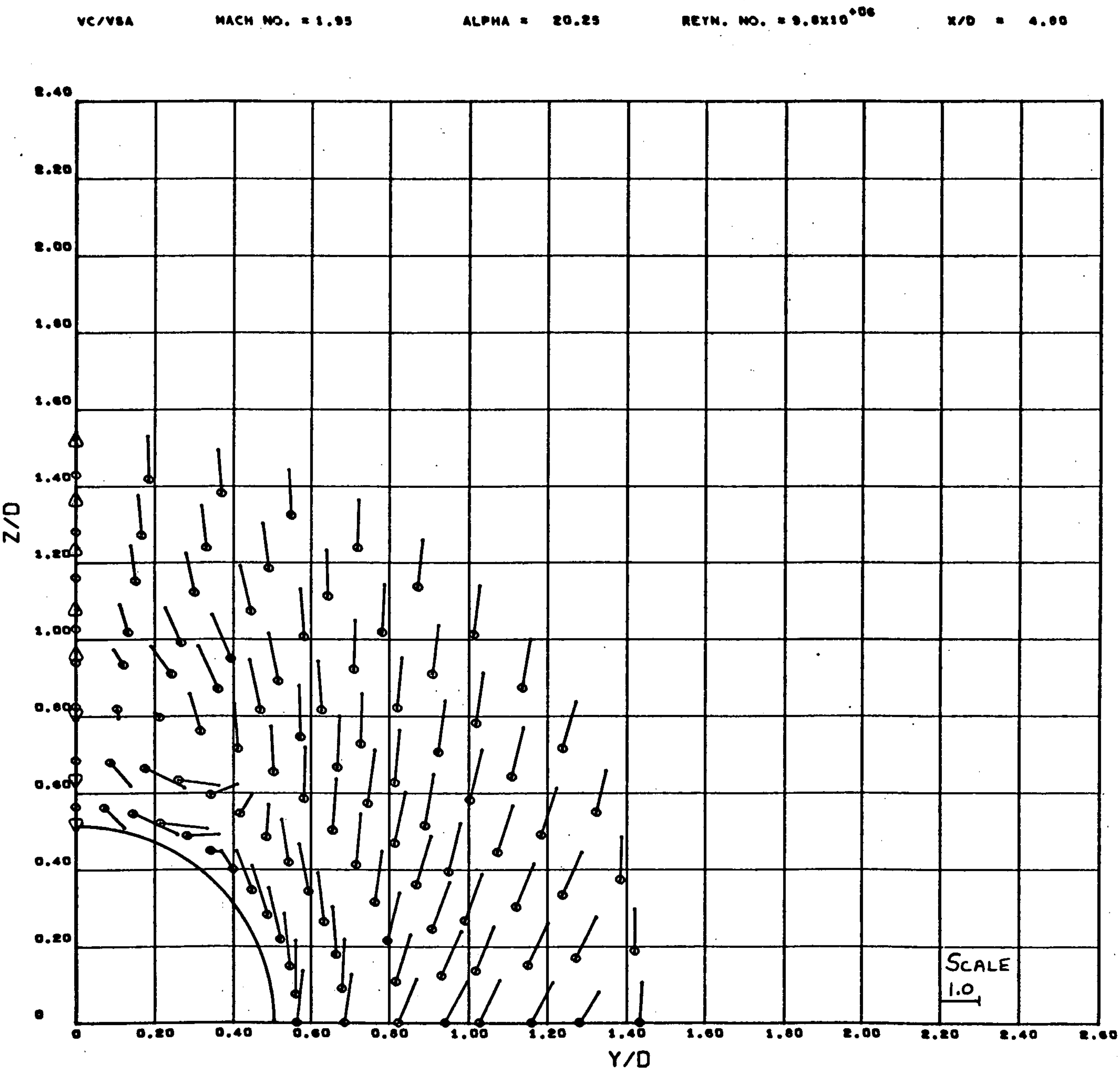

Figure 20c (cont'd) - Local Crossflow Velocity Vectors $\sim \frac{V_c}{V_\infty \sin\alpha}$

U1100/SC4020
0014 0000

VC/VSA   MACH NO. = 1.96   ALPHA = 20.25   REYN. NO. = 9.7X10^{+06} X/D = 6.50

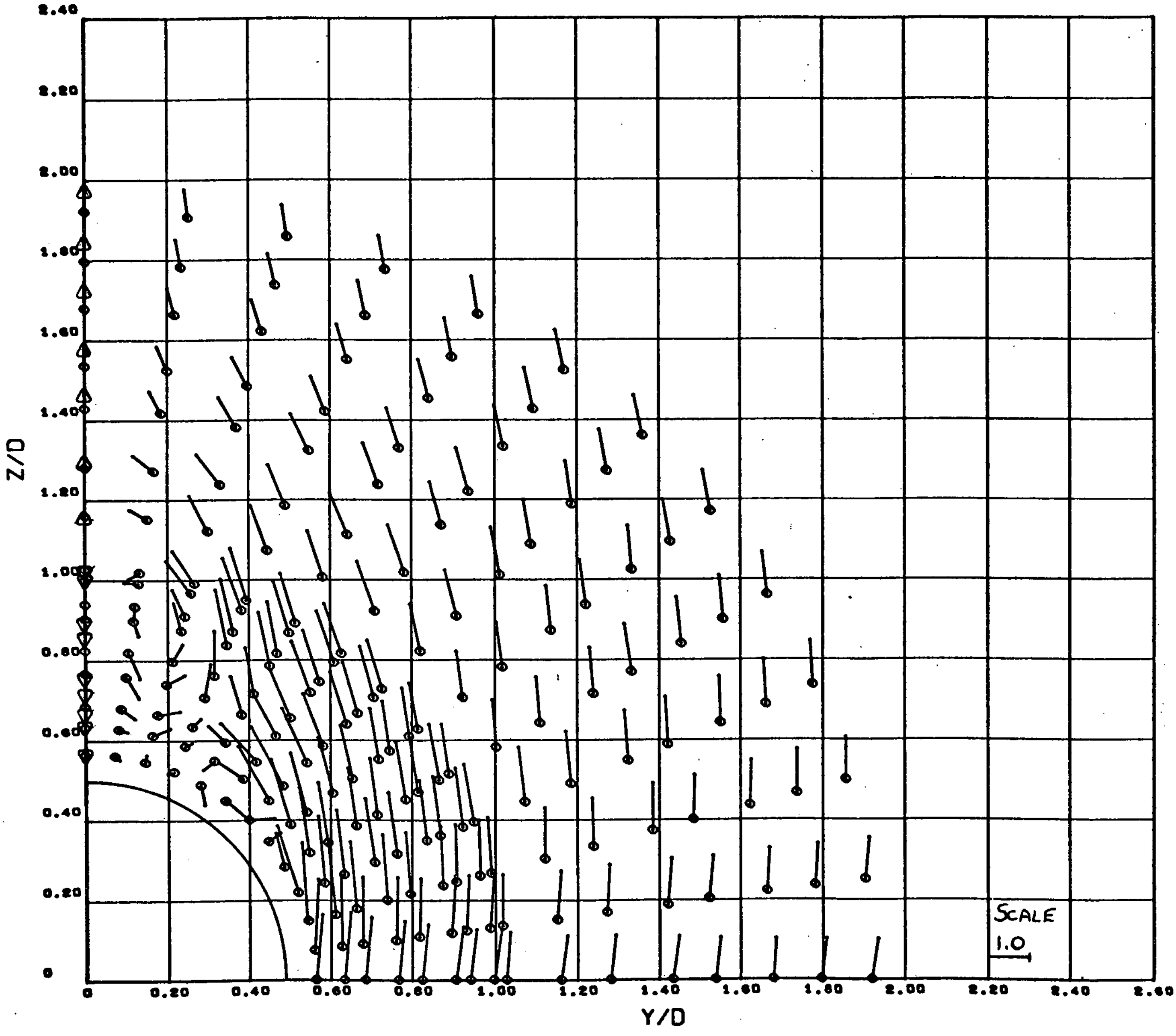

Figure 20c (cont'd) - Local Crossflow Velocity Vectors ~ $\frac{V_c}{V_\infty \sin\alpha}$

U1108/SC4020
0048 0000

VC/VSA MACH NO. = 1.96 ALPHA = 24.82 REYN. NO. = 9.8X10^{+06} X/D = 3.80

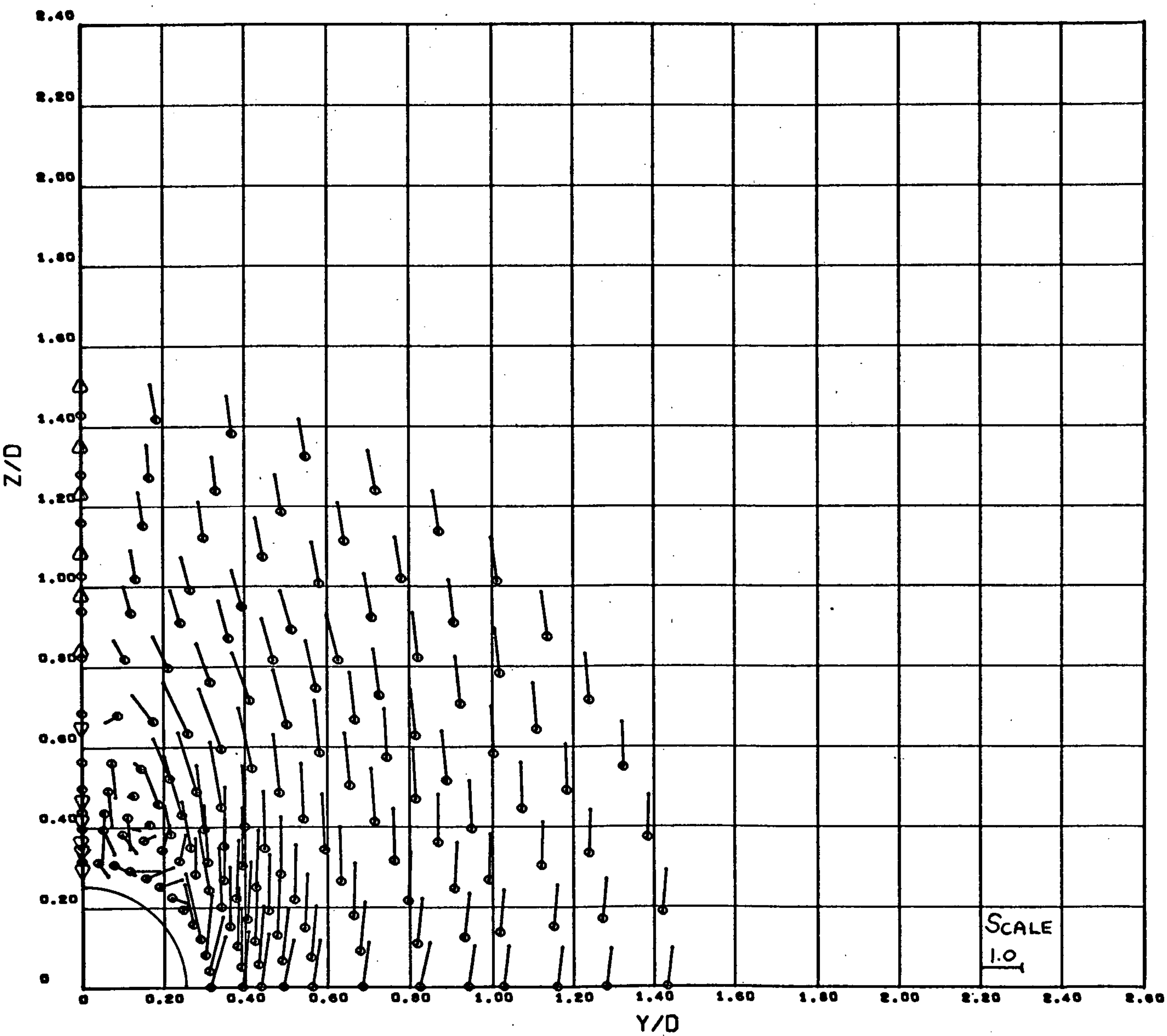

Figure 20d - Local Crossflow Velocity Vectors ~ $\frac{V_C}{V_\infty \sin\alpha}$

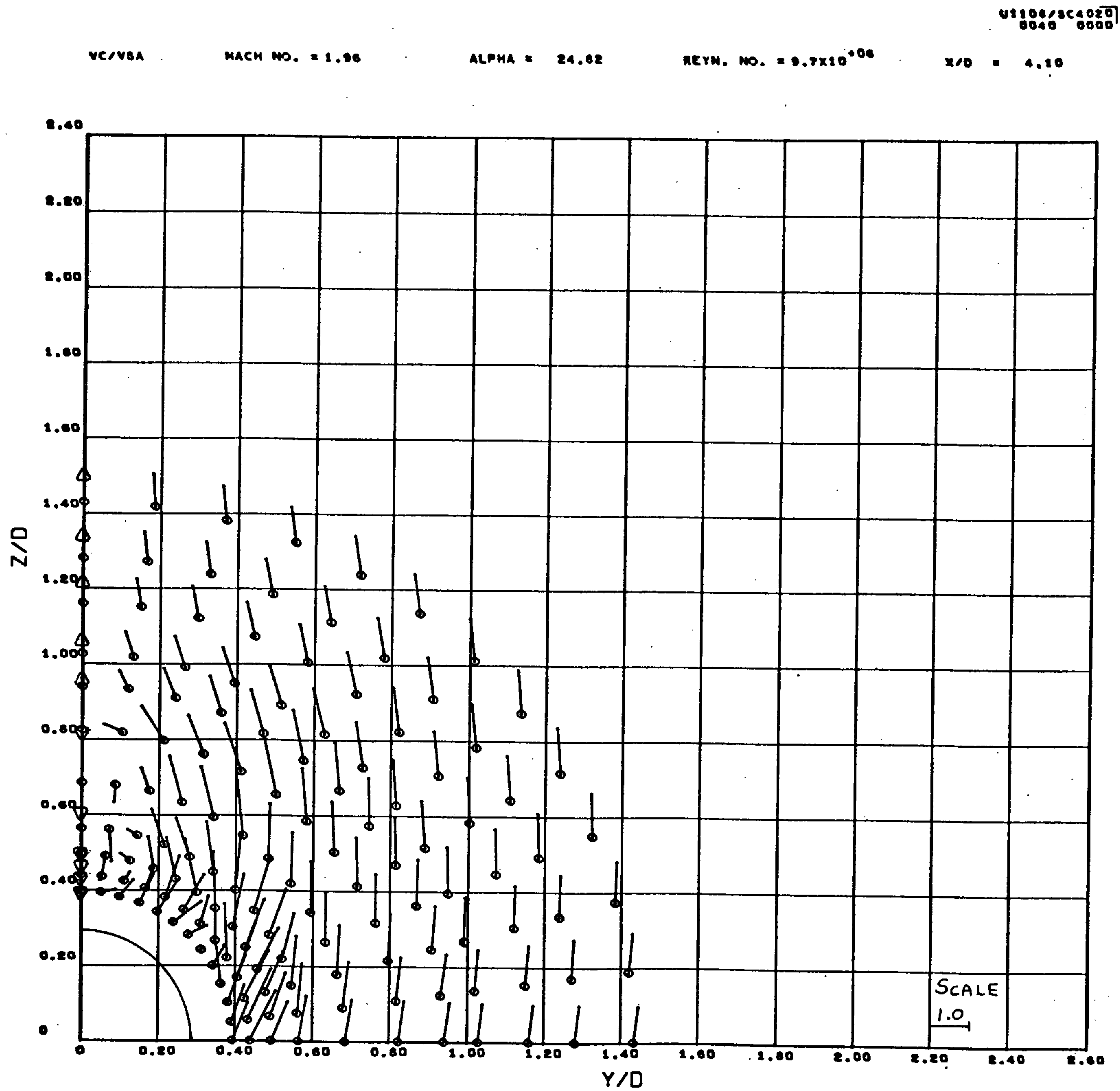

Figure 20d (cont'd) - Local Crossflow Velocity Vectors $\sim \frac{V_c}{V_\infty \sin\alpha}$

U1108/SC4020
0032 0000

VC/VSA MACH NO. = 1.96 ALPHA = 24.62 REYN. NO. = 9.6X10^{+06} X/D = 4.40

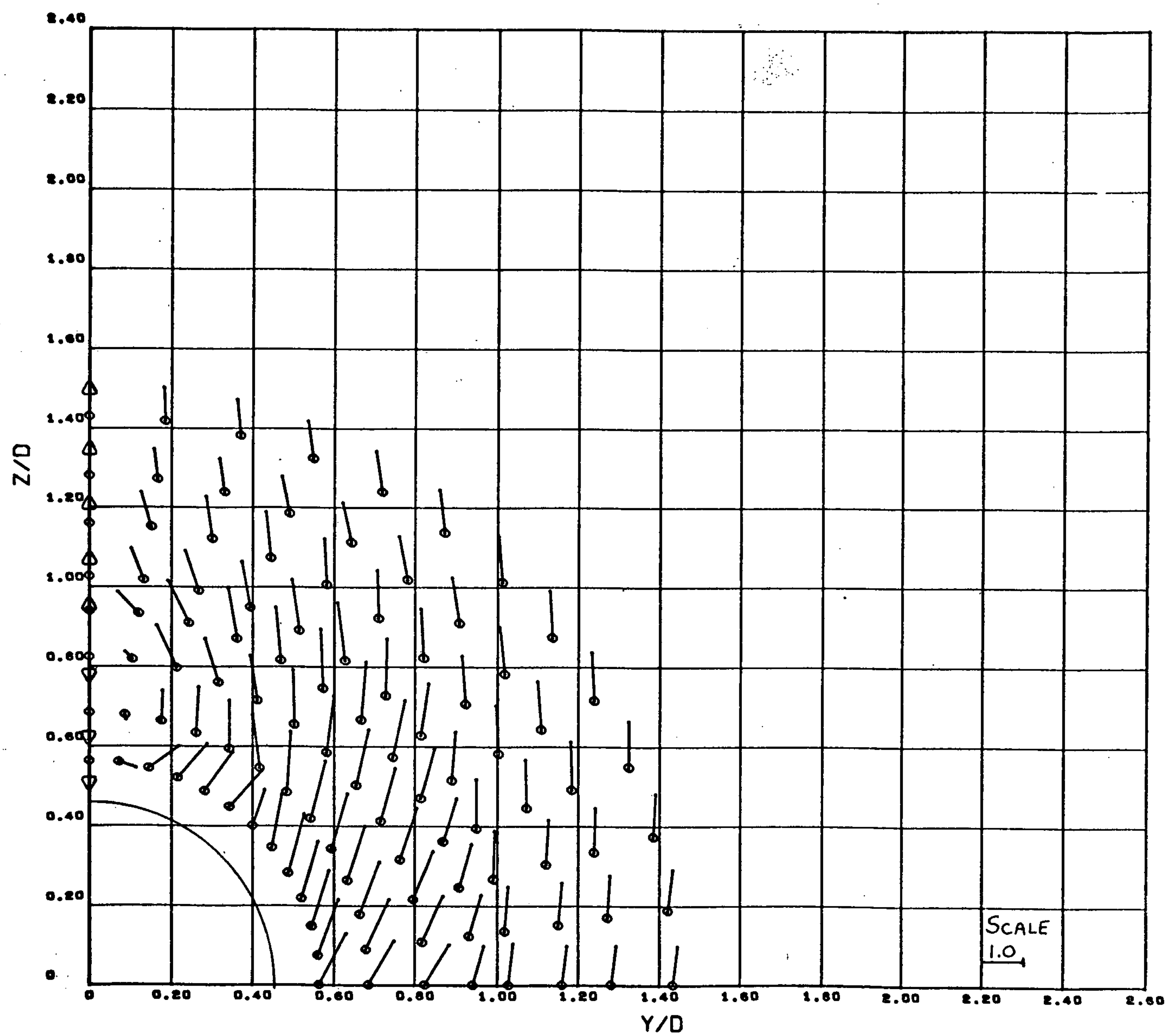

Figure 20d (cont'd) - Local Crossflow Velocity Vectors $\sim \frac{V_c}{V_\infty \sin\alpha}$

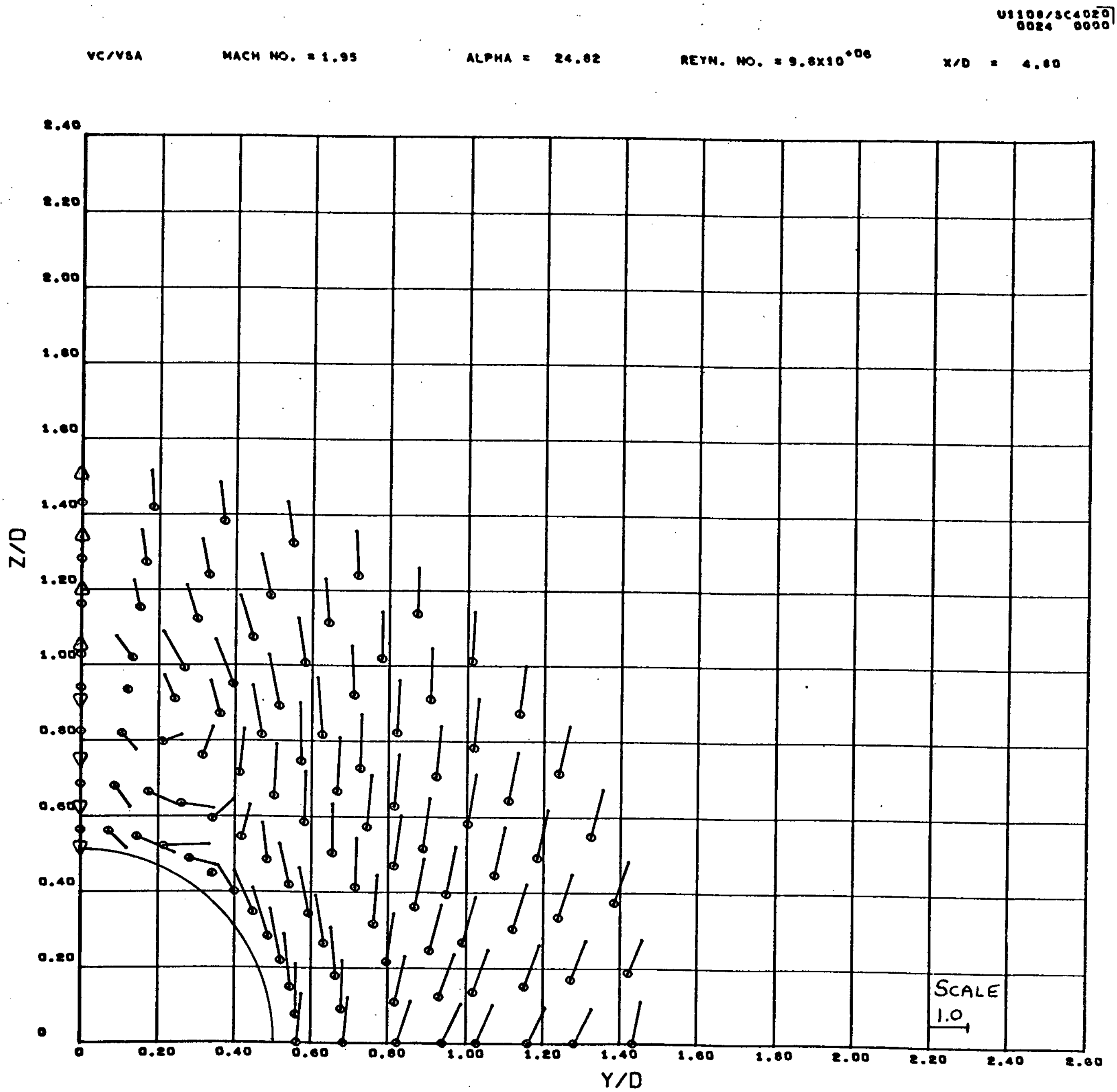

Figure 20d (cont'd) - Local Crossflow Velocity Vectors $\sim \frac{V_c}{V_\infty \sin\alpha}$

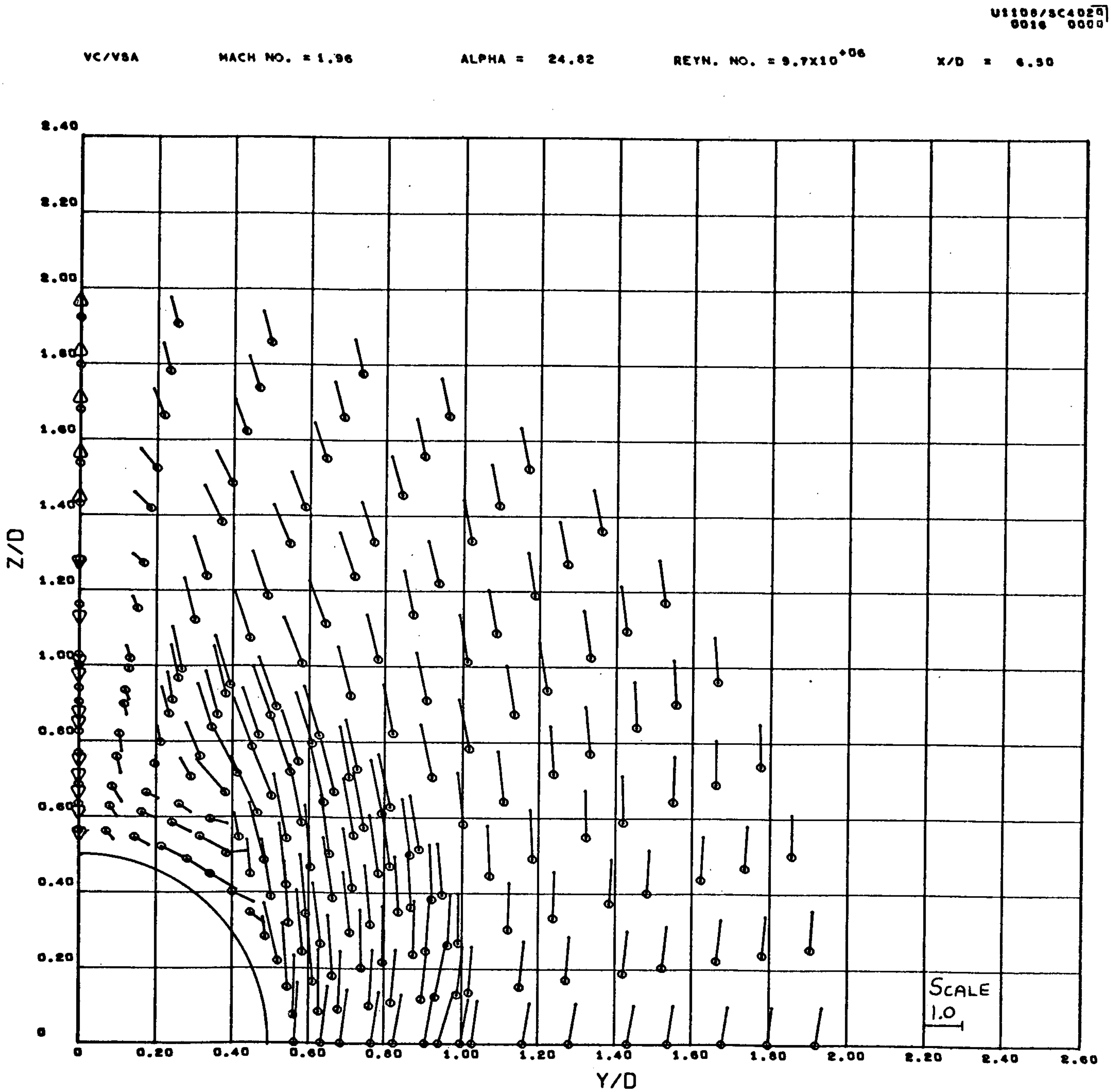

Figure 20d (cont'd) - Local Crossflow Velocity Vectors $\sim \frac{V_c}{V_\infty \sin\alpha}$

C2

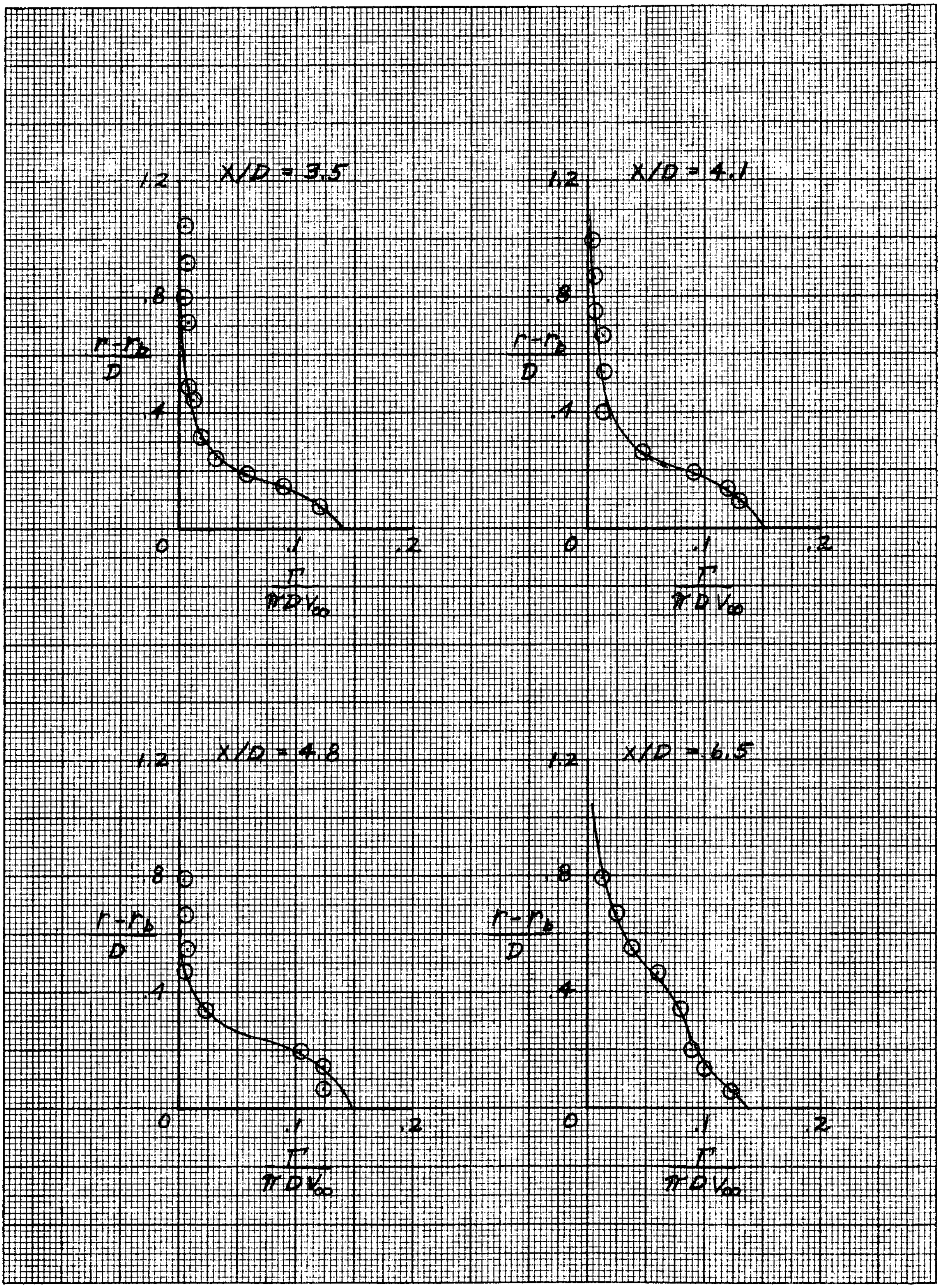

Figure 21 - Total Circulation Strength as a Function of the Inboard Integration Limit $M_\infty = 0.8$, $Re = 4.4X10^6 ft^{-1}$

(a) $\alpha_\infty = 20.1^o$

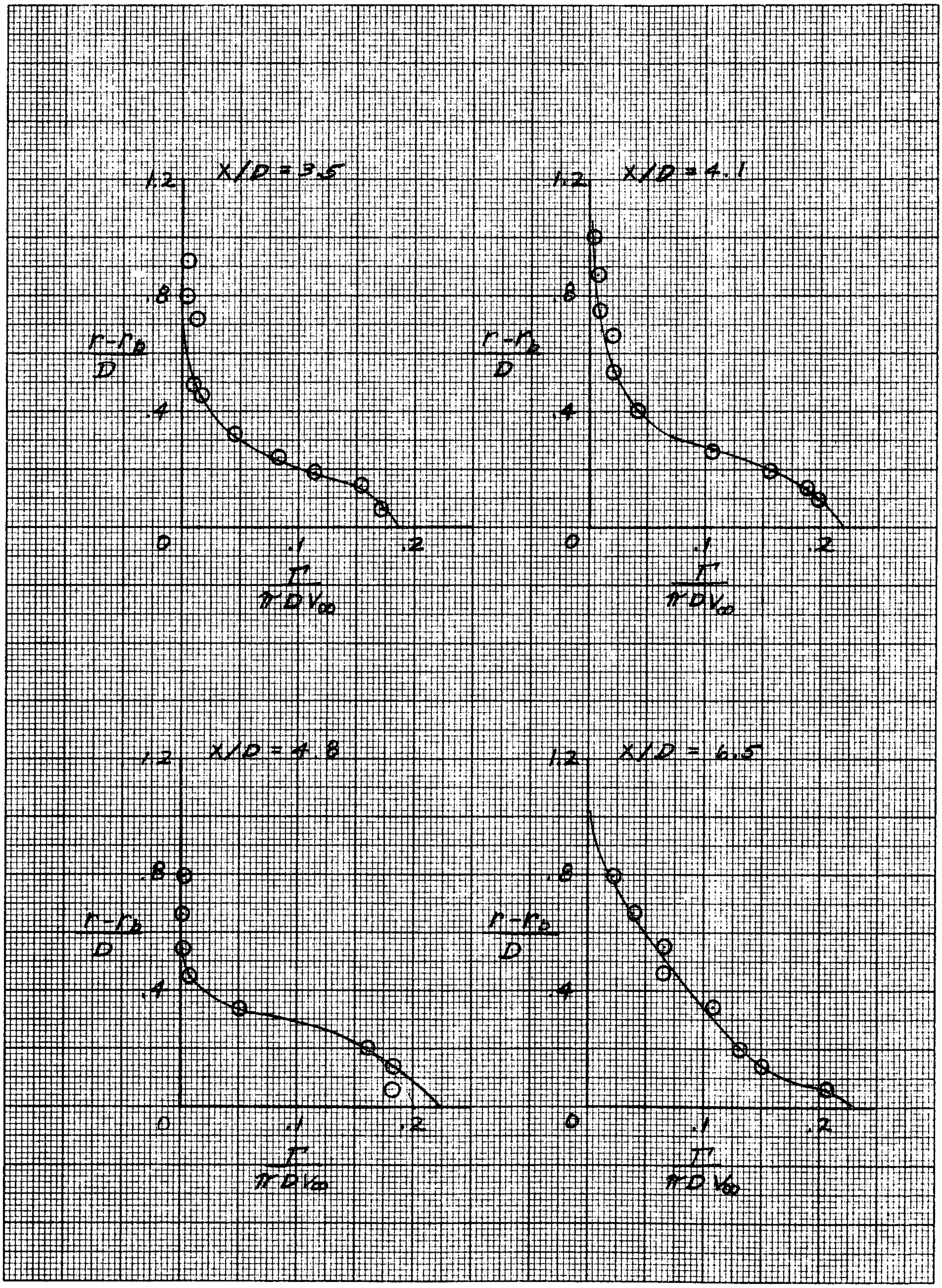

Figure 21 - Total Circulation Strength as a Function of the Inboard Integration Limit, $M_\infty = 0.8$, $R_e = 4.4 \times 10^6 ft^{-1}$
(b) $\alpha_\infty = 24.6^\circ$

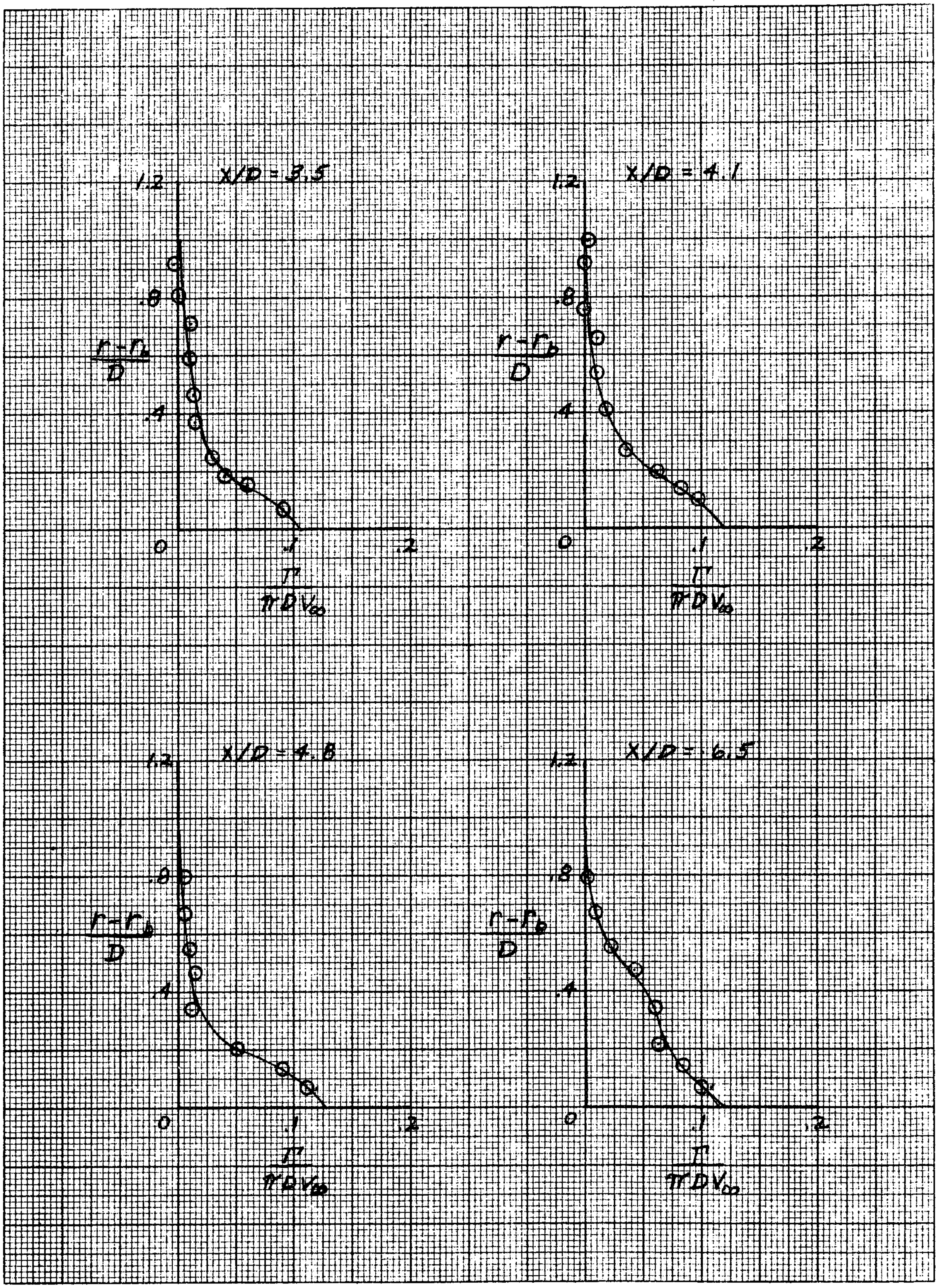

Figure 22 - Total Circulation Strength as a Function of the Inboard Integration Limit, $M_\infty = 0.8$, $Re = 7.9 \times 10^6 ft^{-1}$

(a) $\alpha_\infty = 20.1^\circ$

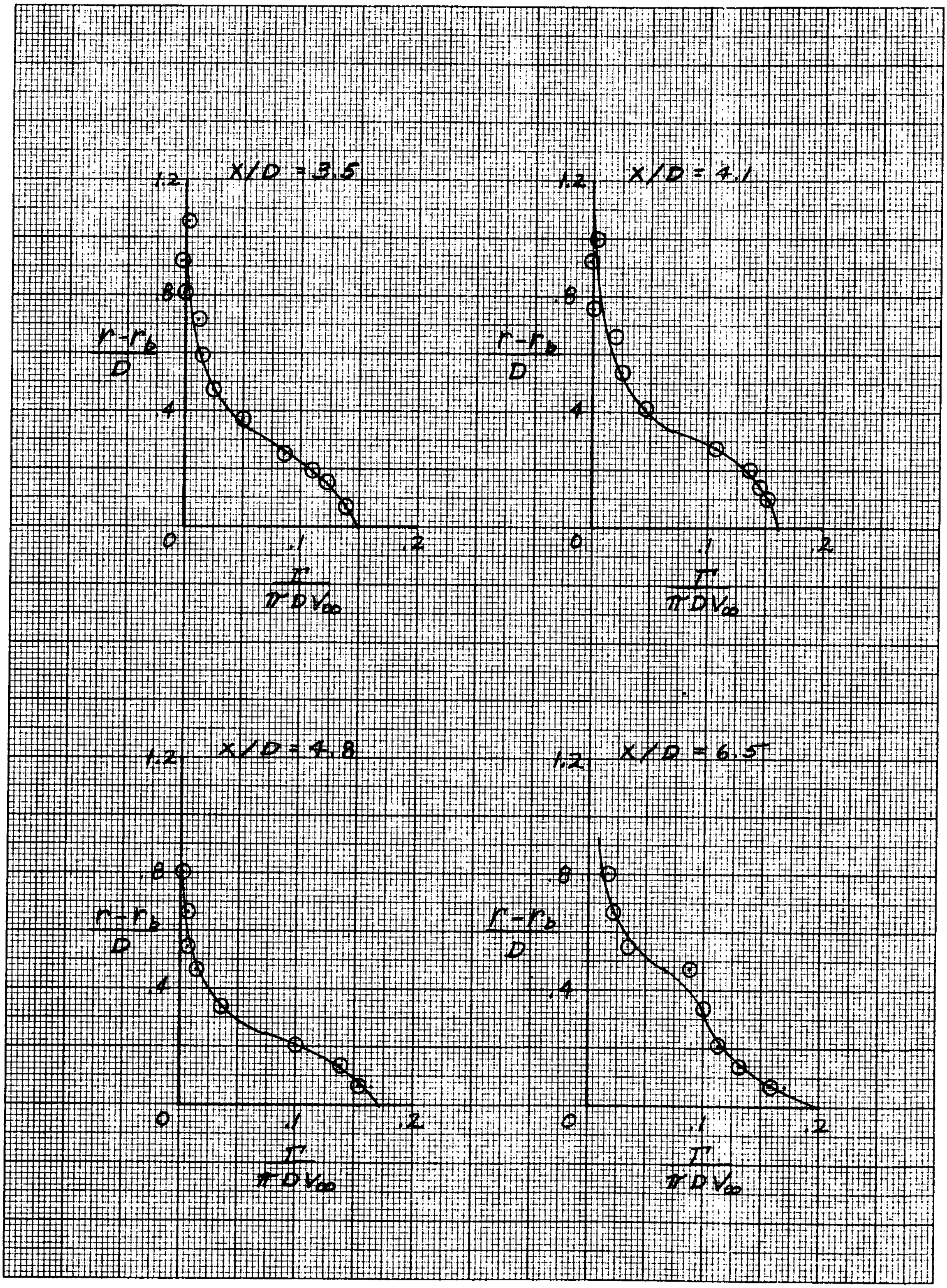

Figure 22 - Total Circulation Strength as a Function of the Inboard Integration Limit, $M_\infty = 0.8$, $R_e = 7.9X10^6 ft^{-1}$
(b) $\alpha_\infty = 24.6^\circ$

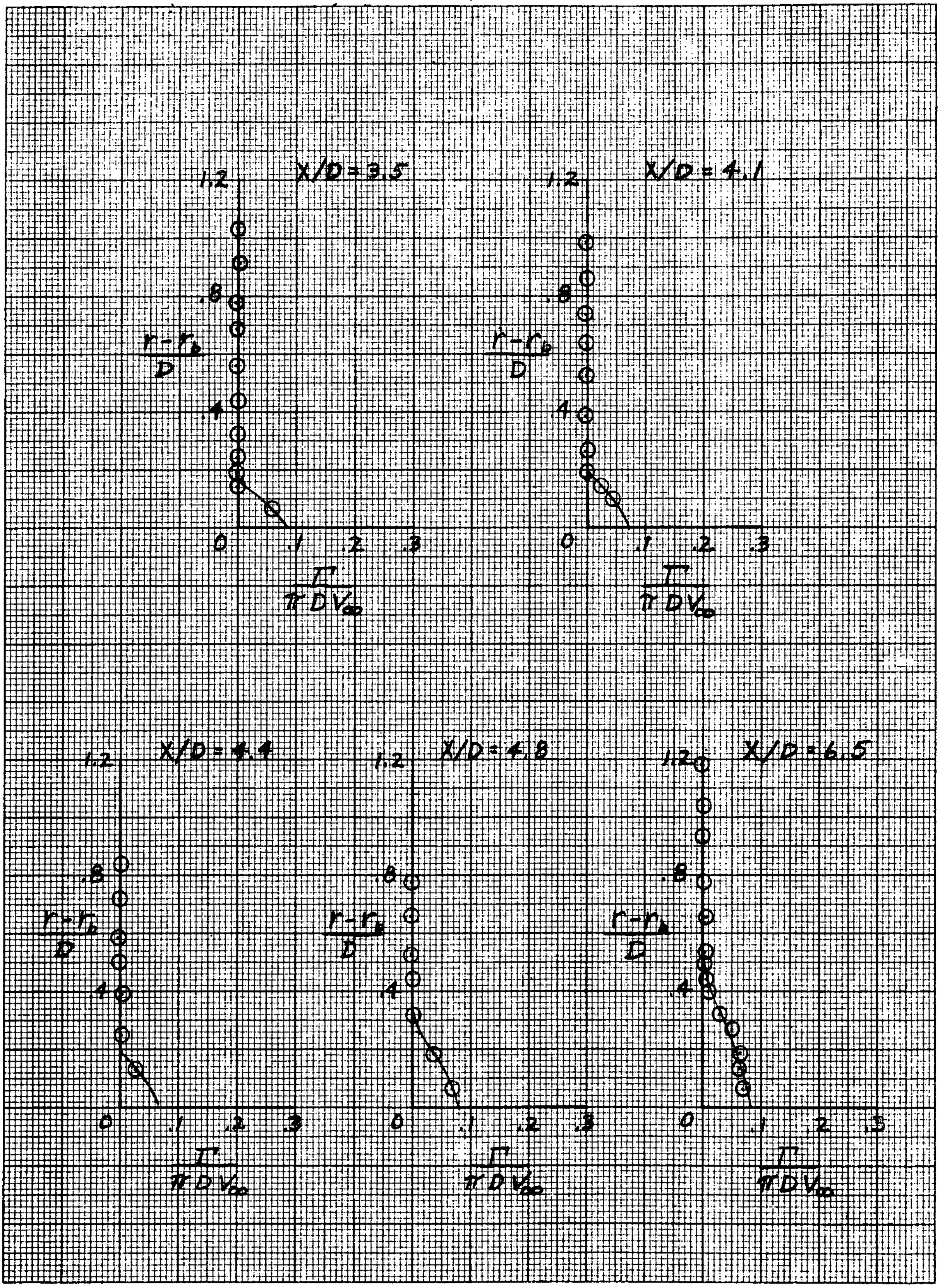

Figure 23 - Total Circulation Strength as a Function of the Inboard Integration Limit, $M_\infty = 1.96$, $R_e = 9.8 \times 10^6 ft^{-1}$

(a) $\alpha_\infty = 14.5^\circ$

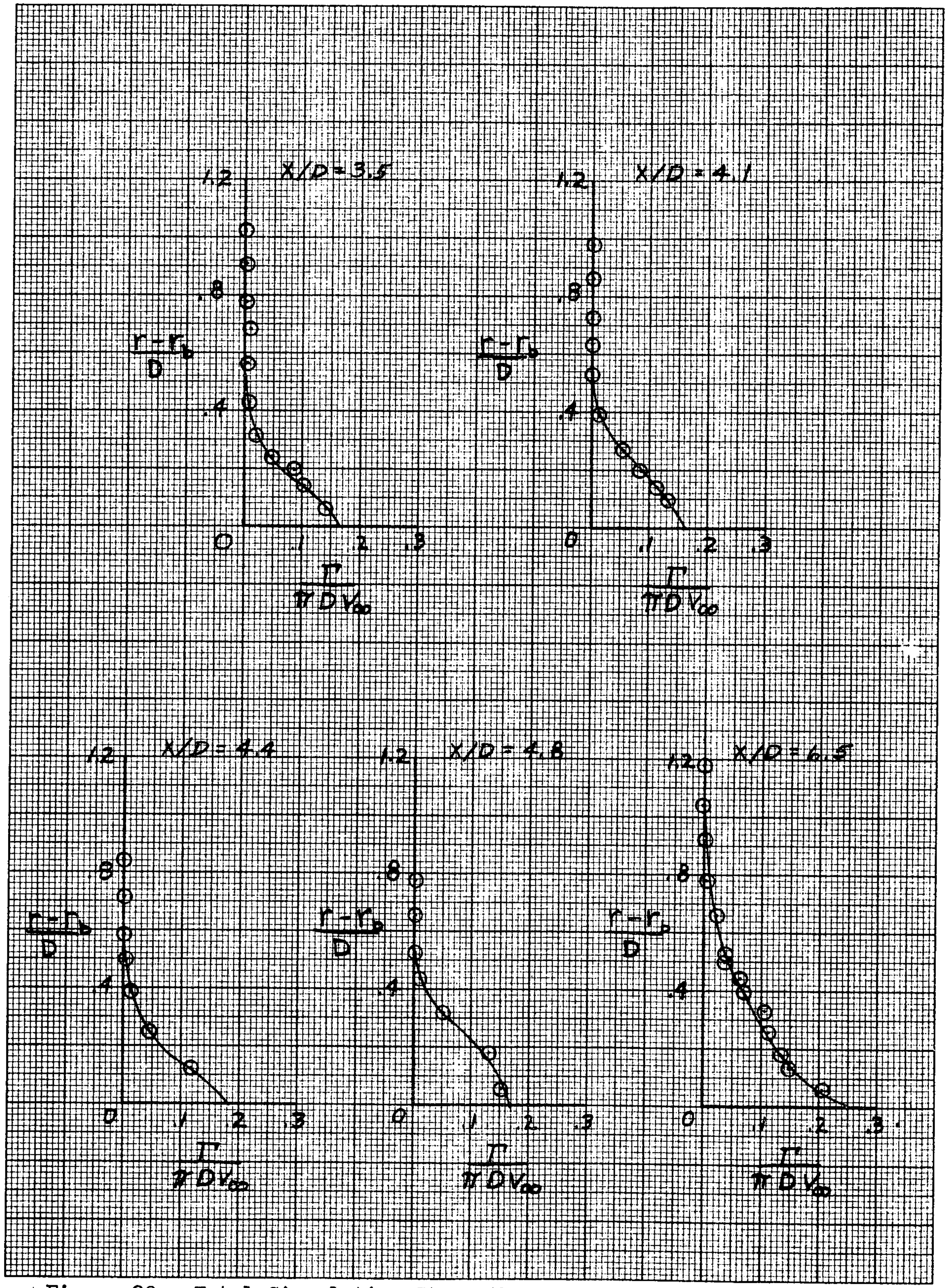

Figure 23 - Total Circulation Strength as a Function of the Inboard Integration Limit, $M_\infty = 1.96$, $R_e = 9.8 \times 10^6 ft^{-1}$

(b) $\alpha_\infty = 20.3^\circ$

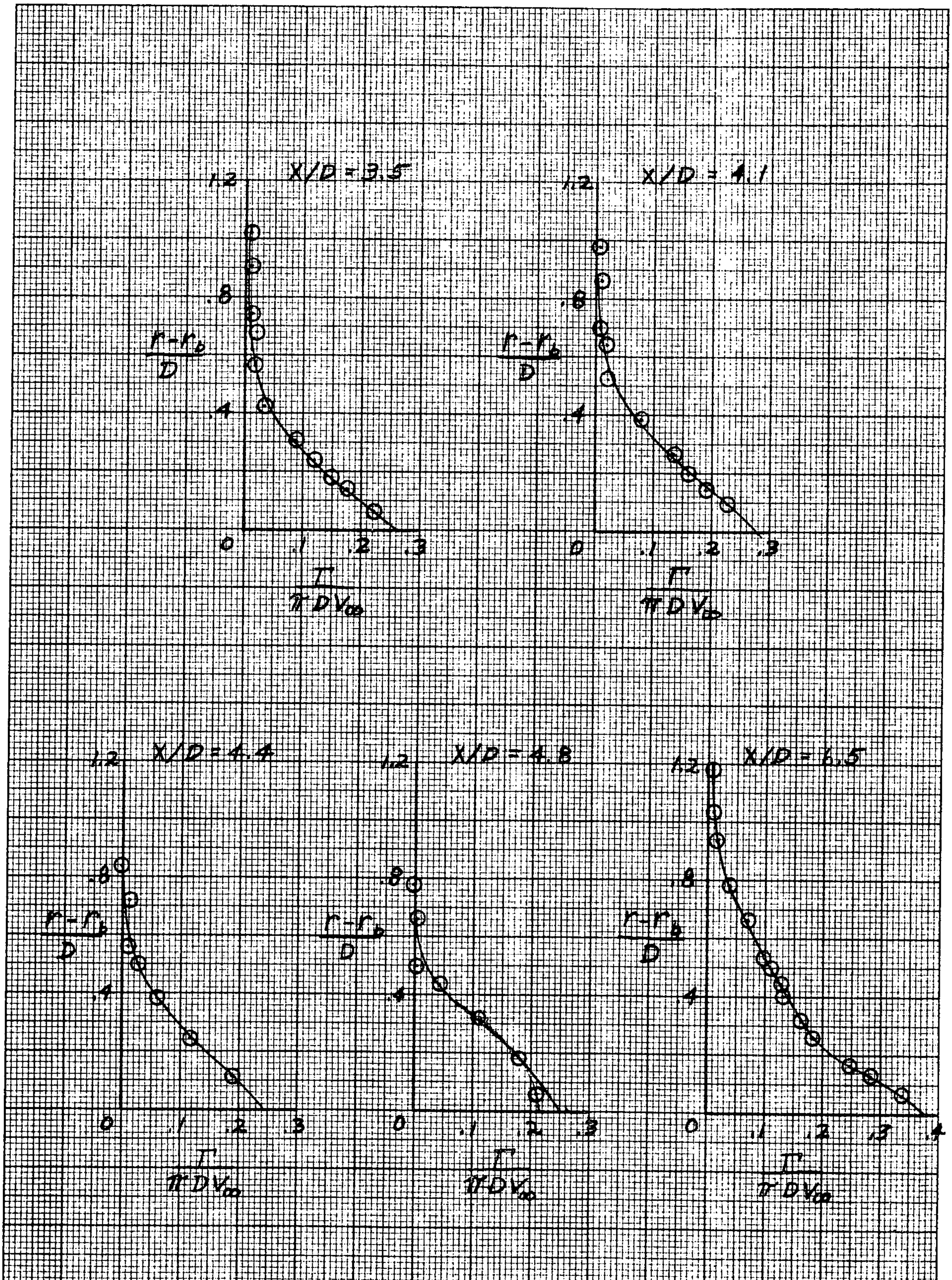

Figure 23 - Total Circulation Strength as a Function of the Inboard Integration Limit, $M_\infty = 1.96$, $R_e = 9.8 \times 10^6 ft^{-1}$

(c) $\alpha_\infty = 24.8^\circ$

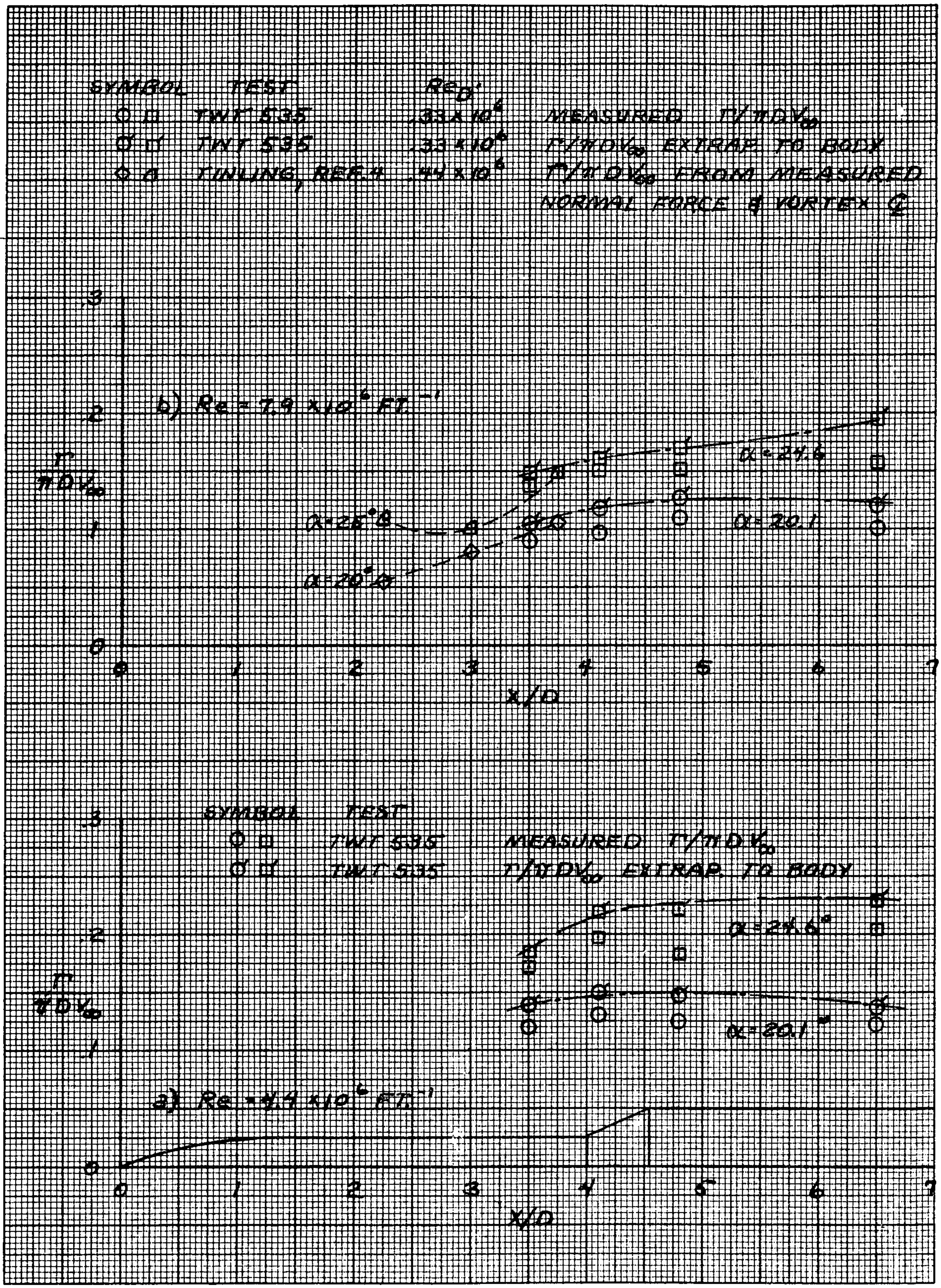

Figure 24. Total Circulation Strength as a Function of Body Station, $M_\infty = 0.8$, $Re = 4.4 \times 10^6 ft^{-1}$ and $7.9 \times 10^6 ft^{-1}$

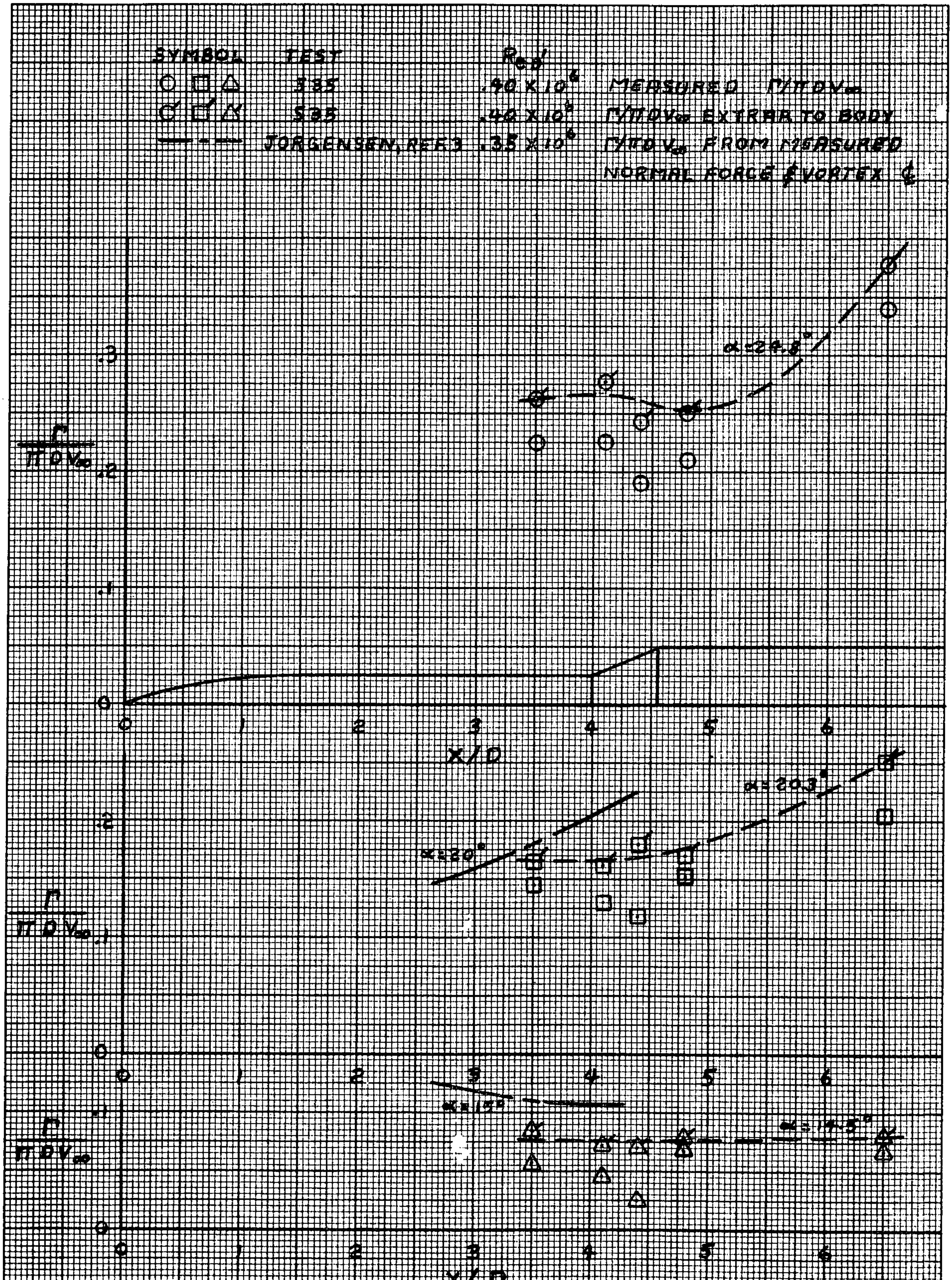

Figure 25. Total Circulation Strength as a Function of Body Station, $M_{\infty} = 1.96$, $RE = 9.8X10^{6}ft^{-1}$

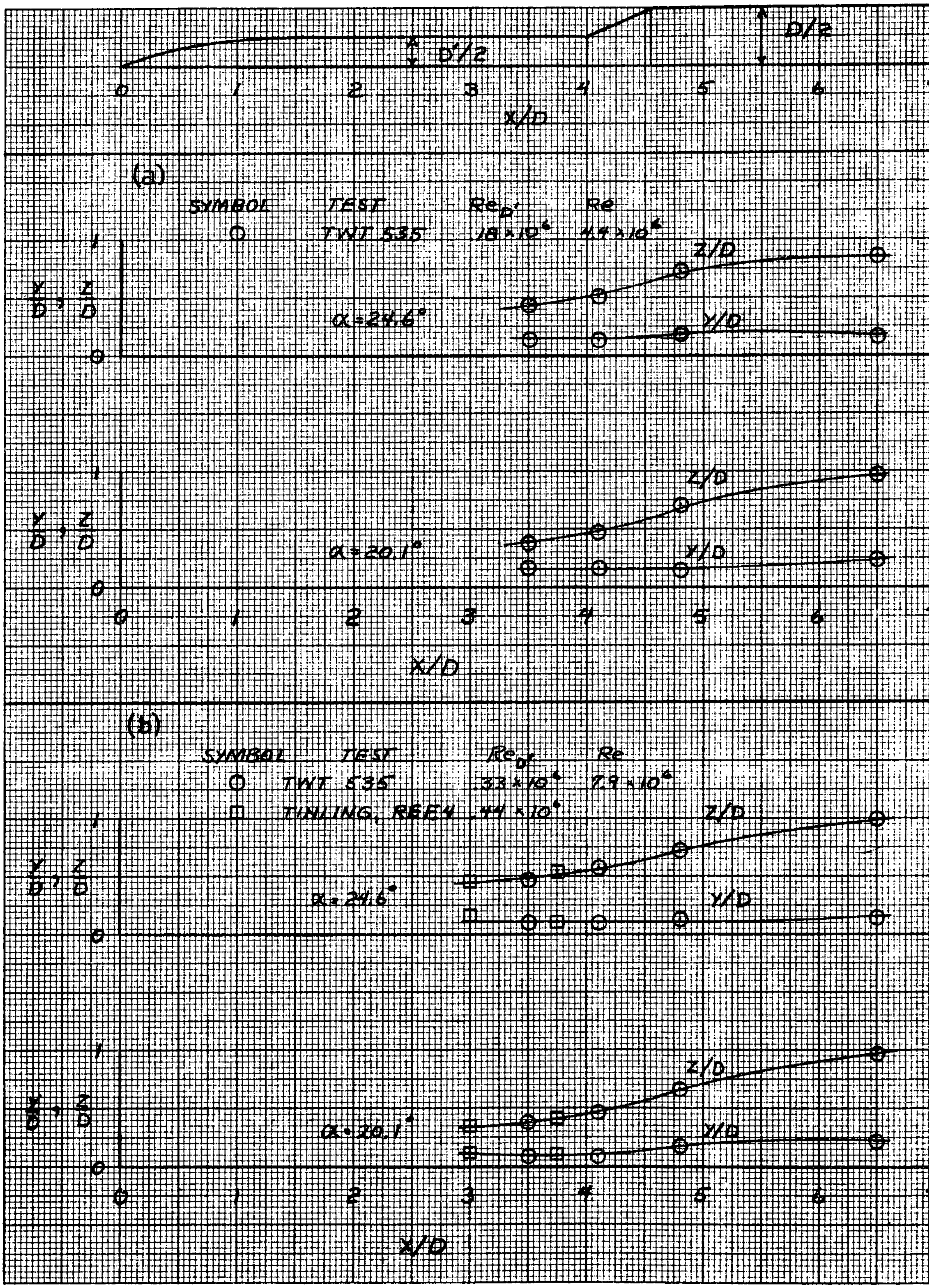

Figure 26. Vortex Center vs Body Station,
$M_\infty = 0.8$; (a) Re = $4.4X10^6$, (b) Re = $7.9X10^6$

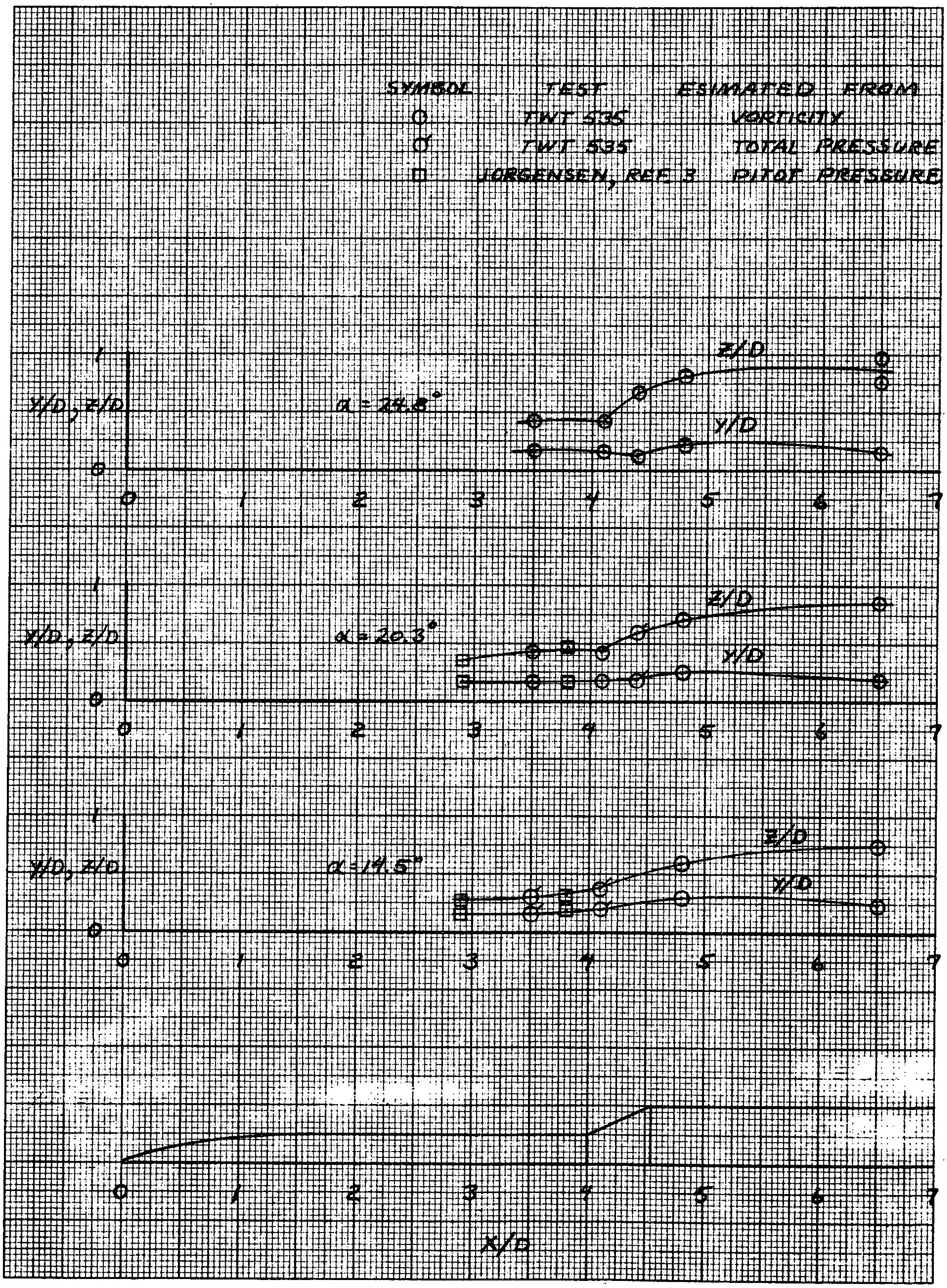

Figure 27 - Vortex Center vs Body Station,
$M_\infty = 1.96$, $R_e = 9.8 \times 10^6$